Processing and properties of bulk and cellular carbon-bonded refractory materials

To the Faculty of Mechanical, Process and Energy Engineering

of the Technischen Universität Bergakademie Freiberg

approved

THESIS

to attain the academic degree of

Doktor-Ingenieur
(Academic degree)

Dr.-Ing.,
(Abbreviation)

submitted

by M. Eng. Bruno Luchini

born on the 09.09.1991 in Sertãozinho (Brazil)

Reviewers:
Prof. Dr.-Ing. habil. Christos G. Aneziris, TU Bergakademie Freiberg
Prof. Dr. Victor C. Pandolfelli, Federal University of São Carlos (Brazil)

Date of the award 18.07.2019

Declaration

I hereby declare that I completed this work without any improper help from a third party and without using any aids other than those cited. All ideas derived directly or indirectly from other sources are identified as such.

I did not seek the help of a professional doctorate-consultant. Only persons identified as having done so received any financial payment from me for any work done for me.

This thesis has not previously been submitted to another examination authority in the same or similar form in Germany or abroad.

Freiberg, 27.02.2019

Acknowledgements

Firstly, I would like to acknowledge Prof. Aneziris for the invitation to conduct my PhD research in Freiberg. Our meetings and discussions were always profitable. Thank you for all the support during those years. I also thank Prof. Pandolfelli for the several Skype meetings and conversations about my research, as well as the constant support from Brazil. I was very lucky with both my advisors.

I want to thank my office mates: Dr.-Ing. Joern Grabenhorst and Dr.-Ing. Jens Fruhstorfer for the countless conversations about refractory materials, and data analysis. Our office was always open for discussing experiments and materials' behavior.

I acknowledge the colleagues from the IKGB for the excellent ambiance and shared breakfast. The colleagues I worked most directly: Dipl.-Ing. Anne Schmidt, Mrs. Kerstin Baldauf, PhD. Ondrej Jankovský, Dr.-Ing. Patrick Gehre, Dipl.-Ing. Ricardo Fricke, Mr. Rico Kaulfürst, Dr.-Ing. Steffen Dudczig, Mr. Uwe Pälchen, thank you!

Thank you M.Sc. Ashish Pokhrel, M.Sc. Andreas Herdering, Dipl.-Ing. Dániel Veres, Dipl.-Ing. Piotr Malczyk, Dr.-Ing. Mahdi Farhani and Dr.-Ing. Tilo Zienert. We shared good stories during lunch time. A special thanks to Mr. Alexander Friedrich for the delicious food and German class.

Special thanks must be addressed to Dr.-Ing. Jana Hubálková. Thank you for the several CT analyses, the proof readings and advises.

I must thank two colleagues that became friends: Dr.-Ing. Enrico Storti and Dipl.-Ing. Tony Wetzig. Thank you both for the always enthusiastic experiments and avid results discussion. We formed a good team!

I thank my family for supporting and encouraging me. My father, mother and brother: *muito obrigado!*

The last, but not least, thank you my lovely Fernanda, for the unconditional support and love.

To find yourself, think for yourself.

Socrates

Contents

List of Symbols and Abbreviations

Symb./Abbrev.	Section	Description	Unit
A_{theor}	3.3.3	Theoretical cross-section area	m^2
α	3.1.4	Thermal expansion coefficient	K^{-1}
$\bar{\alpha}$	3.1.4	Average thermal expansion coefficient	K^{-1}
CCS	3.3.3; 4.2.3; 5	Cold Crushing Strength	$N.m^{-2}$
CS	4.2.3	Compressive strength	$N.m^{-2}$
δ	2.2.2	Strut deflection	m
E	3.1.1	Young's modulus	$N.m^{-2}$
E^*	2.2.2	Young's modulus of the foam	$N.m^{-2}$
E_s	2.2.2	Young's modulus of the material from which the foam is made	$N.m^{-2}$
f	3.1.3	Natural frequency	s^{-1}
F	2.2.2	Generic force	N
G	3.1.4	Shear modulus	$N.m^{-2}$
Γ	3.1.4	Particle's thermally expanded dimension	m
I	2.2.2	Second moment of area	m^4
K	3.1.4	Bulk modulus	$N.m^{-2}$
L	2.2.2	Cell's size	m
	3.1.3	Bar's length	m
	3.1.4	Virtual sample's size	m
	3.3.2; 4.3.1; 4.3.2; 4.3.3	Large samples with 100×100×44 mm^3	-
m_{filter}	3.3.3	Mass of the filter	kg
M_{MOR}	2.2.2	Critical moment	N.m
μ	3.1.4	Mean (temperature variation)	K
	4.2; 4.2.1; 4.2.3	Mean (strut thickness)	m
r	3.1.4	Radius of the finest alumina grain	m
R	3.1.4	Radius of the coarsest alumina grain	m
R''''	2.1.2	Thermal shock parameter	m
R_{st}	2.1.2	Thermal shock parameter	$K.m^{1/2}$

ρ^*	2.2.2; 3.3.3; 3.3.4; 4.3.4	Density of the foam	$kg.m^{-3}$
ρ_s	2.2.2; 3.3.3; 3.3.4; 4.3.4	Density of the material from which the foam is made	$kg.m^{-3}$
σ	3.1.4	Standard deviation (temperature variation)	K
	4.2.1; 4.3.3; 4.3.4	Geometric standard deviation (lognormal distribution)	-
σ^*	2.2.2; 3.3.3; 4.3.1	Foam's crushing strength	$N.m^{-2}$
σ_{MOR}	2.2.2	Modulus of rupture	$N.m^{-2}$
σ_s	3.3.3	Strength of an individual strut	$N.m^{-2}$
t	2.2.2	Strut's thickness	m
T	3.1.3; 3.1.4; 4.1.5	Temperature	K
V_{AF}	4.2.1	Volume after firing	m^3
V_{BF}	4.2.1	Volume before firing	m^3
w	3.1.3	Bar's thickness	m
a	3.1.4	Alumina	-
b	2.2.2	Number of struts	-
CC	3.2.3; 4.2.1	ROI located at the center	-
CF	3.2.2; 3.3.2; 3.3.3; 4.2.2; 4.3.1; 4.3.2; 4.3.3; 4.3.5	Centrifugation	-
CF-T1	3.2.2; 3.2.3; 3.2.3; 3.3; 4.2.1; 4.2.2; 4.2.3; 4.2.4; 5	Centrifugation and single thermal treatment	-
CF-T2	3.2.2; 3.2.3; 4.2.1; 4.2.2; 4.2.3; 4.2.4; 5	Centrifugation and double thermal treatment	-
CRC	1	Collaborative Research Center	-
CT	3; 3.2.3; 3.3; 3.3.3; 3.3.4; 4.2; 4.2.1; 4.2.2; 4.2.3; 4.2.4; 4.3.4; 4.3.5; 5	Computer tomography	-
DFG	1	German Research Foundation	-
FEM	4.3.4	Finite Element Method	-
FR	3.1.4	Fahmy-Ragai	-
ϕ	3.1.3	Correction factor	-
gc	3.1.4	Glassy carbon	-
HS	3.1.4; 4.1.5	Hashin-Shtrikman	-
HT1×	3.1.3; 3.1.3; 4.1.3; 4.1.4	Samples heat treated up to 500 °C, 1 cycle	-

HT2×	3.1.3; 3.1.3; 4.1.3; 4.1.4	Samples heat treated up to 1000 °C, 2 cycles	-
IET	3.1.3; 4.1.1; 4.1.6	Impulse Excitation Technique	-
j	2.2.2	Number of joints	-
JC	3.1.3; 3.1.3; 4.1.1; 4.1.3; 4.1.4	Just cured samples	-
k	3.3.4; 4.3.4; 5	Strut tapering factor	-
l	3.1.4	Lower bound	-
LB	3.2.3; 4.2; 4.2.1	ROI located at Left Bottom	-
LT	3.2.3;4.2; 4.2.1	ROI located at Left Top	-
M	2.2.2	Maxwell's equation	-
PAH	2.3.1; 2.3.2	Polycyclic Aromatic Hydrocarbon	-
PU	3.2.2; 3.2.3; 4.2; 4.2.2; 4.2.4; 5	Polyurethane	-
PVDC	2.3	PolyVinyliDene Chloride	-
RB	3.2.3; 4.2; 4.2.1	ROI located at Right Bottom	-
ROI	3.2.3; 3.3.3; 3.3.4; 4.3.3	Region of interest	-
RS	3.2.2; 3.2.3; 3.3; 3.3.2; 3.3.3; 4.2.1; 4.2.2; 4.2.3; 4.2.4; 4.3.1; 4.3.2; 4.3.3; 4.3.5; 5	Rolling and Spraying	-
RT	3.2.3; 4.2.1	ROI located at Right Top	-
RVE	4.3.4	Representative Volume Element	-
SEM	3.1.3; 4.1.4	Scanning Electron Microscope	-
S	3.3.2; 4.3.1; 4.3.2	Small samples with 50×50×22 mm^3	-
TGA	3.1.3; 4.1.2	Thermogravimetric analysis	-
TEM	2.3	Transmission Electron Microscope	-
u	3.1.4	Upper bound	-
V	3.1.4	Volume fraction	-
WS	3.2.3; 4.2.1	Whole Sample is the ROI	-

1 Introduction

From the beginning of the human species, materials are defining the course of societies' development. Stone and metal ages are just some examples of how important materials are for the evolution of humanity. Mastering materials processing, or even discovering new applications are crucial for companies, research institutions and countries in a globalized market.

The concern about climate change is wide-spread nowadays. A constant search for reducing the impact of human activity on the planet's resources consumption motivates the scientific community and political institutions. In the refractory field this is not different. Investigations about lowering carbon footprint and energy consumption, as well as the use of renewable materials, are gaining significant attention and are modulating this discipline.

According to some researchers, the use of carbon-bonded materials in the steel production should be diminished. A fast research on the *web of science* database with the terms (*Low-Carbon* AND *Refractor**), within the period between 2000 and 2018, resulted in 127 publications (in specialized journals and conference proceedings). After carefully analyzing all the publications, 74 works remained related to refractories containing Carbon. The higher number of publications and consequent interest of the academy and research community became evident in the last 5 years. Dividing the works by their publication date, 46 researches were published between 2014 and 2018. This number was 15 and 9 for the periods of 2009–2013 and 2004–2008, respectively. For comparison, only 4 papers were published on this topic between 2000 and 2003.

The vision of stopping using carbon in refractories is, at least, too simplistic. It nullifies the evolution of this material's comprehension and limits the development of innovation. The first use of carbon in refractories dates back to the 1860's (use of ground coke and tar in carbon blacks and pastes for iron and ferroalloy furnaces in Europe). Since then this material has been studied and modified, to address harsher and harsher requirements.

It is clear that lowering the carbon footprint in the steel production should be a general concern. However, carbon could also be part of the solution. One can not negate the unique thermo-mechanical properties of graphite, nor the excellent thermal-shock resistance of carbonaceous binders, or even the new possibilities of not yet fully characterized carbon nanotubes, graphene and graphene-oxide, for instance.

In a more holistic thinking, one should take into account the whole chain of refractories production and their role as raw material impact on the production chain. For example, it is known that carbon-bonded alumina foam filters are the state-of-the-art material for steel melt filtration. This crucial step in the steel production reduces the amount of non-metallic inclusions in the finished steel, playing a major role in safety by increasing the fatigue life of parts and reducing the tool wear during machining. Therefore, higher-quality metal is produced.

Focusing just on fatigue life, if a metal with higher fatigue life is chosen, lighter components can be made, compared to a non-filtered metal for a fixed life time criterion. Supposing that this metal would be used for an automobile or airplane structural component, then lower fuel

consumption and a consequent lower CO_2 emission would be achieved.

This is just one example of how complex it is to address materials selection in such interconnected environment, where decisions should envisage multiple areas. In situations like this, computer-assisted analyses gain importance.

The virtualization of the real world is already a reality for the materials science domain. Several studies are being carried out concerning the numerical modelling of the thermo-mechanical behavior of materials (mainly after the 1970's). On the one hand, having a numerical model allows the researchers to analyze the materials in distinct scenarios, saving time and physical resources. On the other hand, the models must be well-calibrated with real experiments, otherwise the results are pointless and will distort the material characterization.

In this manuscript, distinct problems concerning carbon-bonded materials processing and characterization were analyzed, from bulk to cellular samples. The main motivation was to address central topics that would enhance the comprehension of the material's behavior, as well as trigger targeted improvements. Some of the topics this thesis covers are:

- Non-linear Young's modulus behavior of carbon-bonded alumina at high temperatures;
- Influence of the processing route on the cold crushing strength of carbon-bonded alumina foam filters;
- Geometric characterization of ceramic foam filters as a tool to understand processing parameters;
- Use of advanced techniques such as computer tomography and finite element modelling to correlate processing parameters and mechanical behavior.

In most of the analyses, non-standard computational strategies were adopted. In those cases, algorithms were written to facilitate the evaluations, or even enable it in the first place. All the algorithms' concepts are described in this thesis and their codes are available in the Appendices.

The current work was carried out within the framework of the Collaborative Research Center 920 (CRC 920) "Multifunctional filters for metal melt filtration - a contribution to zero defect materials" at the Technische Universität Bergakademie Freiberg funded by the German Research Foundation (DFG).

2 Theoretical Background

As explained in the Introduction, this manuscript treats both: carbon-bonded **bulk** and carbon-bonded **cellular** materials. Therefore, in order to facilitate the reader's comprehension of the distinct subjects, some topics were selected and are further detailed in the following subsections.

Firstly, some of the state-of-the-art carbon-bonded bulk materials are analyzed, namely: carbon-bonded alumina and carbon-bonded magnesia. Afterwards a literature research on carbon-bonded cellular materials is presented, including the basic mechanics of cellular materials. Finally, the most common carbon sources for refractory applications are reviewed and typical impacts of the carbon source on the refractories' thermo-mechanical properties are discussed. This last part is considerably important, since modern refractories should be analyzed as complex composites. Therefore, the behavior of each individual raw material must be well understood in order to design and analyze the final product.

The theoretical background is not limited to the present section. The section "Materials and Methods" includes three sub-sections named "Motivation" where topics directly related to the experiments conducted are also reviewed.

2.1 Carbon-bonded bulk materials: state of the art

Roungos correlated the addition of carbon in functional refractories to a significant decline in the refractory consumption by the steel industry in the last decades [1]. The author commented that carbon-bonded refractories were crucial for the success of continuous casting technologies. Nowadays, 92 % of the world's crude steel is produced by continuous casting [2].

In general, carbon-bonded bulk refractories are used in harsher condition zones, where thermal shock, erosion and corrosion resistances are crucial. For instance, carbon-bonded alumina can be found in ladle shrouds, monoblock stoppers (Fig. 2.1a) and submerged entry nozzles [1, 3, 4], while carbon-bonded magnesia bricks (Fig. 2.1b) are mostly used in the ladle lining – like in the slag, baths and impact zones [1,5,6], converters and electric arch furnace [7].

Resende *et al.* [5] analyzed refractories prepared by the combination of alumina, magnesia, silica and graphite bonded by a carbonic resin. Several experiments were carried out, with focus on the corrosion resistance against basic slags. The authors concluded that the recipe with the highest graphite content was the less corroded one. Those samples also presented the highest refractoriness under load.

2.1.1 Alumina-Carbon

Stein and Aneziris [10] listed some important requirements which carbon-bonded alumina components should fulfill in steel-making applications: for instance, high corrosion and erosion

(a) (b)

Figure 2.1: (a) Tundish monoblock stopper; (b) MgO-C refractory bricks. Extracted from [8] and [9], respectively.

resistance, low wettability against steel and slag melts, high thermal shock performance and high mechanical strength at elevated temperatures.

The thermal shock performance is an essential property for functional components like submerged entry nozzles, since those elements must withstand severe thermal variations in the tundish system. Normally, the Al_2O_3-C functional components are preheated from room temperature up to 1100 °C and, afterwards, must resist the contact with molten metal at 1550 °C [11–13].

Mertke and Aneziris [14] investigated the influence of nanoparticles dispersion and functional metallic additions on the thermal shock resistance of Al_2O_3-C refractories. The authors reported an increase of the thermal shock resistance for samples containing nanoparticles and metallic Si. SiC whiskers were found in the microstructure, explaining the better thermo-mechanical performance.

Other studies explored the addition of alumina sheets and carbon nanotubes in Al_2O_3-C refractories. It was demonstrated that the mechanical and thermo-mechanical properties were improved due to the formation of an Al_2CON phase [3].

Recently, Zhang and Zhu [15] developed an *in situ* catalyzed-growth technique to form large quantities of oxide nanofibers and carbon nanotubes in carbon-bonded refractories. The technique is based on the reaction of fine oxides and carbides precursors with a transition metal catalyst (e.g. Co or Ni). Because of the intrinsic features of the so-called nanofibers, excellent thermal stability and mechanical strength were reported, increasing the erosion/abrasion resistance of the refractory.

Conventionaly, bulk parts made of carbon-bonded alumina are shaped using pressing techniques (uniaxial and hidrostatic). Jahn *et al.* [16] investigated the manufacture of carbon-bonded alumina tiles using pressure slip casting. The results were promising, and the final parts showed material properties close to the state-of-the-art carbon-bonded alumina used in

the steel industry.

2.1.2 Magnesia-Carbon

In the modern steelmaking industry, the use of basic slags is widespread. They present a higher capacity of removing phosphorous and sulfur contaminants from the steel than the acidic ones [17]. Therefore, dolomite and MgO refractories achieved a great importance, the first one being the most used in the beginning of the 20^{th} century, thanks to its lower price and higher availability. However, with the harsher conditions of advanced steel making processes, MgO is preferred, because of its high refractoriness and thermal conductivity, consequently better thermal-shock performance [17].

MgO presents a high thermal expansion coefficient, which impairs its thermal shock resistance. Therefore, the combination of MgO with graphite is really advantageous. As it will be explained (see Section 2.3.4), due to its lamellar structure and anisotropy, graphite is used to tune the thermal expansion coefficient of refractories [18, 19].

MgO-C refractory linings are well known as high-duty refractory products because of their outstanding mechanical, thermal, and chemical properties for applications in converters, electric furnaces, and steel treatment ladles [20].

In general, the residual carbon content of MgO-C refractories lays between 5 and 30 wt. %. The carbon will be responsible for a lower Young's modulus and strength, due to a poor carbon-oxide bonding [21]. On the other hand, the work of fracture is increased, boosting the refractory toughness [22].

Rodrigues and Pandolfelli [22] analyzed the R-curve behavior of MgO-C bricks with two distinct residual carbon content (8 and 13 wt. %). They showed that, despite reducing the modulus of rupture and Young's modulus at room temperature, the higher residual carbon substantially increased the fracture energy and $R^{''''}$ and R_{st} thermal shock parameters. This was mainly motivated by crack bridging and effective lower thermal expansion coefficient.

Leite *et al.* [23] suggested that, in order to obtain a composition of the MgO-C system with high refractoriness and corrosion resistance, large MgO crystals, low impurity level, high CaO/SiO_2 ratio and low amount of B_2O_3 are desired.

2.2 Carbon-bonded cellular materials: state of the art

Cellular materials combine the properties of a solid material with a cellular morphology in order to obtain a structure with high property to weight ratio [24]. By properties one could list: stiffness, strength, thermal conductivity and diffusivity, etc. [25]. Cellular ceramics have become increasingly popular in the last 30 years, mainly thanks to their applications as filters, catalyst carriers, membranes and scaffolds for cell growth [25, 26].

2.2.1 Applications

Carbon-bonded cellular materials gained significant attention in the last decade, mainly motivated by clean steel technologies [27–35]. Carbon from different sources (natural graphite, carbon black, resin and pitch) is usually combined with stable oxides (MgO, Al_2O_3), forming a highly functional refractory.

Emmel and Aneziris [36, 37] conducted important studies of carbon-bonded alumina foam filters, produced by the replica technique, applied in the steel melt filtration. Based on their formulation, several studies [29, 33, 35, 38–40] helped increasing the knowledge around this complex composite.

Slurry replica technique [41] is by far the most industrialized processing method for ceramic filter production. Its huge development is due to the increasing metal quality from which the casting industry is demanded. Millions of pieces are used every year to filter different kinds of metal alloys prior and during their casting [42].

Despite the well-established benefits of metal melt filtration, this technique is rarely applied in the continuous casting of steel. The main reason is related to excessive clogging of the filters, which is in conflict with the continuous tundish operation. Recently, Wetzig and Aneziris [28,29] proposed the concept of exchangeable ceramic filters for tundish applications as a response to this problem. Promising results were attained in industrial trials [29], making this new procedure a possible route to combine the excellent filtration efficiency of ceramic foam filters with the continuous casting requirements.

As those filters are used directly in the tundish system [29], their geometries are relatively complex (see Fig. 2.2). The first trials used cylindrical filters with 200 mm diameter and 200 mm height. Filters with such large dimensions are challenging to manufacture and require several analyses to attest their integrity. Otherwise, they may not withstand the harsh conditions faced during the tundish operation [28]. The up-scaling of the filters' geometry is a non-trivial task and is an important topic of the Collaborative Research Center 920 framework.

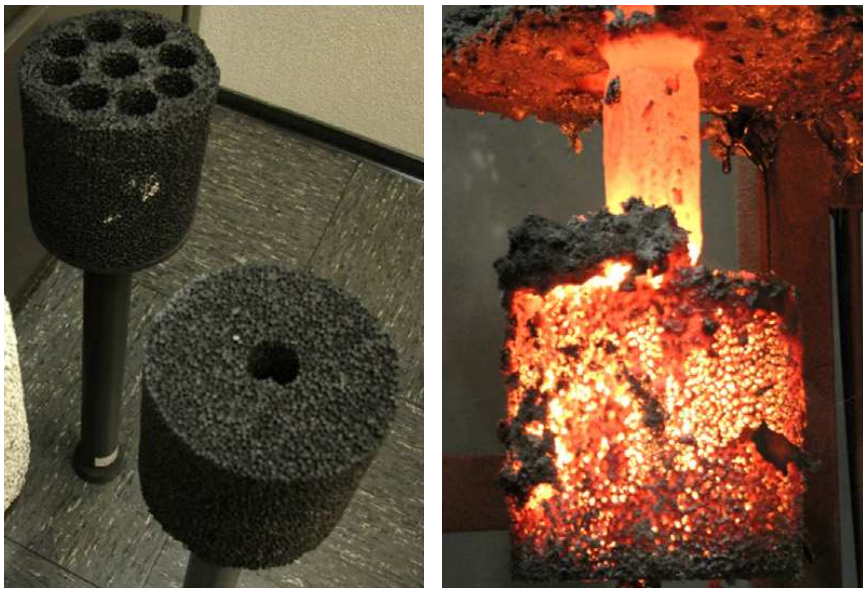

(a) (b)

Figure 2.2: (a) Carbon-bonded alumina filters before industrial test; (b) Carbon-bonded alumina filter after industrial test. Extracted from [29].

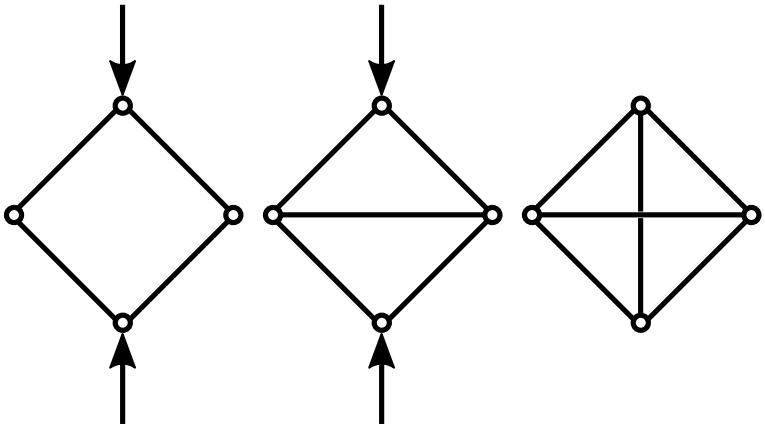

Figure 2.3: (a) Bending-dominated structure; (b) Stretch-dominated structure; (c) Over-constrained (self-stressed) structure. Extracted from [25].

2.2.2 Cellular Mechanics

Ashby [25] highlighted the three main factors determinant to the cellular material properties, that are: (i) the properties of the solid material of which the foam is made; (ii) the topology (connectivity) of the cell edges; and (iii) the relative density, ρ^*/ρ_s, of the foam, where ρ^* is the density of the foam and ρ_s the one of the solid of which the foam is made.

One important concept of cellular geometries was developed based on Maxwell's study about the equilibrium and stiffness of frames [43]. Maxwell's equations are very important for structural design and were used by Gibson and Ashby [26] to differentiate stretch-dominated and bending-dominated foam geometries.

Assuming a frame with b struts connected by j friction-less joints, like those in Fig. 2.3, equation 2.1 (for bidimensional frames) assesses if the structure is statically and kinematically determinate, i.e. if it is rigid and will not fold up when loaded.

$$M = b - 2 \cdot j + 3 \tag{2.1}$$

In three dimensions, the equivalent equation is:

$$M = b - 3 \cdot j + 6 \tag{2.2}$$

If $M < 0$ (Fig. 2.3a), the structure is considered a *mechanism* and presents one or more degrees of freedom of movement. If the joints are not pinned like in Fig. 2.3, but locked, like in ceramic foam filters, the struts **bend** when the structure is loaded. Therefore, foam geometries presenting $M < 0$ are considered **bending-dominated** structures.

On the other hand, if $M = 0$ (Fig. 2.3b), the frame is not a *mechanism* any longer. Therefore, if the structure is loaded, the struts will carry tension or compression, and the foam becomes a **stretch-dominated** structure.

Figure 2.3c represents an over-constrained (self-stressed) structure ($M > 0$). If the vertical strut is shortened, it pulls the other struts into compression, that is balanced by the tension

on the shortened strut. The struts can be stressed even though the structure carries no external loads. $M > 0$ foams are also considered **stretch-dominated** structures. Maxwell's equations give insights to design cellular materials, and indicate the reason why most of the foam geometries are *bending-dominated* [25] (Fig. 2.4).

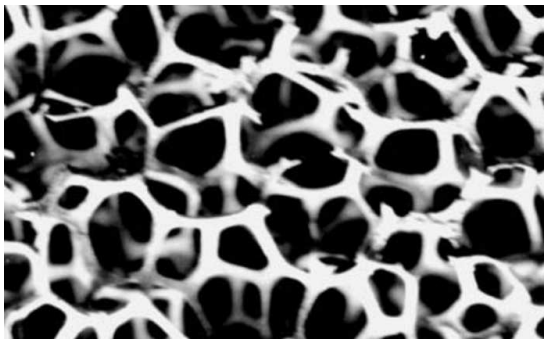

Figure 2.4: A typical cellular ceramic structure. Extracted from [44].

Based on an ideal unit cell with $M < 0$ (Fig. 2.5a), Gibson and Ashby [26] derived some important equations correlating the foam's relative density with its elastic modulus and mechanical strength. From Fig. 2.5a (with $t \ll L$), one can verify that:

$$\frac{\rho^*}{\rho_s} \propto \left(\frac{t}{L}\right)^2 \tag{2.3}$$

where L is the cell size and t is the strut's thickness.

Assuming a foam subjected to a remote compressive stress σ exerting a force $F \propto \sigma \cdot L^2$ on the cell edges, the struts would bend (Fig. 2.5b). Considering the bend deflection as δ, a strut with a length L, loaded at its mid-point by a force F would deflect:

$$\delta \propto \frac{FL^3}{E_s I} \tag{2.4}$$

where E_s is the elastic modulus of the strut's material and I is the second moment of area of the strut ($I = t^4/12$ for a square cross-section, $t \times t$).

The compressive strain suffered by the whole cell is then $\varepsilon \propto 2\delta/L$. Combining the results, the relative elastic modulus ($E^* = \sigma/\varepsilon$), for a bending-dominated behavior, can be expressed as:

$$\frac{E^*}{E_s} \propto \left(\frac{\rho^*}{\rho_s}\right)^2 \tag{2.5}$$

A similar approach was used to calculate the collapse load* of a brittle structure, typical for ceramics (Fig. 2.5c). A critical moment, M_{MOR}, before the strut's failure can be expressed as:

$$M_{MOR} = \frac{\sigma_{MOR} \cdot t^3}{4} \tag{2.6}$$

*The collapse criterion was based on full section plastic deformation criterion of ductile material beams.

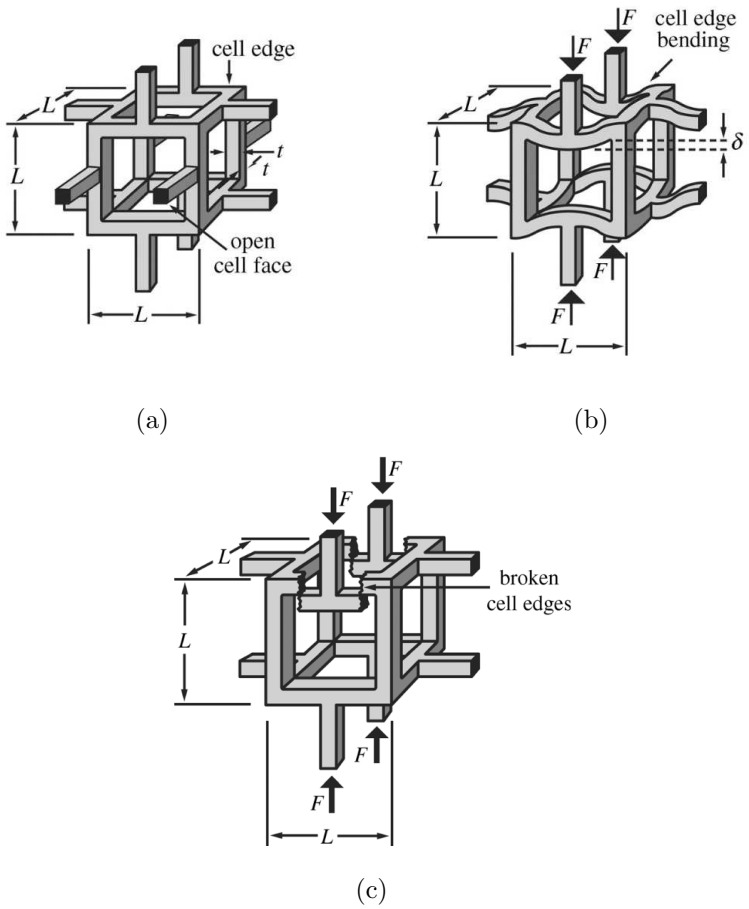

Figure 2.5: (a) An idealized cell of an open-cell foam. (b) Bent struts of a unit cell. (c) Brittle foam collapse. Extracted from [25].

where σ_{MOR} is the modulus of rupture of the strut's material. The M_{MOR} is related to the remote stress by $M_{MOR} \propto F \cdot L \propto \sigma \cdot L^3$. Re-assembling the equation gives:

$$\frac{\sigma^*}{\sigma_{MOR}} \propto \left(\frac{\rho^*}{\rho_s}\right)^{3/2} \tag{2.7}$$

where σ^* is the foams' crushing strength.

Similar equations were calculated for stretch-dominated, Fig. 2.6, geometries [25]:

$$\frac{E^*}{E_s} \propto \left(\frac{\rho^*}{\rho_s}\right) \tag{2.8}$$

$$\frac{\sigma^*}{\sigma_{MOR}} \propto \left(\frac{\rho^*}{\rho_s}\right) \tag{2.9}$$

Figures 2.7a and 2.7b, respectively, summarize the relative modulus of elasticity and crushing strength of typical cellular materials as function of their relative densities. The influence of

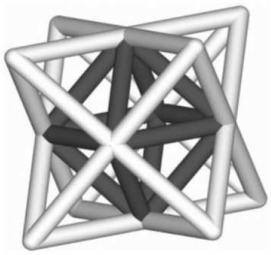

Figure 2.6: Unit cell of a stretch-dominated structure. Extracted from [25].

the cell connectivity is obvious (see ideal stretch- and bending-dominated behaviors). One can also notice that typical foams show mechanical behavior closer to that of bending-dominated structures.

It must be highlighted that the Equations developed by Gibson and Ashby [26] are simplified guidelines for the design and characterization of cellular materials, since several simplifying assumptions were made. For instance, the assumption of an ideal cell geometry with fixed cross-section dimensions (Fig. 2.5a). It is well-known that ceramic foam filters produced by the replica technique [41], generally present hollow and tapered struts [34, 36].

Two of the first authors who dealt with the effect of the strut morphology on the failure surface of cellular materials were Kim and Al-Hassani [45]. Based on the experimental work from Triantafillou [46], the authors investigated the influence of the strut tapering on the plastic yield surface of foams. They concluded that plastic collapse due to bending moment is the dominant failure mode for most metal foams subjected to multiaxial load (as predicted by Gibson and Ashby's model [26]). However, for highly tapered struts, normal modes in the struts parallel to the load direction become significantly important, contributing to the failure criteria envelope. Therefore, the shape of the plastic yield surface was found to depend not only on the relative density, but also on the strut morphology.

With the advance of computational materials simulation, several authors analyzed the mechanical behavior of cellular materials subjected to distinct loads. Some based their geometries on simplified structures, like Kelvin (Tetrakaidecahedron) cells [47–51], others generated models with more realistic geometries [42, 52–54]. In both cases, the possibility of several analyses enriched the cellular materials field, and a deeper comprehension of the mechanical behavior of open-cell foams has been achieved.

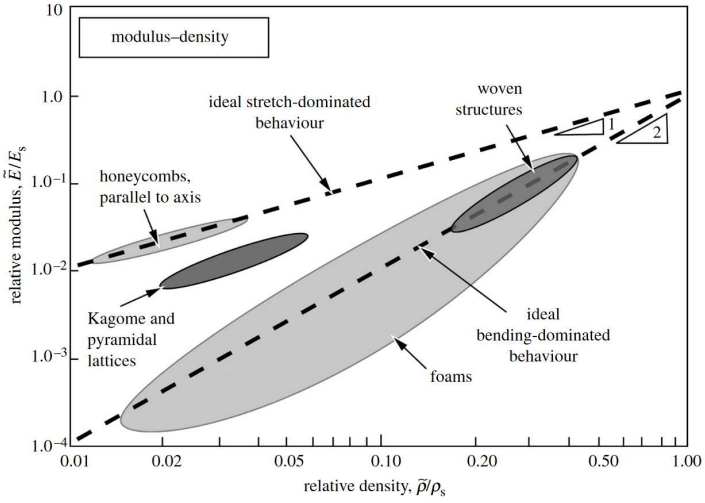

(a)

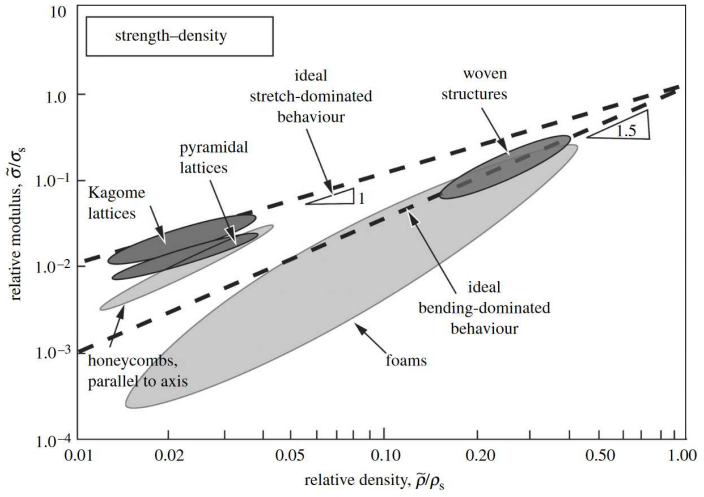

(b)

Figure 2.7: (a) Relative elastic modulus and (b) relative strength plotted against relative density for cellular structures presenting distinct topologies. Extracted from [25].

2.3 Sources of carbon and their influence on processing and thermo-mechanical properties

Carbon, in its several forms, is one of the most important constituents of state-of-the-art refractories used in steel-making. It is frequently combined with other materials (generally oxides) such as alumina, magnesia, zirconia and silicon carbide, forming highly functional composites.

During the 1970's and 1980's, carbon-bonded materials spread out in the steel-making industry. Several patents were deposited concerning the processing and application of such refractories [55–57].

Rand *et al.* [58] listed the main reasons for carbon addition into steel-making refractories:

- Highly refractory character and thermal stability in non-oxidizing conditions;
- Poor wettability by polar liquids, particularly silicate-based slags;
- High thermal conductivity;
- Ability to modify thermal expansion coefficients and mechanical properties, consequently tuning the thermal shock behavior.

Motivated by the growing interest in carbon-containing composites, Rand and McEnaney [59, 60] wrote two important review papers about the carbonic resines and pitches, widely used as binder materials. The most important differences between the two carbon sources are related to their ability, or not, to generate graphite-like structures after thermal treatment [59].

The distinction between graphitizing and non-graphitizing carbons is illustrated in Figure 2.8. Both images resulted from a high resolution transmission electron microscope (TEM) analysis of sucrose and anthracene samples treated up to 1000 °C under argon atmosphere. Figure 2.8a shows an example of non-graphitizing carbon prepared by the pyrolysis of sucrose. The structure appears disordered and isotropic (the diffraction pattern of symmetrical rings confirms the isotropy). Figure 2.8b, on the other hand, shows the structure of a graphitizing carbon prepared by thermal treatment of anthracene. The structure contains flat carbon layers, packed tightly together with a high degree of alignment (the diffraction pattern confirms the preferential orientation).

The so-called graphitizing carbons tend to be soft and can be readily transformed into crystalline graphite by heating up to temperatures in the range between 2200 °C and 3000 °C. On the contrary, non-graphitizing carbon is usually hard, micro-porous and cannot be transformed into crystalline graphite even at temperatures above 3000 °C [62].

Carbon can present several crystallographic levels (between the glassy carbon and graphite crystals), depending on its source and treatment's conditions (temperature, atmosphere, pressure). Those intermediary organization levels are called non-graphitic carbon. They cannot be called amorphous since they present bi-dimensional order extension larger than 1 nm [17,63,64].

The first theory to explain non-graphitizing carbon sources was proposed by Franklin [63] in 1951. According to her model, the main reason why non-graphitizing carbons cannot self-organize at high temperatures is related to cross-linking bonds between carbon chars. As those cross-links are composed of covalent bonds, even if they are broken at high temperatures, the activation energy for the motion of entire crystallites would be too high, restricting their movement (Fig. 2.9a). Franklin did not discuss the origins of such cross-linking bonds.

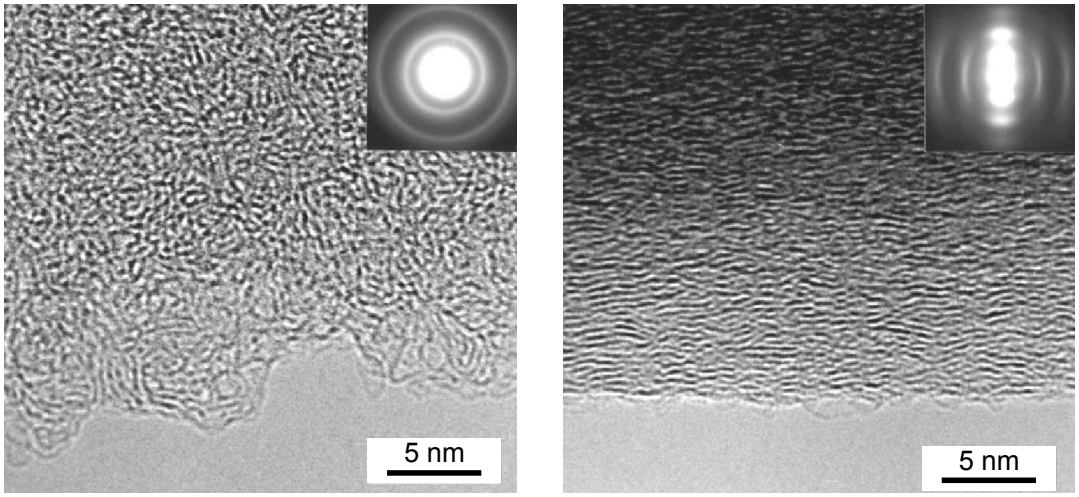

(a) sucrose (b) anthracene

Figure 2.8: High resolution micrograph of carbon prepared by pyrolysis of sucrose and anthracene under argon atmosphere at 1000 °C. Extracted from [61].

With the advent of high-resolution transmission electron microscopes in the 1970s, Ban *et al.* [65] were one of the first groups to examine non-graphitizing carbons. Images of polyvinylidene chloride (PVDC) thermally treated up to 2700 °C analyzed by those authors, apparently showed the presence of curved and twisted graphite sheets. Ban *et al.* suggested the ribbon model (Fig. 2.9b), where graphene layers are twisted and entwined, which would explain why those materials are non-graphitizing [65]. This model was the most accepted one, but still some characteristics of non-graphitizing carbons were not clarified. For instance, non-graphitizing carbons present high porosity even after being treated at high temperatures. Harris [62] commented that due to the high flexibility of the graphene layers, they would fold further together when treated at high temperatures and consequently the porosity would decrease, allowing the material to reduce its surface energy, which is not the case.

After the fullerene[†] discovery in 1985 [66], Harris and colleagues [61,62,64] revisited the high resolution TEM images of non-graphitizing carbons. They discovered the presence of some carbon nanoparticles (presenting an onion-like structure) similar to fullerenes. After several analyses they proposed that non-graphitizing carbons present fullerene-like structures, i.e., carbon atoms are not only positioned in a hexagonal honeycomb pattern (like in graphene sheets), but some are located in pentagonal or heptagonal cells. As a result, the carbon sheets would be curved or twisted (Fig. 2.9c). According to the theory, complete fullerene structures could be formed at high temperatures. Hence, this model satisfies the high microporosity condition after the material faces high temperatures (fullerene structures are relatively stable [62, 66]). Burian and Dore [67] used Raman spectroscopy to analyze carbons prepared from sucrose (non-

[†]Fullerene (Fig. 2.13b) is a carbon allotrope in form of a hollow sphere. The first fullerene discovered was C_{60} where carbon is arranged in a hollow sphere containing 12 pentagonal and 20 hexagonal faces [66]. The most surprising fact to the scientific community was that carbon arranged in pentagonal or heptagonal shapes could be stable at high temperatures.

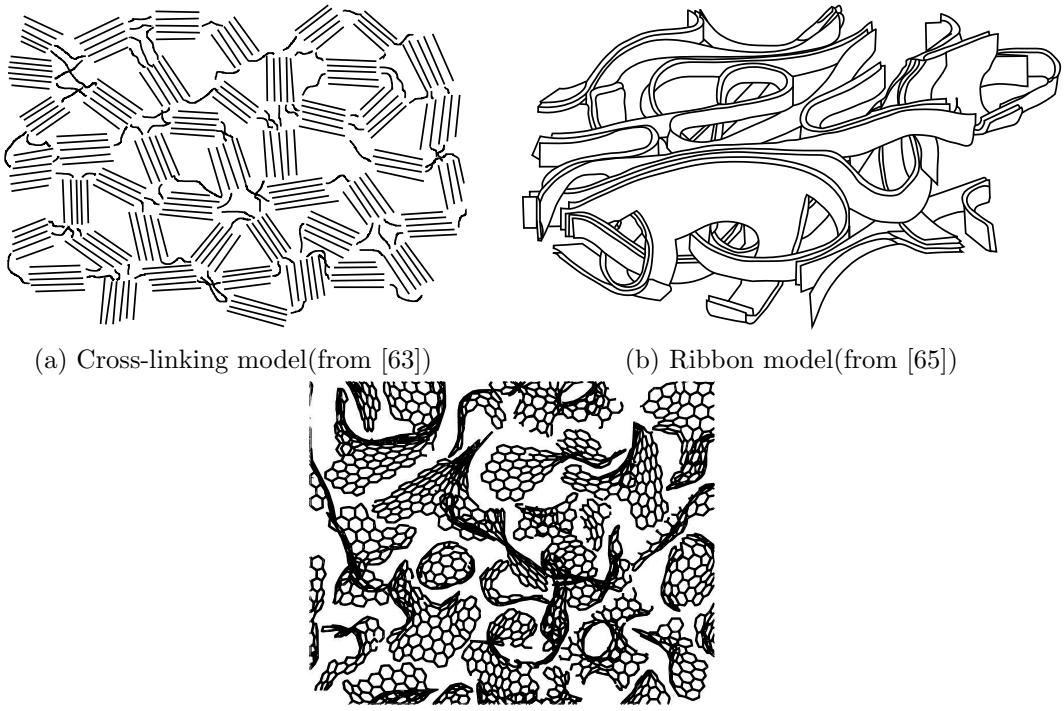

(a) Cross-linking model(from [63])

(b) Ribbon model(from [65])

(c) Fullerene model(from [62])

Figure 2.9: Structural models of non-graphitizing carbon sources.

graphitizing) and found clear evidence for the presence of fullerene- and nanotube-like elements in carbon. Nowadays, the fullerene model is the most accepted one [68].

2.3.1 Pitch

Pitch is a complex material obtained from the thermal decomposition of organic precursors. Coal tar pitch is the residue of the coal tar heavy or anthracene oil distillation. It is a mixture of many organic compounds, with the precise composition varying according to the tar source and distillation conditions. It was the first organic binder used in the refractory production, and it is still applied in modern technologies mainly due to its high carbon yield and possibility of being graphitized [7, 58, 59].

The usual properties of interest of coal tar pitch are related to carbon yield, boiling ranges, solubility in specific solvents and softening points. Materials with similar softening points and solubility in a common solvent (quinoline, for instance) may present quite different properties during carbonization [58].

The molecular structure of the pitch determines its rheological and wetting characteristics as well as its behavior during pyrolysis. The properties of pitch-bonded parts will be strongly influenced by the wetting of the other raw materials by the pitch during mixing and the early stages of carbonization [59].

Carbonic matrix derived from pitches tend to be anisotropic, a product of the development of layers during the growth and coalescence of mesophase spheres in the initial stages of pyrol-

ysis [69]. The mesophase behavior correlates to two main factors: (a) the non-existent crossing bonds between carbonic chains and (b) the aromaticity of pitch's molecules granting a low rigidity characteristic of a crystalline liquid. This crystalline liquid self-aligns as the temperature increases, allowing the formation of graphite lamellas. Plastic deformation during this stage, due to externally applied stresses or the formation of gaseous by-products of pyrolysis, may disrupt long range ordering of the mesophase resulting in a finer microstructure [59, 70].

When the mesophase is carbonized, a considerable shrinkage followed by microcracking takes place. These microcracks follow the lamellar orientation, since the direction of greatest shrinkage is perpendicular to the molecular layer stacks.

The pitch pyrolysis is a very complex phenomenon involving depolymerization in parallel with thermal decomposition of functional groups, in which primary reaction products compete for the donatable hydrogen for stabilization [59, 71, 72].

Brooks and Taylor [73] described the pitch graphitization during pyrolysis. Firstly the pitch melts and becomes an isotropic pitch-like material of plastic consistency. With rising temperatures (generally above 400 °C), some mesophase spheres (Fig. 2.10a) are noticeable in the pitch mass (the spheres nucleation appears to be related to the presence of insoluble particles). These spheres increase in size as function of time and temperature. At a certain size they start to interfere with one another (including coalescence of spheres) and a mosaic pattern is recognizable (Fig. 2.10b). Finally, the mesophase changes to a solid semi-coke. The semi-coke keeps the mosaic texture and lamellar orientation, but its order level increases with increasing temperature (Fig. 2.10c). Marsh [74] proposed a simplified schematic illustration (Fig. 2.11) of a graphitizable carbon source.

The relation between the presence of insoluble particles and the mesophase nucleation has been studied to catalytically graphitize pitch materials, attaining satisfactory graphitization levels at temperatures lower than 2200 °C [75, 76].

The main disadvantage of pitch is related to its emission of toxic substances, including carcinogenic ones, during pyrolysis. The polycyclic aromatic hydrocarbons (PAHs), benzo[a]pyrenes for instance, are the most concerning ones [7, 62, 77]. Anthracene-based pitches usually present a benzo[a]pyrene concentration of up to 15,000 ppm. Levels higher than 50 ppm are already considered dangerous by the German hazardous materials regulation (TRGS 551) and a labeling obligation comes into effect [7, 78].

2.3.2 Modified coal tar pitch - Carbores® P

As discussed in the previous section, one of the biggest disadvantages of using pitch is related to its toxicity. The high concentration of polycyclic aromatic hydrocarbons (PAHs), like benzo[a]pyrenes, increases the concern of using this carbon source.

Carbores® P, was developed by the company Ruetgers (Germany) to address the safety concerns. It presents a concentration of benzo[a]pyrenes lower than 300 ppm. [17, 79]

It is a modified coal-tar pitch powder, hence Carbores® P is graphitizable [80]. According to the material's safety data sheet, it has a softening range between 240 °C and 250 °C and decomposes at around 400 °C.

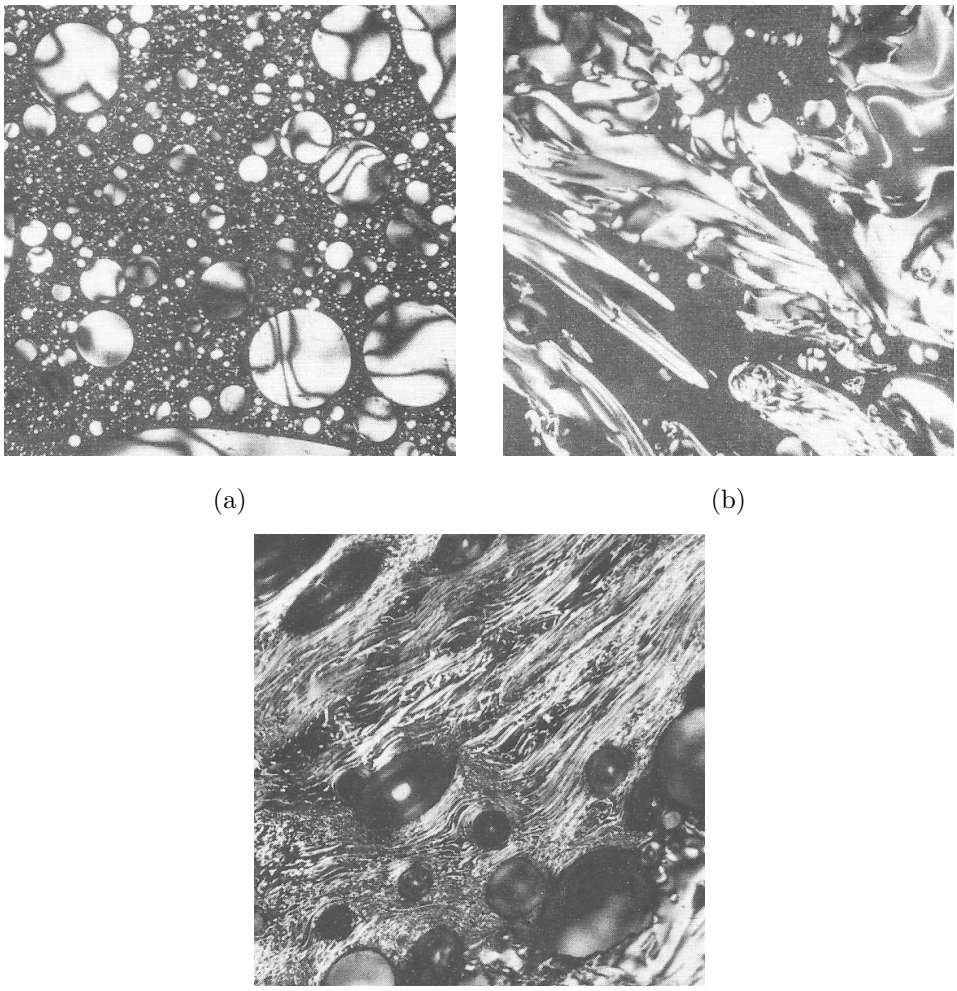

(a) (b)

(c)

Figure 2.10: Development of mesophase during the pyrolysis of a petroleum pitch. a) Separated mesophase spheres. b) Deformed regions of coalesced mesophase spheres. c) Semi-coke stage. Extracted from [59].

2.3.3 Resin

Phenolic resins from furfurylalcohol are good carbon precursors to refractory binders due to their high carbon yield. They are usually non-graphitizing and show decreasing viscosity with increasing temperature above the glass transition. In general they present a thermosetting character and above 100 °C extensive cross-linking takes place, giving the resin a rigid and insoluble behavior. [59]

Novolak resins are obtained when a precursor with phenol/formaldehyde molar ratio greater than 1 is heated in the presence of acid catalyst. Since the formaldehyde has completely reacted, this type of resin requires hexamine for the final cross-linking (cure) stage.

The pyrolysis mechanisms of phenolic resins are quite complex, since condensation, oxidation,

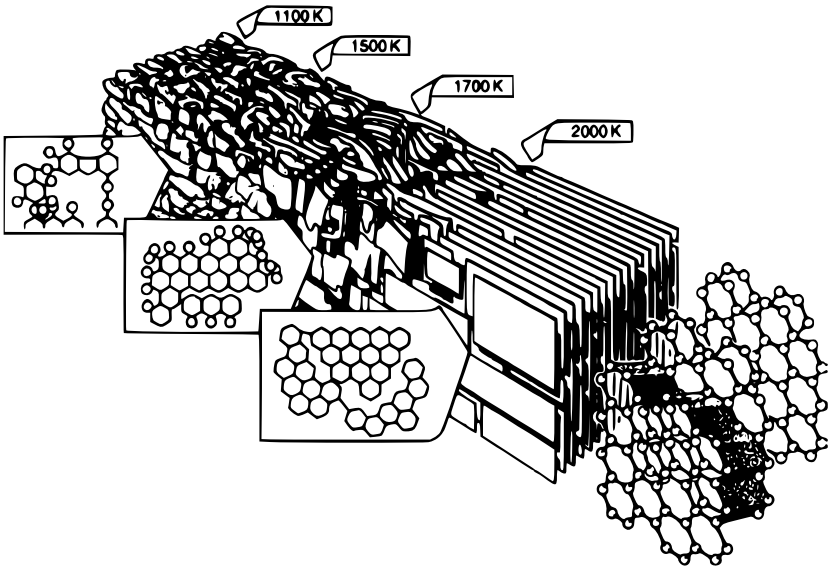

Figure 2.11: Structural changes which occur during the heat treatment of a graphitizable carbon. Extracted from [74].

dehydration and decomposition reactions occur simultaneoulsy [81]. The evolution of volatiles during the pyrolysis of a resol resin is schematically shown in Figure 2.12.

As it can be seen, the evolution of water release ranges from 200 °C up to 900 °C, whereas CH_4, CO, H_2 and CO_2 are released at temperatures over 400 °C. The low temperature dehydration is related to the removal of the oxygen incorporated into the structure during air curing and the heat treatment produces dihydroxybenzophene bonds, releasing H_2O [59, 82, 83]. Rand and McEnaney [59] described that the overall volatiles release is determined by the molar ratio of phenol to hexamine, being this variable a possible tuning parameter.

The presence of oxygen and a higher number of alifatic groups hinder the carbon fixation, since they facilitate the rupture of the polymeric structure and, consequently, the formation of volatiles. Therefore, an alternative to reduce the volatiles release is a pre-oxidation step of the resins. However, this procedure generally increases the resins viscosity, affecting the processing of the refractory [17].

Compared to pitch, resins reduce the refractory porosity. This characteristic is of great importance, since above a certain carbon yield, the oxidation rate is mostly determined by the refractory's open porosity [17, 84, 85].

McEnaney and Rand [60] established a comparative summary of properties of pitch- and resin-derived carbons (Table 2.1).

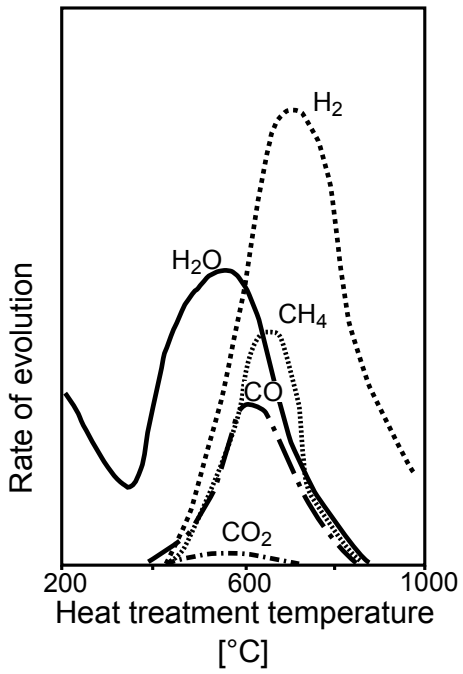

Figure 2.12: Evolution of volatiles from phenol-formaldehyde resin during carbonization (extracted from [59]).

Property	Pitch-carbons	Resin-carbons
Graphitizability	High	Low
Porosity	Mainly macroporous	Mainly microporous
Strength	Lower	Higher
Elastic modulus	Lower	Higher
Fracture toughness	Higher	Lower
Thermal conductivity	Higher	Lower
Calculated Thermal Shock Parameter R_{st}	Higher	Lower

Table 2.1: Comparative summary of properties of pitch- and resin-derived carbons. Adapted from [60].

2.3.4 Graphite

Graphite is the most stable form of carbon under standard ambient conditions and one of the most important raw materials for the refractory industry. In 2015, the refractories industrial sector of the United States alone consumed 10,080 tonnes of natural graphite [86].

According to Rand *et al.* [58], if one word had to be used to describe the graphite's behavior, it would be **anisotropy**. Due to its planar layered structure (see Figure 2.13), graphite presents distinct behaviors (thermal, mechanical and chemical) depending on the load direction. The

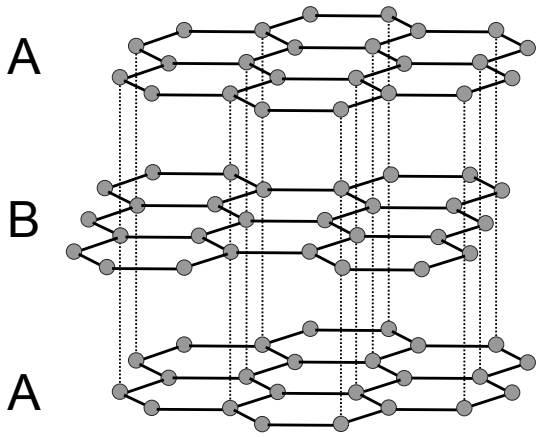

(a) Graphite planar layered structure.

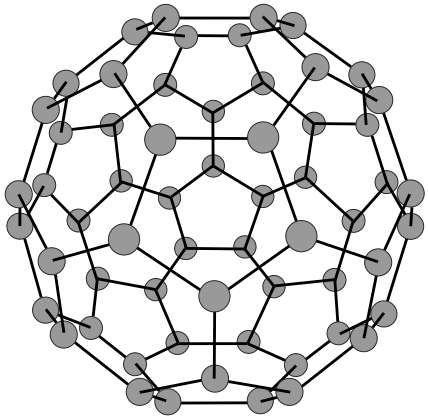

(b) Fullerene C_{60} structure.

Figure 2.13: Graphite and Fullerene C_{60} structures.

carbon-carbon bond (covalent) within the plane is, particularly, strong with an interatomic distance of 0.142 nm. The bonding (van der Waals) in between the planes is weak with a planar spacing of 0.304 nm.

Apart from its high refractoriness, graphite delivers other important features and properties to the final refractory material, such as: low effective thermal expansion coefficient, high thermal conductivity, high flexibility and consequent high thermal-shock resistance [18]. Complementary advantages of using graphite in the refractory composition come from its chemical and volumetric stability [87]. For carbon-based refractories applied in the slag line, the high thermal conductivity of graphite favors the formation of a viscous metallic layer on the refractory's hot face, protecting it from the typical abrasion/corrosion mechanisms that this region is usually exposed to [88].

Bitencourt and Pandolfelli [70] described in detail the mutual relationship between graphite and stable oxides, such as MgO and Al_2O_3, for siderurgical applications. Normally, graphite presents low wettability for molten oxides contained in slags (mainly silicates). However, it is wetted by molten iron [89]. Therefore, the liquid metal could react with the refractory material, increasing its corrosion. The stable oxides, in turn, do not present the same non-wettability behavior toward slags, but are poorly wetted by liquid iron. Therefore, the combination of both material classes is of great interest. In this mutualistic system, graphite will protect the oxides from slag corrosion, while the oxides will preserve graphite from corrosion by molten iron.

Despite the advantages of adding graphite in the refractory composition, its geometry and low wettability with the dispersing media (water, pitch or resin) demand a high effort during the refractory processing, and consequent higher amount of liquid [77]. Another important limitation of graphite is its oxidation resistance. At temperatures above 400 °C, graphite is extremely susceptible to react with oxygen, carbon dioxide and other oxidizing gases [87].

One possibility to reduce the required amount of dispersant is to partially substitute the graphite flakes with micro-crystalline graphite. This variant presents lower crystallinity and higher concentration of polar groups, enabling a better interaction with the dispersing medium and, consequently, higher wettability [70].

The anisotropy of graphite is also manifested by its chemical behavior. Oxidation usually starts at the edges of the graphene layers, although impurities in the graphite might perform a catalytic role, dominating this behavior. In Figure 2.14a, one can observe the hexagonal oxidation front of pure graphite flakes (respecting the crystallographic orientation), whereas Figure 2.14b illustrates the role of impurities catalyzing the oxidation, resulting in a rounded oxidation front.

Figure 2.15 shows how the amount of graphite in an alumina-graphite composite influences the refractory effective thermal expansion coefficients. The samples were uniaxially pressed at 150 MPa and then fired up to 1600 °C under reduced atmosphere. During pressing, graphite tends to be perpendicularly aligned to the pressing direction. Therefore, the difference of the thermal expansion coefficients in the two directions is mainly related to crack formation due to the graphite anisotropy [58].

2.3.5 Carbon Black

Carbon black consists of quasi-spherical particles ranging from 10 nm to about 500 nm in size. It is formed by the incomplete combustion or cracking of hydrocarbon gases and vapors derived from petroleum sources. The first X-ray diffraction study of carbon black was carried out by Warren in the 1930s, who demonstrated the presence of graphite-like carbon of short-range order [90].

Lum *et al.* verified that the addition of carbon black in refractories bonded by resins reduced the volatiles release during firing. This behavior was related to the interaction of these volatiles with functional groups located on the carbon black surface [91]. Ewais reported an increase of mechanical strength of magnesia-graphite bonded by pitch, when adding carbon black [19]. However, the mechanisms behind this strengthening were not clear, but one could correlate that to a lower volatiles release.

Conversely to Lum *et al.* [91], a study conducted by Bahtli *et al.* [92], concluded that substituting flake graphite with pyrolytic carbon black impaired the thermal shock resistance of the

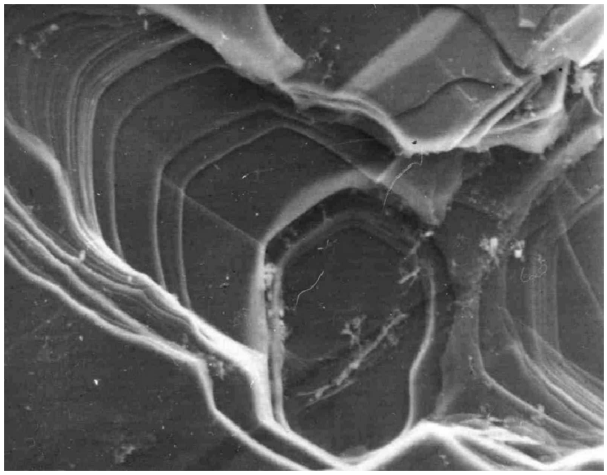

(a) Hexagonal front of graphite oxidation

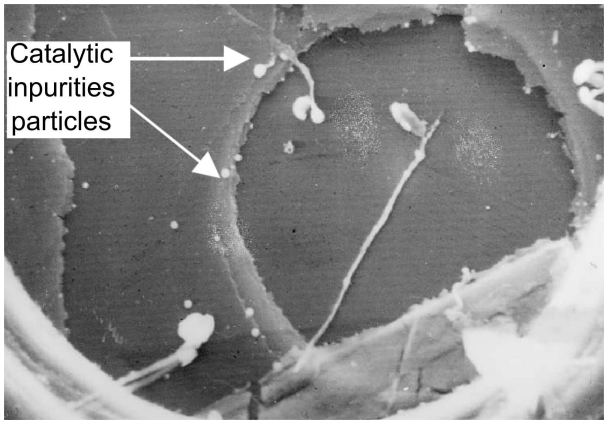

(b) Rounded front of graphite oxidation due to catalytic impurities

Figure 2.14: SEM images of oxidation etch pits on pure (a) pure graphite flake and (b) graphite flakes with catalytic impurities. Extracted from [58].

refractory. This phenomenon was mainly related to a higher porosity due to the carbon-black volatilization. One of the drawbacks of this study was that the varying amount of residual carbon did not allow a direct comparison. The authors analyzed the fracture surfaces of the samples after 3-point bending tests and concluded that, due to a higher porosity related to the carbon black volatilization, most of the cracks of those samples were intergranular. On the other hand, the samples containing flake graphite presented inter- and trans-granular cracks, proving the deleterious effect of an excess of carbon black on the matrix resistance.

The classification of carbon black as graphitizable or non-graphitizable carbon source is still an open discussion. If one would consider graphitizable carbons only the ones presenting a bi-dimensional long-range order, then certainly carbon black must be considered a non-graphitizabe source [62]. On the other hand, carbon black presents a certain graphitization level, but due to its format (Figs. 2.16a and 2.16b), at the end of its graphitization stage, faceted

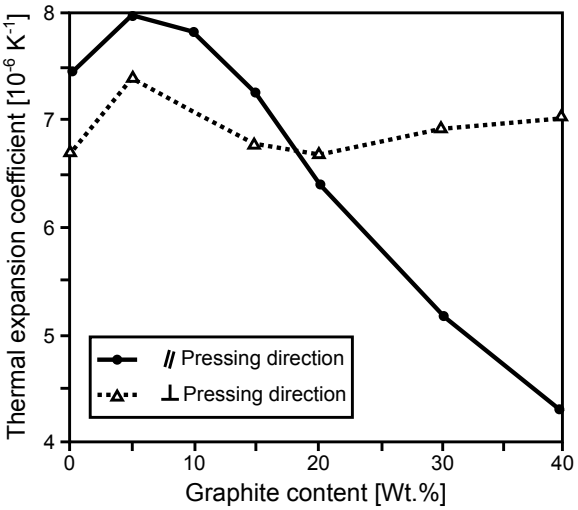

Figure 2.15: Thermal expansion coefficient of alumina-graphite composite pressed at 150 MPa and fired up to 1600 °C under inert atmosphere. Extracted from [58].

particles with residual microporosity are generated (Fig. 2.16c). Carbon black is considered a carbon filler and is used to increase the carbon yield and tune the particle size distribution of carbon-bonded refractories. [17]

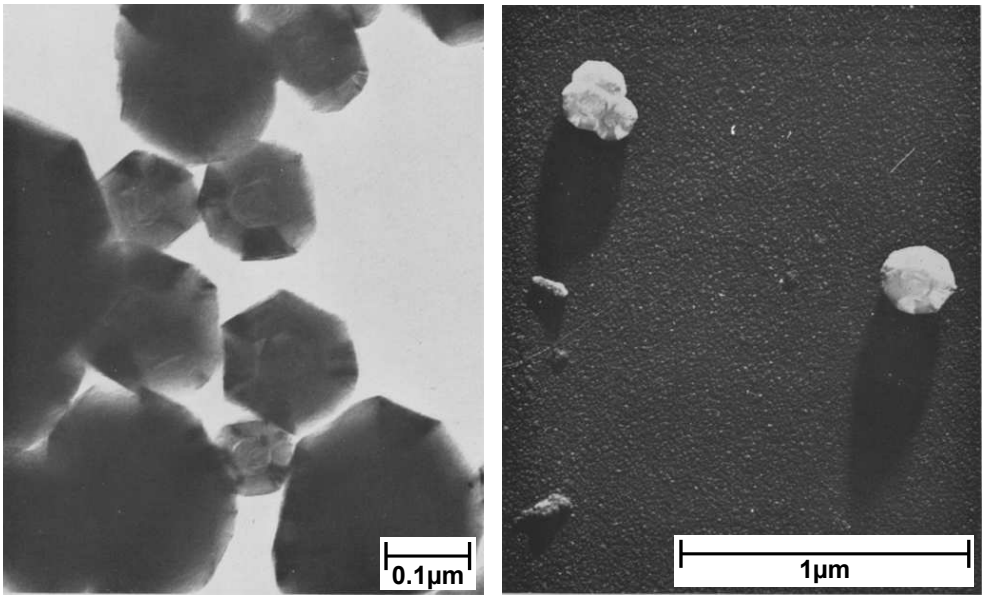

(a) (b)

(c)

Figure 2.16: (a) Scanning electron micrograph of P-33 carbon black (extracted from [93]). (b) Shadowed electron micrograph of P-33 carbon black (extracted from [93]). (c) Model of structure of a thermal carbon black after graphitization (extracted from [94]).

3 Materials and Methods

As explained in the Introduction, this thesis addresses problems related to bulk and cellular carbon-bonded materials. In order to facilitate the readers' interpretation, the Materials and Methods part was divided into three main topics. Section 3.1 treats the non-linear Young's modulus behavior of carbon-bonded alumina at high temperatures. Motivation, material composition, experimental and modelling approaches are also described. Inspired by the results of this investigation, correlating the thermo-mechanical properties of bulk Al_2O_3-C with its processing route (see Section 4.1.1), Section 3.2 assesses the influence of the processing route on the ceramic material distribution of carbon-bonded alumina foam filters. Motivation, material composition, processing parameters and experimental approaches are detailed described. A deep examination of three distinct processing routes was performed. From those, the two best processing routes were selected for investigating the up-scaling of the foam filters' geometries (Section 3.3). In this study, the method to characterize highly porous structures via X-ray computed tomography (µCT) was validated and a wider comprehension of how the processing route influences the mechanical properties of ceramic foam filters was achieved.

3.1 Non-linear Young's modulus behavior of carbon-bonded alumina at high temperatures

3.1.1 Motivation

The complex behavior of the Young's modulus of composite materials as a function of temperature has challenged the scientific community in the last decades [95–97]. Various models [98–102] and theories [103, 104] have been proposed to explain non-conventional features. Understanding the role of the thermo-mechanical properties mismatch among different phases in such materials [105, 106] can guide their design and improve their in-service operation.

Carbon-bonded alumina (Al_2O_3-C), a key-piece product in the steel industry, presents non-conventional Young's modulus behavior at high temperatures [104]. A relevant number of steel casting components such as entry nozzles, monoblock stoppers and ladle shrouds are based on Al_2O_3-C, which is also well-known for its excellent thermal-shock resistance [11,107]. Therefore, improving its thermo-mechanical properties can result in a positive impact on the steel-making chain, reducing the costs and energy consumption.

Werner *et al.* [104] analyzed the Young's modulus (E) behavior of fired Al_2O_3-C samples by the impulse excitation technique up to 1450 °C. They suggested that the non-conventional E increase as function of temperature was related to the thermal expansion mismatch between alumina particles and the matrix.

No information about the Young's modulus of carbon-bonded alumina green samples as function of temperature was found in the literature. Analyzing this feature would allow un-

derstanding the origins of the non-linear behavior, giving to the scientific community a global vision on the way mechanical properties and material's processing parameters correlate.

The purpose of the present study is to understand the Al_2O_3-C non-linear thermo-mechanical behavior [104, 108] by investigating its Young's modulus versus temperature profile, analyzing green and fired samples. The main differences with previous studies are the combination of experiments and finite element simulation (model materials) in macro and micro-scale perspectives.

The strategy adopted to model the Al_2O_3-C non-linear behavior is based on model materials microstructure simulation. Many authors applied the concept of model materials to understand the unusual behavior of complex composites [97, 109–111]. Model materials are simplified composites with, for instance, just two phases and well-defined geometries and properties. This includes, among others, the volume fraction of particles, the particle size and their distribution. The trends observed in the model analysis can be used to explain the behavior of the industrial heterogeneous ceramic materials.

Numerical simulation in conjunction with model materials became an effective analysis tool for researchers, improving the investigation capability and reducing the testing costs. However, suitable models and continuous comparison with experimental data are required to validate the model approaches.

Therefore, the aim of this Section is to characterize the Al_2O_3-C microstructure, correlating the micromechanisms acting during firing with the consequent mechanical behavior of fired samples.

3.1.2 Materials

The carbon-bonded alumina investigated in this study is based on a composition presented by Roungos and Aneziris [3]. The main difference with the current material was the use of a tabular alumina with no metal additives as anti-oxidants (Table 3.1).

Raw materials	Type or fraction	wt.%
Graphite	AF[a] /NFL[b]	30.0
Tabular alumina	0 - 0.5 mm	25.3
	0.5 - 1 mm	44.7
Novolac resin	liquid	2.0
	powder	4.0
Hexamethylenetetramine[c]		10.0

[a] $d_{50} = 18\mu m$ [104]

[b] $d_{50} = 160\mu m$ [104]

[c] Based on the resin content

Table 3.1: Composition of the carbon-bonded alumina used in this investigation

The general features of the raw materials used in this study were as follows: tabular alumina (T60/64, 99.5 % Al_2O_3, Almatis GmbH, Ludwigshafen, Germany), natural graphite (AF with

a carbon content of 96 - 98 %, and NFL with a carbon content of 92 - 94 %, both supplied by Graphite Kropfmuehl AG), liquid and powder Novolac resin (Momentive, Duisburg, Germany), and hexamethylenetetramine (Momentive, Duisburg, Germany) as a resin hardener.

The samples were produced by firstly mixing the components in a compulsory mixer (Maschinenfabrik Gustav Eirich GmbH & Co. KG, Hardheim, Germany). Secondly, bars ($150 \times 25 \times 25\,\mathrm{mm}^3$) were uniaxially pressed at 100 MPa [3] and then cured at 180 °C [112].

3.1.3 Experimental

Young's modulus measurement via impulse excitation technique (IET)

For the measurement* of the Young's modulus as a function of temperature $E(T)$, a furnace with an impulse excitation setup and controlled argon atmosphere was used (HTVP1600, IMCE, Belgium) [113] (Figure 3.1). The flexural natural frequency was measured at distinct temperatures within the range of 27 to 1000 °C. For calculating $E(T)$, according to Eq. (3.1), the procedure stated by ASTM-E1876 [114] was followed. In the equation, ϕ is a correction factor for accounting the finite thickness effect, ρ is the apparent density, L is the bar's length, f is the natural vibration frequency and w is the bar's thickness.

$$E(T) = \frac{0.9465\phi\rho L^4[f(T)]^2}{w^2} \tag{3.1}$$

Figure 3.1: Furnace equipped with an impulse excitation device and controlled argon atmosphere (HTVP1600, IMCE, Belgium). Figure extracted from [115].

Three just cured (JC) samples were heated up to 1000 °C and cooled to 27 °C for two cycles. The heating and cooling rate were approximately 1 K/min and 5 K/min for the first and second cycles, respectively. The lower heating rate during the first cycle intends to reduce the damage

*It must be highlighted that the Young's modulus measurements were conducted in cooperation with Dr.-Ing. Joern Grabenhosrt from the Institute of Ceramic, Glass and Construction Materials of the TU Bergakademie Freiberg. The experimental design and the results analysis were mainly performed by the author of the thesis.

caused by the release of resin volatiles. Dwell times of 5 h and 1 h were applied at 1000 °C for the first and second cycles, respectively. Measurements were taken at every 10 °C variation. The first cycle represented the sample firing, whereas the second one was related to the behavior of a fired specimen.

Thermogravimetric analysis (TGA)

The thermogravimetric analysis of bulk samples ($\approx 100g$) from 40 °C up to 1000 °C was conducted in a furnace equipped with a scale (Figure 3.2, Nabertherm LHT 04/16 SW, Germany), with values being recorded at every 10 K variation. The heating rate was 5 K/min. Due to the high likelihood of carbon-bonded alumina to oxidate, its firing must be handled in an oxygen-free atmosphere. The firing of samples was carried out inside a retort filled with calcined petcoke to satisfy that condition [116].

The investigation was divided into two steps. The first one involved a thermogravimetric analysis of the petcoke without the sample, as it is known that it will partly oxidate in the presence of oxygen (white test). The second step included a thermogravimetric analysis of the carbon-bonded alumina sample inside a retort filled with petcoke (real test). In order to isolate the carbon-bonded alumina pyrolysis behavior, the difference between the white and the real test was calculated.

Figure 3.2: Furnace equipped with a scale used to measure the mass loss variation as function of temperature (Nabertherm LHT 04/16 SW, Germany). Figure extracted from [117].

Scanning Electron Microscopy (SEM)

The effect of the thermal treatment on the samples' microstructure was assessed by scanning electron microscopy (XL 30, Philips, Amsterdam, Netherlands)[†]. Samples treated with three distinct thermal schedules were analyzed: The so-called just cured (JC) samples (180 °C), fired

[†]It must be highlighted that the SEM operation was conducted in cooperation with Dr.-Ing. Gert Schmidt from the Institute of Ceramic, Glass and Construction Materials of the Technische Universität Bergakademie Freiberg. The images analyses and description were performed by the author of the thesis.

for two heating and cooling cycles up to 1000 °C (HT2×), and treated up to an intermediate temperature of 500 °C single cycle (HT1×).

Porosity measurements

The relationship between the thermal treatment and the apparent porosity was also investigated. All porosity measurements applied the water immersion technique, following the standard EN 993-1.

3.1.4 Numerical simulation

The numerical simulation procedure followed the model material approach [97, 110, 111] in order to investigate the effective Young's modulus behavior as a function of temperature of carbon-bonded alumina. For that purpose, Franklin and Tucker [103] suggested a theory that was complemented by Werner *et al.* [104], where the increase of the effective Young's modulus with the temperature is a consequence of the closure of gaps between the particles and the matrix, which is related to the thermal expansion mismatch of the phases.

To investigate the effective Young's modulus variation as a function of temperature, virtual compression tests at different temperatures were simulated. The computational geometry was a simplified 2D composite model comprising alumina and graphite particles dispersed in a continuous carbonaceous matrix. The particles' location was not homogeneous and gaps between the particles and the matrix were considered, as in the real condition. For the numerical simulation, the commercial software ABAQUS® was used. The analysis results were compared to the behavior of the second heating cycle of the Young's modulus experimental values.

The geometry was firstly generated with a code for the design of random virtual microstructures developed by the author of the present manuscript. The code was written in the MATLAB software and its algorithm is presented in the Appendix A.1 (Page 111). Each particle dimension and position of the analyzed geometry are also supplied in Table A.2.1 (Page 125).

A simplified bi-modal particle size distribution with two distinct radii of $R = 0.5\,\text{mm}$ and $r = 0.25\,\text{mm}$ was assumed for the coarse alumina (Fig. 3.3). The coarse graphite particles were considered as ellipses with an aspect ratio of 1/5 and 0.5 mm as their largest dimension. The particles' size was assumed as simplified values from the material particle size distribution (Appendix A.3, Page 141). The virtual sample dimensions were $L \times L$, where $L = 20 \cdot R$.

The designed geometry follows the real volume fraction of the coarse particles as calculated from Table 3.1 and particle size distribution by considering a theoretical density of $3.95\,\text{g}\cdot\text{cm}^{-3}$ for the alumina [118], $2.2\,\text{g}\cdot\text{cm}^{-3}$ and $1.5\,\text{g}\cdot\text{cm}^{-3}$ for graphite [119] and glassy carbon [120], respectively. The material comprised 53 vol. % of alumina (12 vol. % considered coarse and 41 vol. % fine), 41 vol. % of graphite (17 vol. % coarse and 24 vol. % fine) and 6 vol. % of glassy carbon.

The graphite's Young's modulus E and thermal expansion coefficient α were considered orientation-dependent, with different values between the parallel ($_{//}$) and perpendicular ($_{\perp}$) directions of the graphene basal plane. The α behavior as a function of temperature is presented in Fig. 3.4, whereas the Young's moduli were considered to be constant with $E_{//} = 795\,\text{GPa}$ and $E_{\perp} = 35\,\text{GPa}$ [121,122]. The ellipses were assumed to present the $_{//}$ properties along their major axis and the $_{\perp}$ properties along their minor axis.

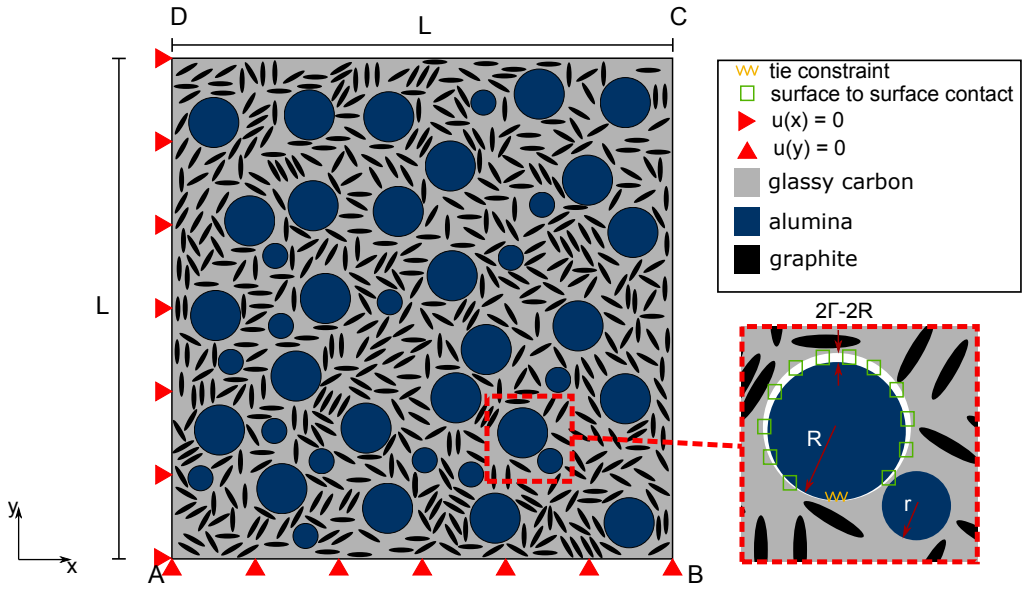

Figure 3.3: Tri-modal particle size microstructure geometry: Bi-modal distributed alumina as well as graphite inclusions embedded in a carbon matrix.

The thermo-mechanical properties of the alumina (Fig. 3.5) were considered the same as those reported by Werner *et al.* [104]. The Poisson's ratios of graphite, alumina, and matrix were kept constant at 0.20, 0.22 and 0.20, respectively.

As a simplifying assumption, the matrix was considered to be a continuous phase presenting the mechanical properties of a 41 vol. % alumina dispersed in glassy carbon (fine graphite was not considered for this study composition). Its thermo-mechanical properties were calculated following the Hashin-Shtrikman [124] and Fahmy-Ragai [125] models. The first model was applied for the Young's modulus prediction, whereas the latter was employed for the thermal expansion coefficient calculation.

The Hashin-Shtrikman (HS) model calculates the upper (HS^+) and the lower (HS^-) bounds of the mechanical properties, attesting that independently of the particles' format and distribution, the composites' effective property should lie within those limits [124]. Both bounds (HS^+ and HS^-) and their average (HS^*) were considered for the Young's modulus of the matrix.

The bounds equations are hereinafter expressed by the equations (3.2) and (3.3), where ^{u} means upper bound, ^{l} the lower bound, $_{gc}$ represents the glassy carbon, $_a$ refers to the alumina, V to the volume fraction, K and G represent the bulk and the shear modulus, respectively.

$$E_m{}^l(T) = \frac{9K_m{}^l(T) \cdot G_m{}^l(T)}{3K_m{}^l(T) + G_m{}^l(T)} \tag{3.2}$$

$$E_m{}^u(T) = \frac{9K_m{}^u(T) \cdot G_m{}^u(T)}{3K_m{}^u(T) + G_m{}^u(T)} \tag{3.3}$$

$$K_m{}^l(T) = K_{gc}(T) + \frac{V_a}{\frac{1}{(K_a(T) - K_{gc}(T))} + \frac{3\,(1 - V_a)}{(3K_{gc}(T) + 4G_{gc}(T))}} \tag{3.4}$$

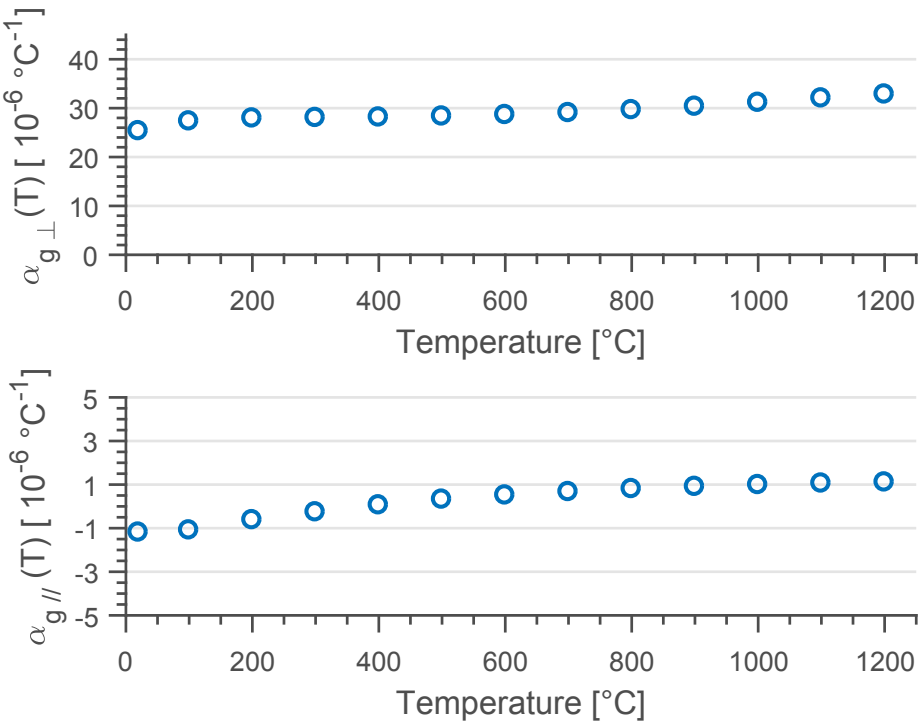

Figure 3.4: Polycrystalline graphite thermal expansion coefficient (α) perpendicular ($\perp$) and parallel ($//$) to the graphene basal plane as function of temperature. Extracted from Tsang et al. [123].

$$K_m{}^u(T) = K_a(T) + \frac{(1 - V_a)}{\frac{1}{(K_{gc}(T) - K_a(T))} + \frac{3V_a}{(3K_a(T) + 4G_a(T))}} \tag{3.5}$$

$$G_m{}^l(T) = G_{gc}(T) + \frac{V_a}{\frac{1}{(G_a(T) - G_{gc}(T))} + \frac{6\,(K_{gc}(T) + 2G_{gc}(T))\,(1 - V_a)}{5G_{gc}(T)\,(3K_{gc}(T) + 4G_{gc}(T))}} \tag{3.6}$$

$$G_m{}^u(T) = G_a(T) + \frac{(1 - V_a)}{\frac{1}{(G_{gc}(T) - G_a(T))} + \frac{6\,(K_a(T) + 2G_a(T))\,V_a}{5G_a(T)\,(3K_a(T) + 4G_a(T))}} \tag{3.7}$$

The Fahmy-Ragai [125] (FR) model was employed to calculate the matrix effective thermal expansion coefficient α_m, equation (3.8). The glassy carbon properties are presented in Fig. 3.6. The values were extracted from Zhao *et al.* [126] and Werner *et al.* [104], respectively. The final matrix properties are presented in Fig. 3.7.

$$\alpha_m(T) = \alpha_{gc}(T) - \frac{3\,(\alpha_{gc}(T) - \alpha_a(T))\,(1 - \nu_{gc})\,V_a}{\frac{2E_{gc}(T)}{E_a(T)}\,(1 - 2\nu_a)\,(1 - V_a) + 2V_a\,(1 - 2\nu_{gc}) + (1 + \nu_{gc})} \tag{3.8}$$

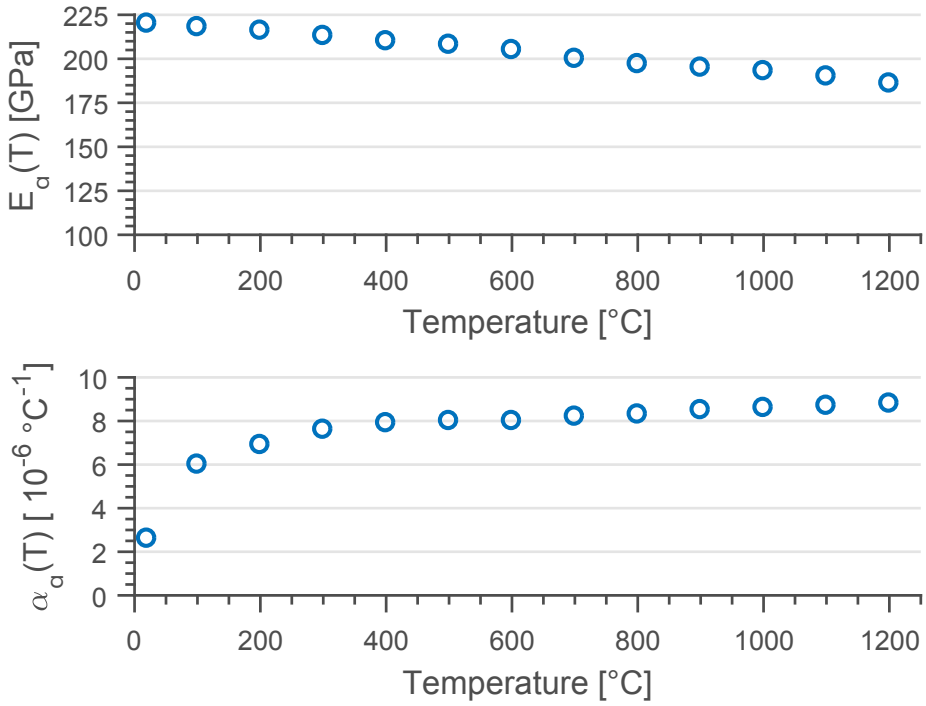

Figure 3.5: Tabular alumina Young's modulus (E) and thermal expansion coefficient (α) as a function of temperature. Extracted from Werner et al. [104].

The particles' gap size was considered to be $2\Gamma - 2r^*$ (Fig. 3.3), where $r^* = r$ or R and Γ represents the particles' initial and thermally expanded dimensions, respectively. Γ was calculated according to the equation (3.9), in which it is a function of r^*, the average thermal expansion coefficients of the matrix $\bar{\alpha_m}$ and the particles $\bar{\alpha_i}$, as well as of the temperature variation ΔT and of a small normal-random perturbation (*normrnd*) [127]. The latter intends to represent the non-uniform gap size distribution in real materials, generating random numbers from a normal distribution in which the mean and standard deviation were considered to be $\mu = \Delta T$ and $\sigma = 50\,^{\circ}\mathrm{C}$, respectively. The average coefficient of thermal expansion (CTE) values were considered to be $\bar{\alpha_m} = 6.0{\cdot}10^{-6}\,^{\circ}\mathrm{C}^{-1}$ for the matrix, $\bar{\alpha_i} = 8.0{\cdot}10^{-6}$ and $28.8{\cdot}10^{-6}\,^{\circ}\mathrm{C}^{-1}$ for the alumina and graphite, respectively. The temperature variation $\Delta T = 800\,^{\circ}\mathrm{C}$ was calculated as the difference between the final $T \approx 1000\,^{\circ}\mathrm{C}$ and the curing $T \approx 200\,^{\circ}\mathrm{C}$ temperatures. In all simulations, 5 % of the particles were considered without gaps, which again resulted in a better representation of the non-uniformity of the real condition.

A small displacement was applied at the sample's edge CD, imposing -0.0025 % strain in the y direction. The reaction force due to this displacement was calculated, and then, the effective stress in the y direction was obtained. Applying Hooke's law, it was possible to calculate the effective Young's modulus at distinct temperatures. A similar procedure, but with different interaction among phases, was applied by Joliff *et al.* [102] for an alumina-glass composite, although the tests simulated by those were tensile and not compressive ones.

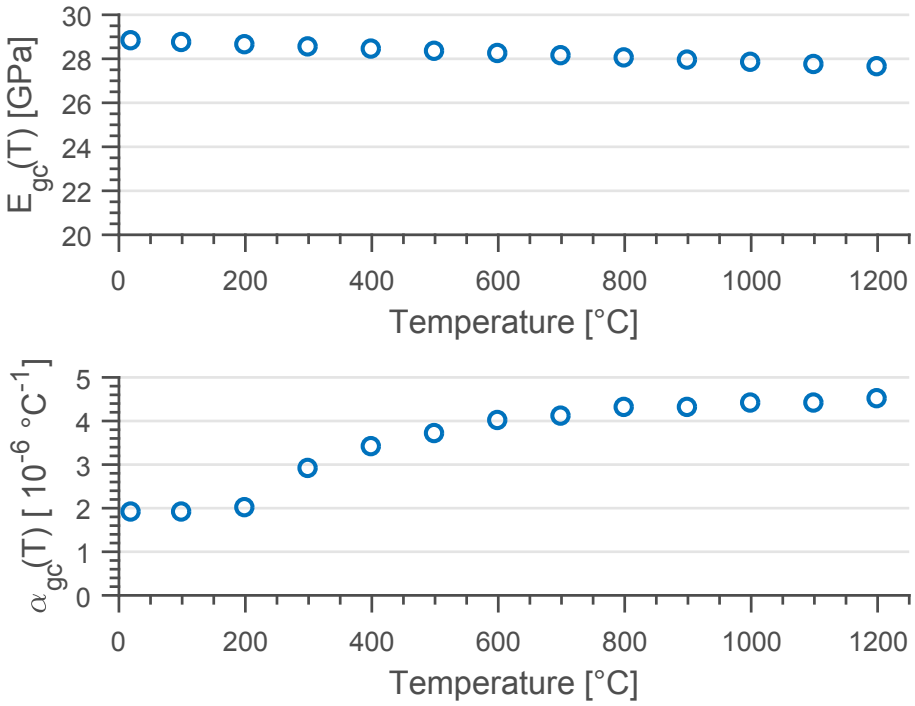

Figure 3.6: Glassy carbon Young's modulus (E) and thermal expansion coefficient (α) as a function of temperature. E and α were extracted from Zhao et al. [126] and Werner et al. [104], respectively. The thermal expansion coefficient was considered to be the same for the temperatures below 200 °C.

$$\Gamma(r^*, \mu, \sigma, \bar{\alpha_m}, \bar{\alpha_i}) = r^* \cdot [1 + (\bar{\alpha_i} - \bar{\alpha_m}) \cdot normrnd(\mu, \sigma)] \tag{3.9}$$

In Fig. 3.3, it is possible to visualize the model and attest its random particle distribution. The boundary conditions of the simulations were assumed as follows:

- y direction displacement restriction at the edge AB;
- x direction displacement restriction at the edge AD;
- Perpendicularity condition between AB and BC edges;
- Perpendicularity condition between AD and CD edges;
- Surface to surface contact between the particles and matrix surfaces (normal contact – hard behavior [128]);
- Tie constraint in a small portion ($\approx 8\%$) of the particle and matrix surfaces to improve the analysis convergence.

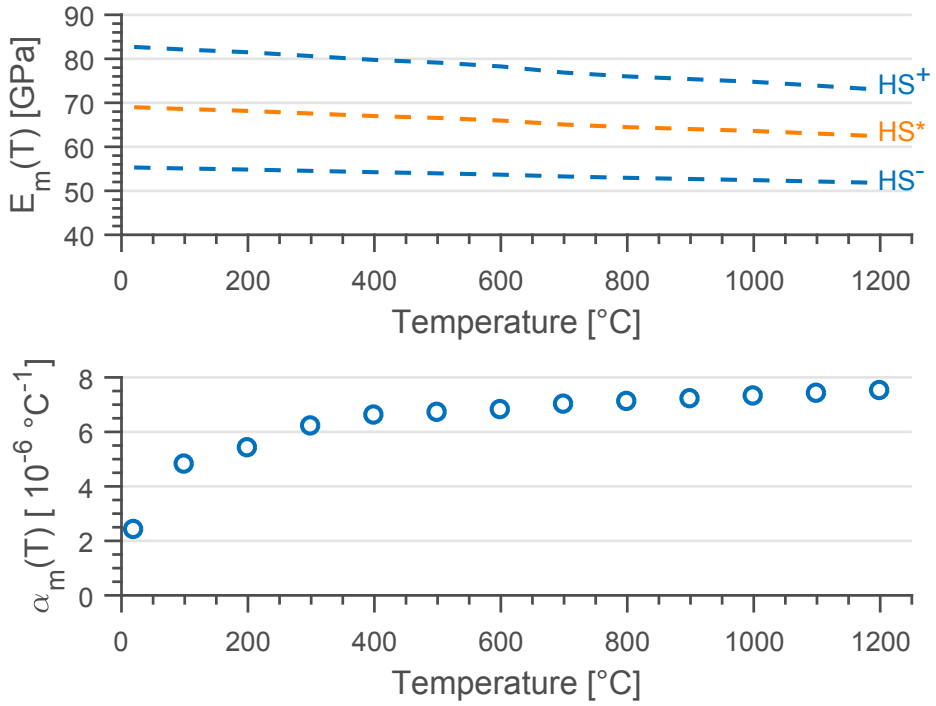

Figure 3.7: Matrix effective Young's modulus and thermal expansion coefficient calculated by HS and FR models respectively.

For each compression test, the temperature of the entire system was considered to be uniform (steady-state). This is also expected in the case of the real experiment due to the low heating rate and high thermal conductivity of carbon. The mesh refinement was calculated depending on the processing time and the accuracy of the results. Furthermore, 2D triangular elements with linear form function were used [128]. The elements presented curvature control with maximum deviation factor of 0.1 and approximate global size of 0.02 μm.

3.2 Carbon-bonded alumina foam filters: A comparison of processing routes

After having characterized the carbon-bonded alumina bulk samples, questions related to the direct comparison with cellular carbon-bonded alumina arose. Therefore, the present Section aims to characterize the production of carbon-bonded alumina foam filters. A comparison of distinct processing routes was made, as well as the suggestion of a new methodology to analyze the ceramic material distribution within the cellular structure. The assessment was mainly based on X-ray computer tomography measurements, performed at several steps of the filters' production. At the end, a preliminary cold crushing strength investigation was carried out, indicating the most promising processing routes.

3.2.1 Motivation

Various types of ceramic filters such as open porous foams, honeycomb structures or "spaghetti" stacks are commonly used by foundry industries in order to withdraw non-metallic inclusions from the molten metal during casting [129–133]. If retained in the cast parts, these inclusions would act as discontinuities within the metallic matrix. Due to the thermal and mechanical properties mismatch between the inclusions and the base metal, the former usually result in internal cracks, slivers or blisters in final rolled products. Especially in case of macro inclusions, the working life will be severely degraded by fatigue [134–139]. Another important task of ceramic filters is reducing the turbulence of the melt flow. Under laminar flow, the risks of metal re-oxidation and cavity formation are minimized [36].

Recently, carbon-bonded alumina (Al_2O_3-C) filters are gaining significant importance, mainly motivated by their excellent thermal-shock and creep resistance [36], due to high thermal conductivity of carbon (up to 400 W/mK for crystalline graphite basal plane). Moreover, the strength scales with the temperature up to 2500 °C for graphite, and the attained plastic deformation can close some cracks and defects [140, 141]. Improvements on filtering efficiency were reported for Al_2O_3-C foam filters associated with special coatings [37, 50, 142].

In general, carbon-bonded alumina filters are produced via the replica technique [41]. This method basically uses a polymeric foam as a template, which is coated by slurry impregnation. After coating the foam, the interstage filter is thermally treated to burn out the polymer and sinter the ceramic material, resulting in a ceramic filter with a replicated geometry of the original polymeric foam. The ceramic coating is a crucial step for the final mechanical properties of the filter, as a homogeneously distributed material is required.

The common technology for producing Al_2O_3-C filters comprises two coating steps [36, 37, 143]. The first one is based on a dip coating (or impregnation) of the polyurethane (PU) open-cell sponge and subsequent squeezing and rolling stages to empty the cells, reducing the excess of slurry and homogenizing the material distribution. Afterwards, a drying stage is required before the spray coating can be carried out. Finally, the coated foams are fired up to 800 °C in a reducing atmosphere. More details about this technology were given by Schmidt *et al.* [143].

Voigt *et al.* [144] investigated geometrical features and mechanical properties of plain alumina filters coated by two distinct techniques: spraying and centrifugation. They concluded that the coating procedure has a large influence on the filter homogeneity, directly affecting its compression strength. Low-viscosity slurries are preferred for centrifugion, whereas slurries with a higher solid content lead to better results when spraying.

No reports were found in the literature related to Al_2O_3-C filters produced by centrifugation. Therefore, the present Section aims to geometrically characterize the filters produced by this technique. Al_2O_3-C filters produced by rolling and spraying (as state of the art) were used as reference.

3.2.2 Materials

As already mentioned in the Motivation (Section 3.2.1), two distinct techniques were used to produce the ceramic filters: *(i)* Rolling and Spraying (*RS*) and *(ii)* Centrifugation (*CF*). Both methods are based on the replica procedure [41]. The *RS* technique was widely explored and described in the literature for Al_2O_3-C filters production [36, 37, 143], whilst *CF* was applied

for plain Al_2O_3-C filters [144, 145]. In the present study, the filters produced by *RS* followed the procedure by Schmidt *et al.* [143] (Figure 3.8a).

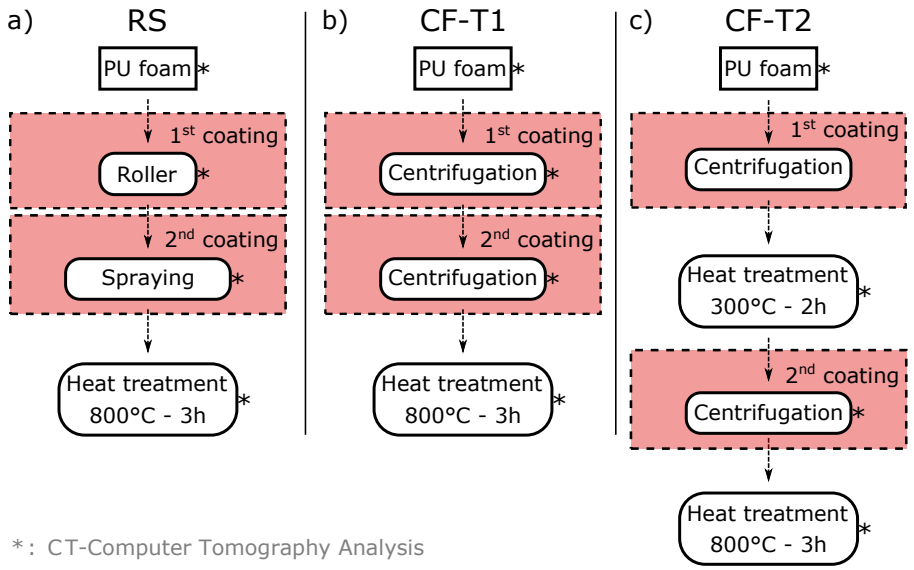

Figure 3.8: Three distinct strategies for sample production.

The raw materials for the filters production were chosen based on the work by Emmel and Aneziris [36]. As alumina source, Martoxid MR 70, 99.8% Al_2O_3 (Martinswerk, Germany) with $d_{90} < 3.0\,\mu m$ was selected. The carbon sources consisted of Carbores® P (Ruetgers, Germany) with $d_{90} < 0.2\,mm$; graphite (Graphit Kropfmuehl, Germany) with $d_{90} < 30\,\mu m$ and carbon black (Lehmann & Voss, Germany) with a primary particle size of 200–500 nm. The additives were ligninsulfonate (Otto-Dille, Germany) as wetting agent and temporary binder, Castament VP 95 L (BASF, Germany) as dispersing agent and Contraspum K1012 (Zschimmer & Schwarz, Germany) as antifoam additive (Table 3.2). Polyurethane foams (Eurofoam, Germany) with 10 pores per inch (ppi) were used as structural template.

While the spraying procedure is a way to deposit material, the centrifugation and roller steps removes the excess of it. The first *CF* coating consists in dipping the polymeric foam into the slurry (81.6 wt.% solid content) (Table 3.2), hand squeezing and placing it in the centrifuging cage. The centrifugation step eliminates the excess of slurry from the foam, emptying the cells. The second *CF* coating is similar to the first one, except that a thinner slurry (65 wt.% solid content) was used and no squeeze was applied. Since the sponge was already coated, squeezing would damage the ceramic structure.

For centrifuging the specimens, the equipment RZR2102 Control (Heidolph, Germany) (Figure 3.9) was used. For each coating, the filters were centrifuged for 20 s at a rotational speed of 850 rpm. A 24-hours interval was taken between the first and the second coating for drying the slurry at room temperature (Figures 3.8b and 3.8c).

One of the drawbacks associated with using the replica method for producing ceramic filters is the inherent presence of hollow struts due to the polymer burnout [36, 146]. This feature directly affects the final mechanical properties of the filters, such as cold crushing strength and friability [147, 148]. Intending to reduce this disadvantage, a variation of the *CF* procedure

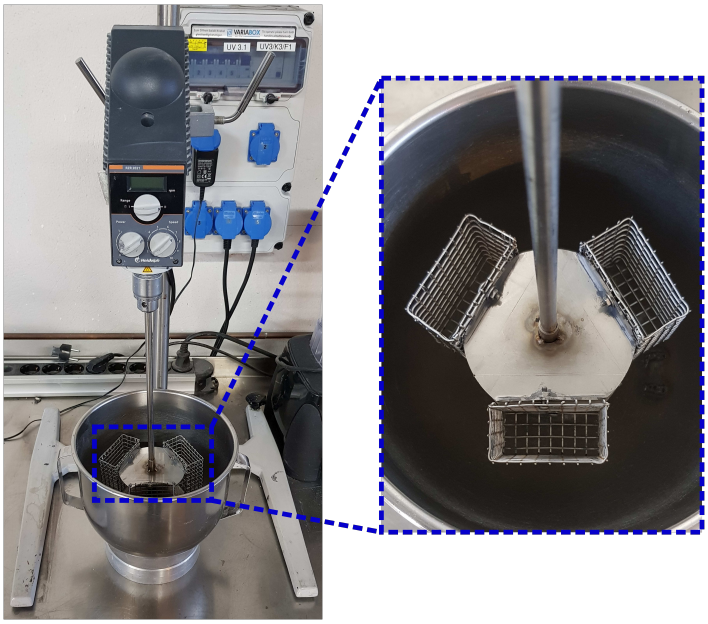

Figure 3.9: Centrifugation device.

Raw materials	wt. [%]
Al_2O_3 Martoxid MR 70	66.0
Carbores® P	20.0
Graphite AF 96/97	7.7
Carbon black MT N-991	6.3
Additives[a]	
Lignin sulfonate C12C	1.5
Castament VP 95 L	0.3
Constraspum K 1012	0.1
Total Solid content[b]	
1st coating (Rolling)	81.6
2nd coating (Spraying)	70.0
1st coating (Centrifugation)	81.6
2nd coating (Centrifugation)	65.0

[a] related to the sum of raw materials; [b] without additives

Table 3.2: Composition of the used slurries

was introduced (Samples *CF-T2*: Figure 3.8c). In this case the samples were thermally treated twice. The first cycle was carried out right after the first centrifugation coating. *CF-T2* samples

were heated up to 300 °C in air with 2 h dwell time at this temperature. The heating rate was 1 K/min. The purpose of this thermal treatment was to partially burn out the PU foam. As Carbores® P softens at 235 °C [149], it was expected that the cracks generated during the PU release could be healed. Therefore, the second coating would partly fill the hollow struts, increasing the filter rigidity.

After the second coating, the samples were thermally treated inside retorts filled with calcined petrol coke up to 800 °C to avoid oxidation. The heating rate was 1 K/ min with 30 min dwell time every 100 K and a final 3 h dwell time at 800 °C. The same thermal treatment was applied for the *RS* and *CF-T1* samples (Figures 3.8a and 3.8b, respectively).

3.2.3 Experimental

X-ray computer tomography (µCT) analysis

To evaluate the homogeneity and wall thickness distributions, one filter from each processing route (*RS*, *CF-T1* and *CF-T2*) was analyzed at different steps of its production (Figure 3.8), using a micro focus X-ray computer tomograph CT-ALPHA (ProCon X-ray, Germany)[‡]. The computer tomograph (CT) device was equipped with a 160 kV X-ray source and Dexela detector (type 1512) with 1944 × 1526 active pixels. The voxel resolution after reconstruction was $40 \times 40 \times 40\,\mu m^3$ for the PU foam analysis and $79 \times 79 \times 79\,\mu m^3$ for the coated filters analyses. A higher resolution was required for the PU foam as its struts thicknesses were considerably thinner than the coated filters ones. The reconstructed CT data were post-processed with the aid of the software *Modular Algorithms for Volume Images* (MAVI, Fraunhofer, Germany) [150]. Additional information about the CT parameters can be found in the Appendix A.4 (Page 143).

The strategy adopted to analyze the wall thickness distribution was based on morphological image processing. Firstly, a binarisation step divided the 3D image voxels into two groups based on their gray level according to Otsu's method [151]: 1) foreground (white) – associated to the material and 2) background (black) – related to the pores. The image operations "erosion" and "dilation" were applied, following Maire *et al.* [152] procedure. It is basically a sieve pattern analysis, where two sequenced operations (erosion and dilation) are applied in the binarised 3D images. Based on that, the wall thickness distribution is calculated, taking into account the difference between the number of white voxels before and after the operations. These sequenced operations are also called *opening* by the MAVI software. More details about this procedure can be found elsewhere [28, 34, 152, 153].[§]

The porosity calculation was made taking into account the ratio between the number of black and total voxels in the region of interest (ROI). This procedure was carried out after the binarization and cropping steps, to avoid border effects.

For analyzing the homogeneity of the material distribution in the filters, six distinct ROIs were analyzed and compared. The ROI designation is related to its location (*WS* - whole sample, *LB* - left bottom, *LT* - left top, *CC* - center, *RB* - right bottom, *RT* - right top – Figure 3.10). All ROIs presented 200 × 200 × 200 voxels, except for the *WS* one. The samples

[‡]It must be highlighted that the CT measurement was conducted by Dr.-Ing. Jana Hubálková from the Institute of Ceramic, Glass and Construction Materials of the TU Bergakademie Freiberg. The experimental design and the results analyses were performed by the author of the thesis

[§]An example of erosion-dilation applied to a 2D cross-section is presented in the Appendix A.5 (Page 145).

were analyzed at several steps during the filter production (Figure 3.8). The CT analyses focused on the following features: *(i)* the homogeneity of the wall thickness distribution, *(ii)* coating thickness at each step, *(iii)* total porosity and *(iv)* shrinkage due to firing.

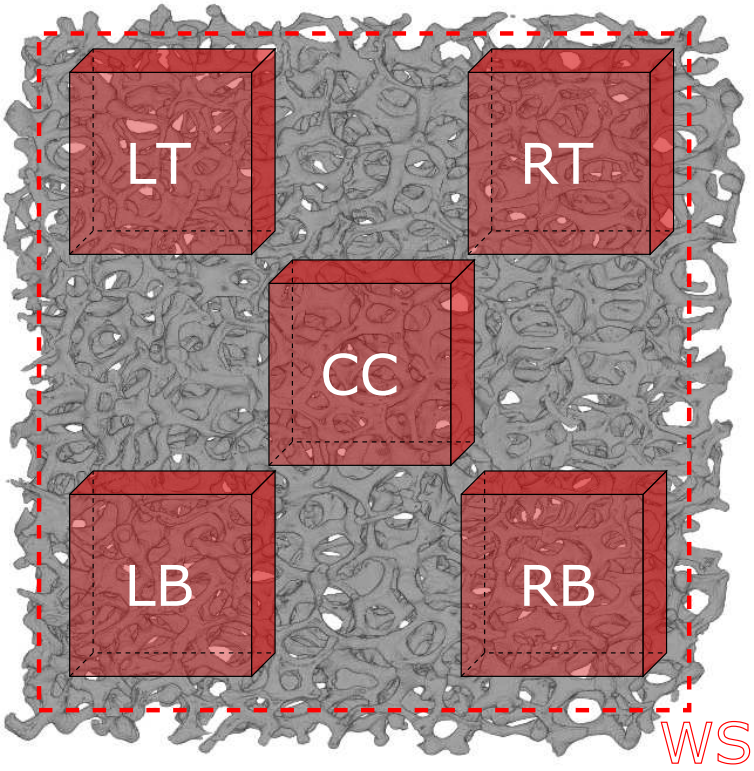

Figure 3.10: Regions of interest analyzed by computer tomography. The ROIs: LB, LT, CC, RB and RT present $200 \times 200 \times 200$ voxels, each.

Optical microscopy analysis

After firing, the samples surfaces were analyzed using a digital optical microscope (VHX-200 D Keyence, Japan). Features such as the presence of pores, micro- and macro-cracks on the surface were investigated, providing the qualitative classification of the filters surfaces from rough to smooth.

Cold crushing strength evaluation

As preliminary tests, one sample from each processing route was mechanically characterized by cold crushing test. The experiments were carried out using an universal testing machine Tira test 28100 (TIRA GmbH, Germany) equipped with a 5 kN load cell. The machine was controlled by displacement with a fixed crosshead speed of 1 mm/min. In order to better distribute the load on the filters, cardboard pads (thickness of 0.26 mm) were placed between the filter and the punches.

3.3 Carbon-bonded alumina foam filters: The challenge of up-scaling

After characterizing the ceramic material distribution of carbon-bonded alumina filters produced by distinct processing routes (see Section 4.2.1), some new questions arose:

- Are the results found for the centrifugation procedure exclusively related to the processing route, or using a 2nd coating slurry with lower solid content than the spraying one also influenced it?
- Are the trends also valid for filters with larger dimensions? Answering this question would be very important to validate the concept of using carbon-bonded alumina foam filters in the continuous casting technology, as suggested by Wetzig *et al.* [28] (discussed in Section 2.2.1).
- How to automate and extract more information from the µCT analysis?
- Which physical features can be correlated to the wall thickness distribution parameters (μ and σ)?
- What is the influence of processing – sample size on the material distribution?

To answer those and other questions, the present Section is proposed. The two best procedures from the previous Section (3.2) (*RS* and *CF-T1*) were chosen for a deeper assessment (from this point, the processing route *CF-T1* will be simply called *CF*).

This Section intends to focus on further characterizing carbon-bonded alumina foam filters, inspired by the methodology developed in the previous one (Section 3.2) and also to address new topics, such as the influence of the cell morphology on the filters' mechanical behavior.

As a complement to the geometrical and mechanical characterization of the filters, artificially generated foam models were also developed. Therefore, in a more controlled environment, a higher variability of foams' morphology could be studied. One could correlate this approach to the model materials approach explained in Section 3.1.4, where simplified model materials are used to explain the complex behavior of industrial ones.

3.3.1 Motivation

As discussed by Luchini *et al.* [154], an ideal ceramic filter for metal melt filtration should present all of the following features (listed in no particular order):

- Suitable refractoriness (according to the metal being processed);
- Good creep and thermal-shock resistance;
- Sufficient mechanical strength at room and in-service temperature;
- Good erosion resistance;
- High functional porosity;

- Low specific heat capacity;
- Good corrosion resistance;
- Poor molten metal wetting;
- High chemical affinity with the inclusions to be removed;
- Homogeneous distribution of impregnated material (see below);
- Cost-efficient production method.

As already presented, the majority of materials applied in the molten metal filtration consists of open-cell ceramic foams produced via the replica process [41]. These filters have a higher specific surface area and lower flow resistance than multi-hole filters, favorably influencing the micromechanisms of filtration [129, 155]. Moreover, the metal flow is adjusted from turbulent to laminar, reducing the risk of reoxidation and the formation of cavities. As a result, a better surface quality and faster mold filling are achieved [156].

A major disadvantage of the replica process is the formation of hollow struts which remain after the burnout of the polymer templates [36, 146, 157]. In order to improve the properties of replica ceramic foams, Vogt *et al.* [146] applied a vacuum infiltration process to fill the cavities inside the struts. The authors observed a 100 % increase in compressive strength (388 % when using zirconia-toughened alumina) of the samples, associated to a weight gain of only 10 %. Similarly, Salvini *et al.* [157] infiltrated ceramic filters with colloidal suspensions (alumina and silica) and analyzed the changes in strength and permeability of the samples among other parameters. They showed that this new procedure positively affects the filters' strength without impairing the permeability. However, in terms of industrial production, this processing route would be more costly and time-consuming than the traditional method due to the additional step.

D'Angelo *et al.* [158] analyzed reticulated ceramics under compression via the finite elements method. They characterized Si–SiC foams produced by the replica technique and investigated how the morphological features affect their mechanical properties. The authors also defined a stress concentration parameter as function of the applied stress and used it to compare distinct cell morphologies. They concluded, for the filters analyzed, that during compression the most stressed region would be located at the strut's nodes, therefore, being potential sources of failure initiation.

Werzner *et al.* [159] analyzed the mechanisms of inclusion removal from molten aluminum by open porous filters in a parametric study. They pointed out that the filtration efficiency (η) is directly proportional to the inclusions' dimensions. The authors calculated a $\eta = 90\,\%$ for inclusions with diameter in the range of 100 µm, which dropped to $\approx 10\,\%$ for those with diameter close to 1 µm (for fixed filter dimensions and porosity). In order to improve the filtration of small inclusions, they suggested to considerably increase the filter thickness. However, simply incrementing this parameter without adjusting the porosity would result in a higher pressure drop through the filter. This would in turn enhance the likelihood of metal freezing during application.

In a more recent study, Werzner *et al.* [160] analyzed the influence of the foam morphology on the effective properties related to metal melt filtration. They numerically investigated

artificially-generated and real filter geometries with different porosity and strut tapering (related to the material distribution between the struts and the joints). It was concluded that for a given porosity, the filtration efficiency is favored as the filter material distribution is shifted from the joints to the struts middle part, increasing the filter surface area. They also investigated the *dilemma* concerning the porosity and pressure drop. It was shown that at constant melt velocity, the filtration efficiency increases as the porosity decreases, mainly due to the greater direct interception. However, decreasing the porosity, the pressure gradient increases at an even higher rate. Therefore, highly porous foams are preferred in terms of filtration efficiency per unit of pressure gradient. As mentioned, one drawback of highly porous foam filters is related to their mechanical properties, mainly crushing strength.

Based on the literature, a consistent industrial strategy to reduce the non-metallic inclusions content in steel cast products relies on the use of highly porous ceramic filters. Therefore, the aim of the present Section is to compare the structural and mechanical properties of highly porous samples (with relative density lower than 15 %) produced via different routes, namely impregnation and rolling followed by cold spraying (RS) or double centrifugation (CF). In addition, rectangular prismatic polyurethane foam templates of different sizes were used to investigate the challenges related to the up-scaling of both techniques. To the author's knowledge, the majority of ceramic foam filters for molten metal filtration is traditionally produced by impregnation, rolling and spraying, however, other production methods may result in better properties and reliability [161, 162].

3.3.2 Materials

The Al_2O_3-C slurry used for the templates impregnation followed the recipe proposed by Emmel and Aneziris [36]. The raw materials were aluminum oxide (Martoxid MR70, Martinswerk, Germany, 99.80 wt.% Al_2O_3, $d_{90} < 3.0$ µm), modified coal tar pitch powder (Carbores® P, Rütgers, Germany, $d_{90} < 0.2$ mm – used as a binder as well as a carbon source), fine natural graphite (AF 96/97, Graphit Kropfmühl, Germany, 96.7 wt.% carbon, $d_{90} < 30$ µm) and carbon black powder (Luvomaxx N-991, Lehmann & Voss & Co., Germany, carbon content $\geq$ 99.0 wt.%, ash content > 0.01 wt.%, primary particle size of 200–500 nm). The additives were ammonium ligninsulfonate (C12C, Otto-Dille, Germany – used as wetting agent and temporary binder), modified polycarboxylate ether (Castament VP95L, BASF, Germany – used as a dispersant) and alkyl polyalkyleneglycol ether (Contraspum K1012, Zschimmer & Schwarz, Germany – used as an antifoam additive). The formulation of the slurries is given in Table 3.3.

Sample preparation

The carbon-bonded filters were produced by the modified replication technique based on the Schwartzwalder and Somers process [41]. Polyurethane foams (Eurofoam, Germany) with 10 pores per inch (ppi) were used as structural template. In order to investigate the up-scaling effect of the coating processes on the mechanical and structural features of the filters, two different foam template sizes (factor A) with the following dimensions were chosen (Figure 3.11):

1. $50\times50\times22\,\mathrm{mm}^3$ (S)
2. $100\times100\times44\,\mathrm{mm}^3$ (L)

Raw materials	wt. [%]
Al_2O_3 Martoxid MR 70	66.0
Carbores® P	20.0
Graphite AF 96/97	7.7
Carbon black MT N-991	6.3
Additives[a]	
Ammonium lignin sulfonate C12C	1.5
Castament VP 95 L	0.3
Constraspum K 1012	0.1
Total Solid content[b]	
1st coating	81.6
2nd coating	70.0

[a] related to the sum of raw materials; [b] without additives

Table 3.3: Composition of the used slurries

The carbon-bonded filters were produced by the following two-step coating approaches (factor B):

1. impregnation and rolling followed by cold spray coating, according to Emmel and Aneziris [36] (RS);
2. impregnation and centrifugation followed by a second impregnation and centrifugation, according to Luchini et al. [34] (CF).

Differently from Section 3.2.2 (Page 35), where a thinner slurry was used for the 2nd coating centrifugation slurry, slurries contaning 81.6 wt. % and 70.0 wt. % solids content were used for the 1st and 2nd *RS* and *CF* coating steps, respectively. Centrifugation of the foam samples after immersion in the slurry was carried out by means of a rotor with special housings connected to a mechanical stirrer. The rotational speed was set at 960 rpm, based on preliminary tests. The spinning time was 10 s and 5 s for the first and second step, respectively. More detailed information about the centrifugation procedure can be found in [34].

After drying at room temperature, all filters were heat-treated in steel retorts filled with calcined petcoke (Müco, Germany) with particle size between 0.2 and 2 mm, in order to attain reducing conditions. The maximum temperature of 800 °C was reached with a heating rate of 0.8 K/min and a final dwell time of 180 min at 800 °C.

3.3.3 Experimental

X-ray computer tomography (µCT) analysis

To evaluate the homogeneity and wall thickness distributions, one filter from each processing route and sample size was analyzed using a microfocus X-ray computer tomograph CT-ALPHA

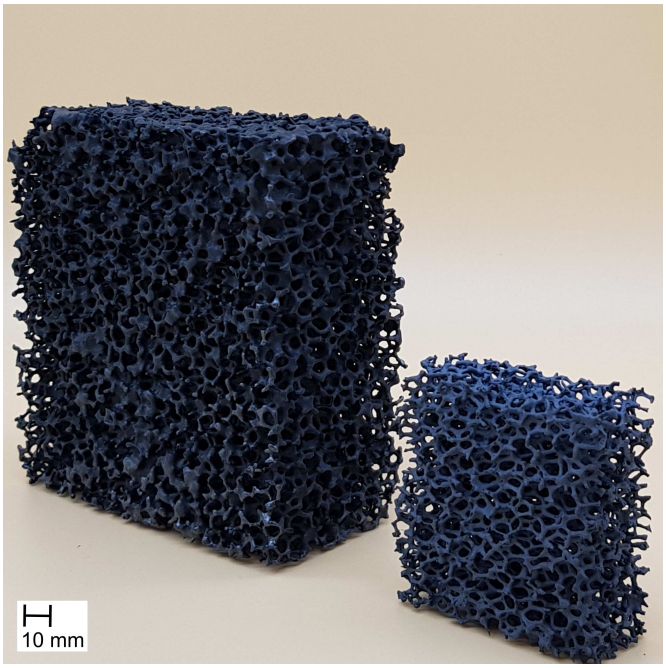

Figure 3.11: Filters L and S investigated in this study.

(ProCon X-ray, Germany). The filters were chosen based on their weight, i.e. closest value to the average weight of each *manufacturing process–sample size* combination. The CT device was the same presented in Section 3.2.3. The voxel size was $79 \times 79 \times 79\,\mu m^3$ after reconstruction.

The reconstructed CT images were post-processed using the software Modular Algorithms for Volume Images (MAVI, Fraunhofer, Germany). The procedure for the CT analyisis was the same as presented in Section 3.2.3. Firstly, the binarization step of the 3D images was carried out according to Otsu's method [151]. The morphological strategy to analyze the wall thickness distribution is called *opening* and was based on the procedure described by Maire et al. [152]. The same approach was used in previous investigations [28, 34, 153].

Following the strategy proposed on Section 3.2.3, the filter samples were analyzed based on regions of interest (ROIs). In total, 108 ROIs were evaluated for S filters and 180 for the L ones. All ROIs presented $100\times100\times100$ voxels and were homogenously distributed in the filter's geometry. In the case of S filters, the ROIs were positioned in three distinct planes, whereas, for the L, the amount of planes was 5 (36 ROIs per plane for both sample dimensions).

To analyze the results, a MATLAB code was developed. This algorithm characterized each ROI (wall thickness distribution type, mean and standard deviation, as well as the local porosity) and its positioning, based on the results of Section 4.2.1. Afterwards, a geometrical linear interpolation step was applied to infer the aforementioned features at the positions outside the ROIs [28], assuming the results from the previous step being located at the barycenter of each ROI. Finally, four planes were selected to illustrate the results (Figure 3.12).

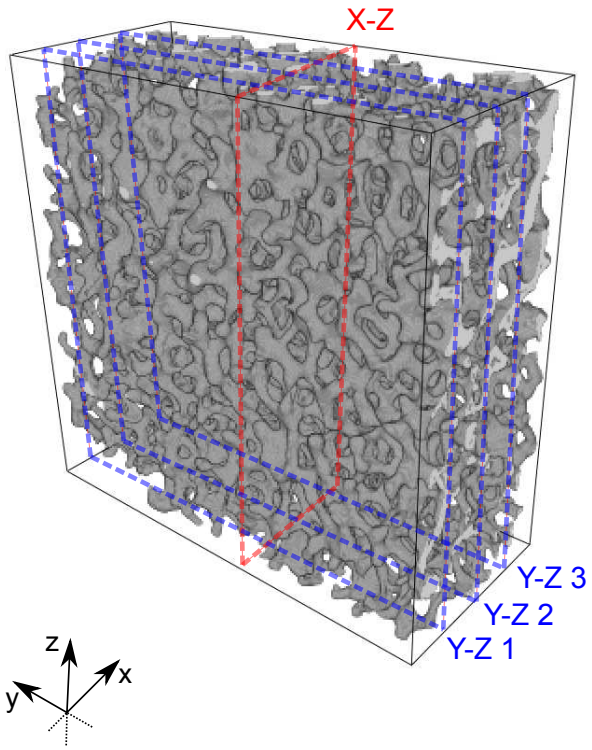

Figure 3.12: Volume rendered image of a filter analyzed via µCT. The planes X-Z, Y-Z 1, Y-Z 2 and Y-Z 3 were chosen to deeper investigate the filters homogeneity.

Optical microscopy analysis

For the investigation of the filters after thermal treatment, a digital light microscope (VHX-200 D, Keyence, Japan) was used.

Mechanical characterization

In total, 45 samples from each *manufacturing process–sample size* combination (RS–S, RS–L, CF–S and CF–L) were tested using the universal testing machines TIRAtest 28100 and TIRAtest 2850 (TIRA GmbH, Schalkau, Germany) equipped with a 5 kN and 20 kN load cells, respectively. The procedure was controlled by displacement with a constant crosshead speed of 1 mm/min. In order to improve the load distribution on the uneven filter body surface, cardboard pads with a thickness of 0.26 mm were placed between the sample and the punches of the testing machine.

For the analysis of the results, 30 filters of each *manufacturing process – sample size* combination were chosen. The criterion for this selection was based on the maximum force achieved for each specimen during the crushing test. Therefore, the results of the 30 specimens with maximum force closer to their group average were selected. In that way, outliers were excluded.

In order to analyze the cold crushing strength (CCS) results, some data treatment had to be

carried out. The typical CCS variables are force and displacement[¶] (the compressive stress and strain can be calculated from them). Basically, for bulk samples, the force is divided by the sample's initial cross-section area resulting in the engineering stress, and the displacement is divided by the sample's initial thickness resulting in the engineering strain. However, for highly porous structures this procedure is not straightforward. On one hand, it is quite complicated to determine the true cross-sectional area of the filters, as they present a network of struts with non-homogeneous distribution. Conversely, using some complex method to assess each filter's true geometry (computer tomography, for example) would result in costly and time consuming evaluations, as ceramic products generally require a high number of samples for estimating representative properties.

Therefore, some oriented simplifications were introduced to provide the comparison of the filter geometry and manufacturing processes. Equation 3.10 was used to represent the cold crushing strength value (σ^*). σ^* was calculated by dividing the maximum breaking force (F_{max}) reached during the crushing test by the theoretical cross-sectional area of the filter A_{theor}, without taking the macro porosity into account. A_{theor} was $50 \times 50\,\mathrm{mm}^2$ for small (S) filters and $100 \times 100\,\mathrm{mm}^2$ for large (L) ones.

$$\sigma^* = \frac{F_{max}}{A_{theor}} \tag{3.10}$$

Calculating just σ^* was not sufficient for a proper comparison between the different filter geometries, as each sample presented a different mean strut diameter. Therefore, the relative density ρ^*/ρ_s was used as a variable (equation 3.11). The relative density was calculated from the samples' mass (m_{filter}) and theoretical volume (V_{theor}), and the true density of the filter material (ρ_s), obtained by helium pycnometry ($\rho_s = 2.9669\,\mathrm{g/cm}^3$).

$$\frac{\rho^*}{\rho_s} = \frac{m_{filter}}{V_{theor}} \cdot \frac{1}{\rho_s} \tag{3.11}$$

In order to evaluate the σ^* results and compare the filters manufacturing processes and samples size, a balanced two-way analysis of variances (ANOVA) was carried out using the software R [163]. For this, a merit index (I^*) was used. I^* was based on the Gibson–Ashby [26] model for bending-dominated cellular ceramics subjected to compression (equation 3.12) (see Section 2.2.2), where σ_s is the strength of an individual strut and c is a constant feature of the cellular geometry. Therefore, as $\sigma^* \propto \left(\frac{\rho^*}{\rho_s}\right)^{\frac{3}{2}}$, I^* was defined as $I^* = \sigma^* / \left(\rho^*/\rho_s\right)^{\frac{3}{2}}$.

$$\frac{\sigma^*}{\sigma_s} = c \cdot \left(\frac{\rho^*}{\rho_s}\right)^{\frac{3}{2}} \tag{3.12}$$

3.3.4 Numerical Simulation

Numerical simulation was used as a tool to enhance the understanding of the experimental results from the mechanical tests and µCT analysis. Artificial foam geometries were modelled based on the methodology proposed by Abendroth *et al.* [53]. They consisted of 216 cells with hollow struts. The geometric modelling process started with the development of an appropriate

[¶]Those were the variables analyzed in Section 3.2.3 (Page 39), since it was a preliminary assessment.

periodic sphere packing. Thus, a Laguerre tessellation was generated and optimized by minimizing the distance between the sphere centers and the corresponding cell barycenters. The resultant geometry was subsequently modified using the the Ken Brakke's Surface Evolver [164] by minimizing the foam surface energy per unit of volume.‖

The next step consisted of mapping the triple edges of the foam from Surface Evolver into a 3D voxel grid. A 3D Gaussian filter was applied on the resulting strut density field and a smoothed 3D representation of the foam was obtained. The final geometry is a function of the relative density of the foam (ρ^*/ρ_s) and of the strut shape (tapering) factor (k), which controls the material distribution between the joints and the struts. Thereby, a high k value denotes high material concentration in the joints and consequently remarkably tapered struts and $k = 0.5$ denotes no tapered struts (real cylinders). More information can be found at Abendroth *et al.* [53].

28 different geometries were generated in total. Of those, 20 foams were modelled intending to represent the real filters that were mechanically tested in this study. They result from the combination of 4 relative densities (0.09; 0.10; 0.11 and 0.12) with 5 strut shape factors k (0.7; 0.8; 0.9; 1.0 and 1.1). The strut shape factor k was varied from 0.7 to 1.1 as an attempt to cover the real tapering of the filters, since when $k = 0.5$ there is no tapering and by visually analyzing the real foams it was possible to identify certain tapering level. The 8 remaining geometries were designed to study the influence of k for a higher ρ^*/ρ_s value, as well as a wider ρ^*/ρ_s range. Figure 3.13. shows the result of 4 different k factors for a fixed ρ^*/ρ_s. Fig. 3.14 emphasizes the material concentration on the joints as function of k value. It is clear that with increasing k the filter material is shifted towards the joints, resulting in tapered struts.

In order to compare the modelled geometries with the real filters analyzed by computer tomography, the same strategy presented in the CT section, *opening* was used. Based on this strategy, a better correlation of the foam geometrical parameters (k factor and ρ^*/ρ_s, for instance) with the CT wall thickness distribution variables (μ and σ) was achieved, providing a better interpretation of the CT results for real filters. Therefore, the artificially–generated foams were morphologically analyzed with the MAVI software, being the whole sample considered as a single ROI.

As complement to the morphological analysis of the artificially-generated foam samples, finite element simulations were also carried out using the same artificial geometries. Virtual compression tests were carried out and the influence of the k factor and of ρ^*/ρ_s on the filters' global strength was assessed. The homogenization procedure used a *von Mises* failure criterion, according to the strategy proposed by Storm et al. [50]. Therefore, periodic boundary conditions for displacements were applied using the constraint equations $u_j^{i+} - u_j^{i-} = \Delta u_j^i$, for corresponding points of opposite boundaries $i+$ and $i-$. Reference points for every coordinate axis i are used to set the global stress $\bar{\sigma}_{ij} = 1/2 \cdot [f_j^i/A^i + f_i^j/A^j]$, where f_j^i represents the reaction forces and A^i denotes the theoretical cross section area of the filter. More information about the homogenization is given by Storm et al. [50]. The simulations assumed a linear elastic material behavior (Young's modulus = 20 GPa and Poisson's ratio = 0.25). As the results were normalized with respect to the failure stress, they are valid for any choice of Young's

‖It must be highlighted that the artifical foam geometries were generated by Dr.-Ing. Martin Abendroth from the Institute of Mechanics and Fluiddynamics of the Technische Universität Bergakademie Freiberg. The modelling design and statistical analysis were performed by the author of the thesis.

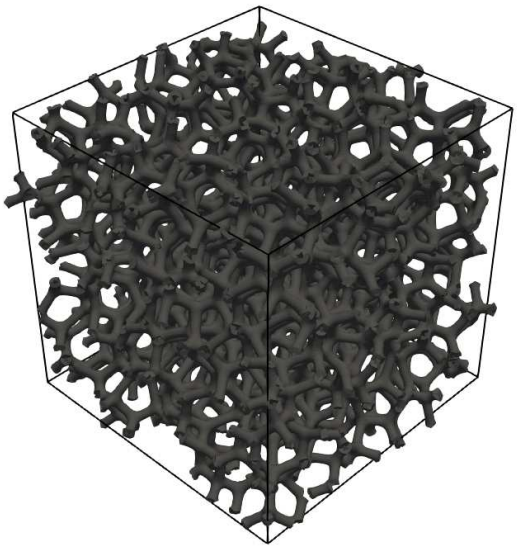

(a) k=0.7 and $\rho^*/\rho_s = 0.11$.

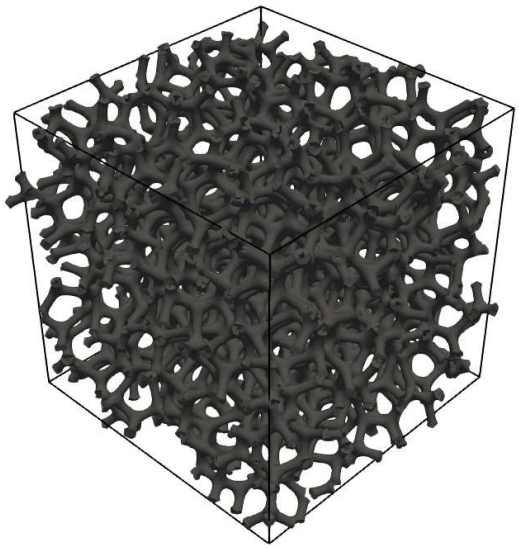

(b) k=0.8 and $\rho^*/\rho_s = 0.11$.

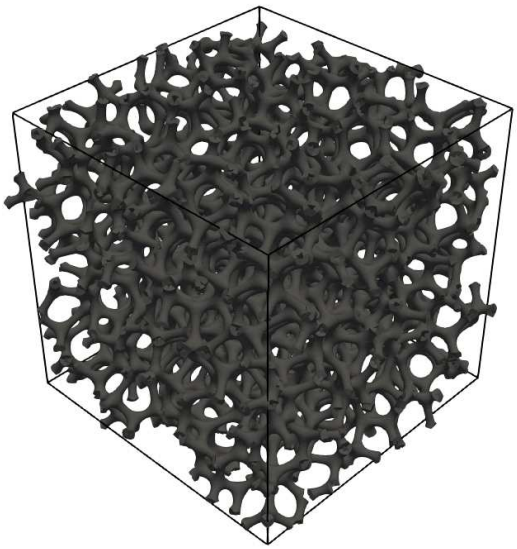

(c) k=0.9 and $\rho^*/\rho_s = 0.11$.

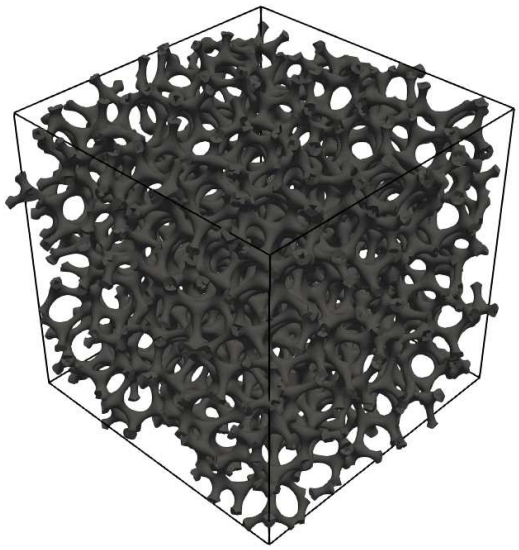

(d) k=1.0 and $\rho^*/\rho_s = 0.11$.

Figure 3.13: Artificially-generated foam geometries.

modulus.**

**It must be highlighted that the finite element simulations were performed in cooperation with Mr. M.Sc. Christoph Settgast from the Institute of Mechanics and Fluiddynamics of the Technische Universität Bergakademie Freiberg. The results analysis and interpretation were conducted by the author of the thesis.

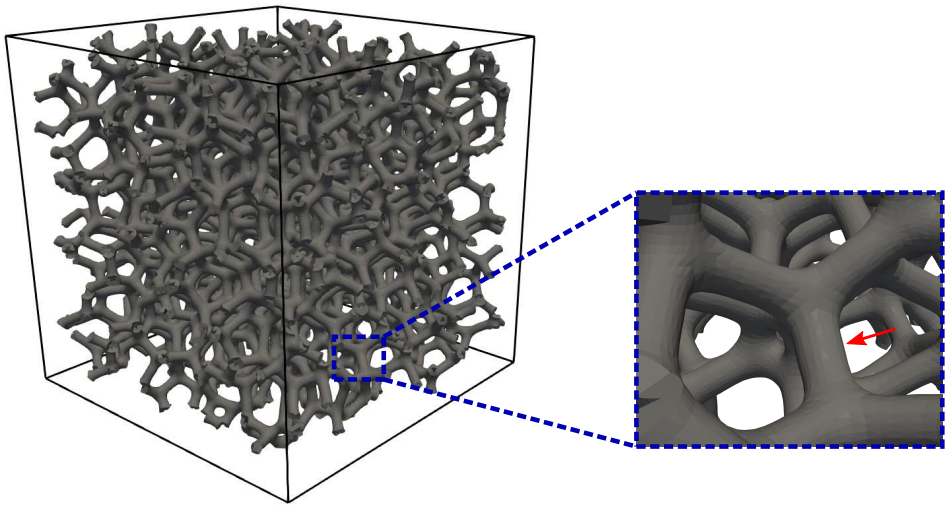

(a) k=0.7 and $\rho^*/\rho_s = 0.11$.

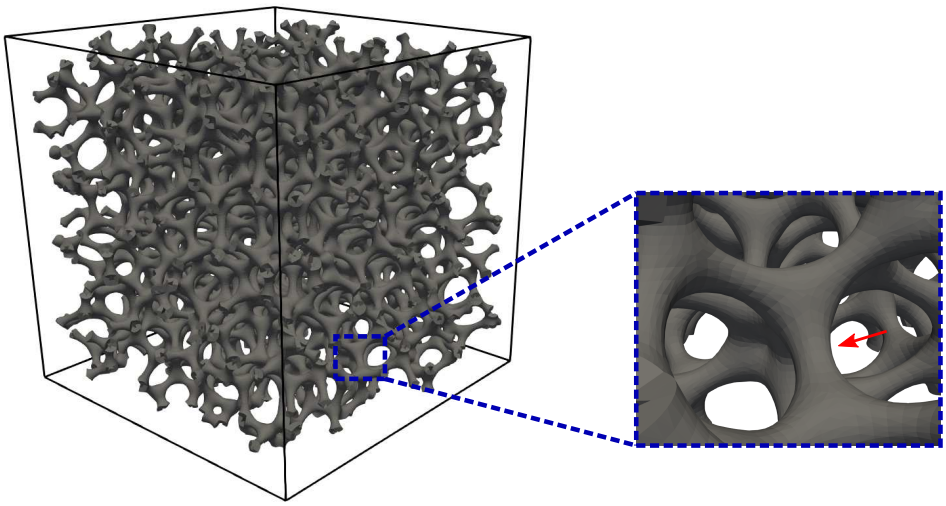

(b) k=1.0 and $\rho^*/\rho_s = 0.11$.

Figure 3.14: Artificially-generated filter geometries with 11% relative density and different k factors. (Zoom on the k influence).

4 Results and Discussion

4.1 Non-linear Young's modulus behavior of carbon-bonded alumina at high temperatures

4.1.1 Young's modulus measurement via impulse excitation technique (IET)

Fig. 4.1 illustrates the effective Young's modulus values as a function of temperature for the two heating and cooling cycles. The results presented are the average of the three samples' measurements. The confidence interval of the measurements varies from 0.26 up to 3.17 GPa.

To support the comprehension of this non-linear behavior, the curve was divided into ten stages which are discussed in detail as follows.

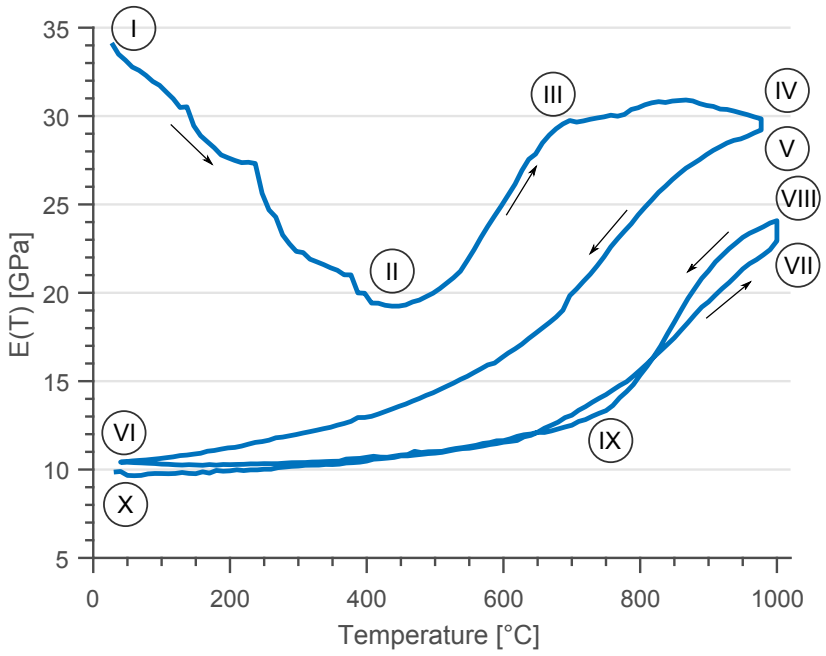

Figure 4.1: Average Young's modulus curve of just cured carbon-bonded alumina during two heating/cooling cycles. The stages I to X are arbitrary divisions.

I–II Decrease of the effective Young's modulus due to the release of the resin volatiles [165, 166] and a consequent increase of the open porosity. The latter increases for the following primary reasons: solid-gas transformation, leaving pores in the structure, and the pressure increase of the volatiles, stressing the material and possibly cracking it. Most

likely, the volatiles release leads the entire behavior of the composite from the room temperature up to 500 °C during the first cycle. This assumption will be verified via the thermogravimetry analysis (Section 4.1.2).

II–III Increase of the effective Young's modulus due to the resin carbonization [167, 168] and closure of a few pores and cracks as a consequence of the thermal expansion mismatch between the matrix, alumina and graphite particles. As alumina and graphite ($\perp$ direction) present higher thermal expansion coefficients than glassy carbon, those particles tend to expand more than the matrix as the temperature increases [103, 104]. Consequently, the open porosity that was previously generated is partially closed.

III–IV During these stages, **the Young's modulus was almost stable**, as an increase of the E value due to the closure of the residual porosity and the densification of the sample during heating up was counterbalanced by its decrease caused by the individual phases' behavior (Figs. 3.5 and 3.6).

IV–V Decrease of the effective Young's modulus, most likely induced by thermal stresses which leads to in-situ cracking. At high temperatures, it is quite possible that the thermal cracks are generated by thermal stresses. At the current stage IV–V, the formed cracks will not be closed due to the particles' thermal expansion as the temperature was kept constant (dwell time).

V–VI The effective Young's modulus decreases during cooling due to a gap-opening between the particles and matrix and the re-opening of a few healed cracks. Gap-opening occurs due to the thermal expansion mismatch among the distinct phases. Very likely, the re-opened cracks are comprised mainly by those developed during the volatiles release at stages I–II. It is assumed that between the current steps (V–VI), cracks might coalesce and branch out. This assumption is supported by the profile of the following heating steps (VI–VII), which does not follow the previous cooling path (V–VI). Liu et al. [122] identified typical network-cracks in graphite materials with high carbon content, which were induced by the highly anisotropic thermal expansion of graphite [122, 169, 170]. In a following section (Section 4.1.4), scanning electron microscopy will be used to attest if the network-cracking detected in previous studies also occurred in the present one.

VI–VII The effective Young's modulus increases exponentially during the second heating cycle. At lower temperatures, firstly, small cracks and gaps are closed due to the thermal expansion mismatch among the particles and the matrix. With increasing temperature, larger sized cracks and gaps are also progressively closed.

VII–VIII The increase of the Young's modulus during the second dwell time at 1000 °C was possibly motivated by a viscoplastic behavior of the carbon matrix [122,141,171,172]. As the thermal expansion coefficient of the alumina is higher than that of the matrix, compressive stresses are generated at the alumina-matrix interface (thermal stresses). Solarek et al. [141,171,172] and Liu et al. [122] demonstrated that, at high temperatures, creep effects start to affect the behavior of carbon-bonded materials. Therefore, due to local creep, the matrix deforms more easily, allowing the alumina and graphite to expand further. Consequently, the contact surface of the particle-matrix would rise and

the sample's effective Young's modulus would increase, as it has been observed. The distinct behaviors between the IV–V and the VII–VIII dwell times can be justified by the thermal-load history of the material. As the material had never experienced 1000 °C before the IV–V stage, the thermal stresses generated at this temperature resulted in cracks around the particles. On the other hand, the microstructure at VII–VIII was already influenced by the thermal treatment (the samples were already micro-cracked). Therefore, the thermal stresses at this temperature were considerably lower than the ones at IV–V. Thus, the viscoplastic phenomena ruled the material's effective behavior.

VIII–IX Decrease of the effective Young's modulus during cooling, caused by the thermal expansion mismatch between phases (re-opening of gaps). The sharp decrease of the Young's modulus at this stage is due to the higher system densification than that at the first heating cycle. For dense materials, crack initiation tends to generate higher damage.

IX–X Slight decrease of the Young's modulus during cooling. It is assumed that at IX most of the large particles are already detached from the matrix. The decrease originates mostly from the enlargement of the gaps' sizes, being less dependent on new gaps creation. The Young's modulus at stage X is lower than at VI due to the viscoplastic behavior observed between the stages VII–VIII and higher damage for VIII–IX. Therefore, the microstructure at stage X diverges from the one at stage VI.

4.1.2 Thermogravimetric analysis (TGA)

To confirm some of the assumptions made during the effective Young's modulus analysis, a TGA was conducted, aiming to identify the crucial temperatures during resin decomposition. As explained earlier, the results presented include the already established difference between the white and the real test. Therefore, all results reported here are related to the carbon-bonded alumina sample, excluding the effect of the petroleum coke.

In Fig. 4.2, the normalized mass change as a function of temperature and its simple derivative ($\frac{\mathrm{d}m}{\mathrm{d}T}$) are presented. One can observe that most of the changes occurs between 300 and 700 °C. The total mass change fraction was approximately -1.8 %. Due to experimental noise in the derivative data (raw curve), a smoothed curve is also displayed. For the smoothing, the moving average technique [173] with three neighbor points was applied. As can be noticed, three distinct peaks were detected. The first one, between 50 and 180 °C is mainly related to water evaporation. As the samples were not kept in a controlled atmosphere after curing, it is very likely that water vapor could have remained in the pores, as stated by Chang and Tackett [166].

The second and third mass loss peaks are in the range of 240 and 740 °C and are related to the thermal decomposition including combustion and pyrolytic conversion of the resin into volatiles and glassy carbon respectively, as explained by Lee [165]. In this temperature interval, mostly ammonia, water, carbon dioxide, methane, toluene, xylene, and phenol are released [166].

In Fig. 4.3, the effective Young's modulus as a function of temperature is re-plotted for the first heating cycle (stages I to IV). Furthermore, the normalized mass change from the TGA was added to the Figure. One can observe that from room temperature up to $\approx$ 500 °C, the decrease of the effective Young's modulus can be justified by the volatiles release, which increases the open porosity.

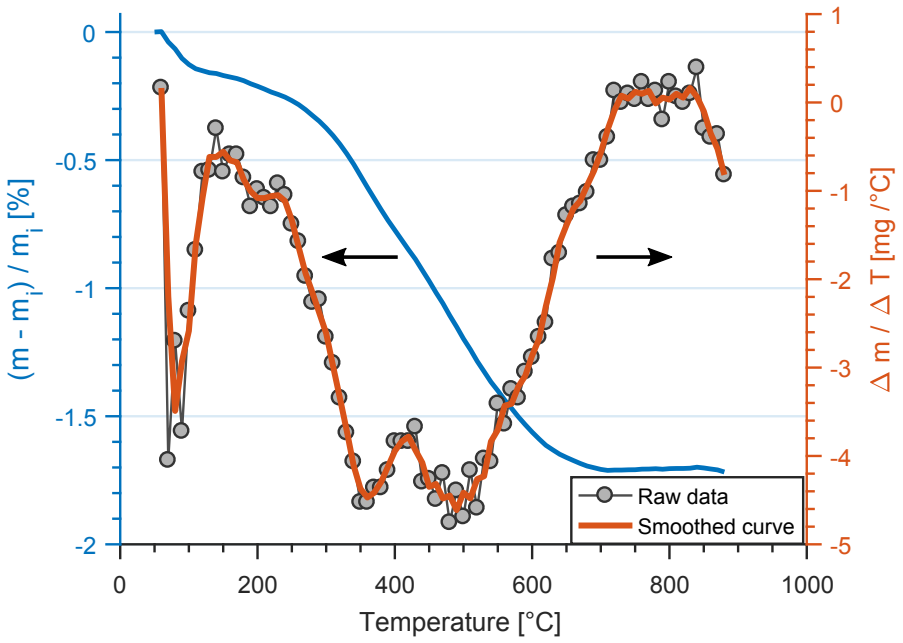

Figure 4.2: Normalized mass (left y-axis) and its simple derivative (right y-axis) of a sample with the composition presented in Table 3.1 after curing at 180 °C as function of temperature - m = mass at specific temperature and m_i = initial mass.

Although the process of volatiles release continues up to ≈ 700 °C, the effective Young's modulus increased in the range between ≈ 500 °C and ≈ 700 °C. For temperatures above ≈ 500 °C, the matrix densification and the thermal expansion mismatch among the phases dominated the process by closing some of the open porosity associated with the volatiles release.

From room temperature up to ≈ 500 °C, the porosity increasing rate is higher than the decreasing one due to the thermal expansion and densification effects. Nevertheless, in the temperature range between 500 and 700 °C, the increasing rate compensates the decreasing one and leads to the global behavior. Consequently, the effective Young's modulus is higher. This result is in agreement with those obtained by Werner *et al.* [104] who analyzed a pyrolized carbon-bonded alumina in air. They demonstrated that the porosity decrease, due to the thermal expansion mismatch, was even higher than the oxidation rate.

4.1.3 Porosity measurements

The apparent porosity of the samples treated at three distinct temperatures is presented in Fig. 4.4. The just cured (JC) sample (180 °C) has the lowest apparent porosity. Heating it up during the first cycle led to the volatiles release (cf. Fig. 4.2) and a higher apparent porosity in the case of the sample that was treated at 500 °C (HT1×). After two cycles (1000 °C) (HT2×), the apparent porosity is the highest. The additional thermal treatment resulted in further volatiles release and network cracks. Moreover, gaps developed between the particles and the matrix. As a consequence, the number of coalescing cracks and the extension of the crack

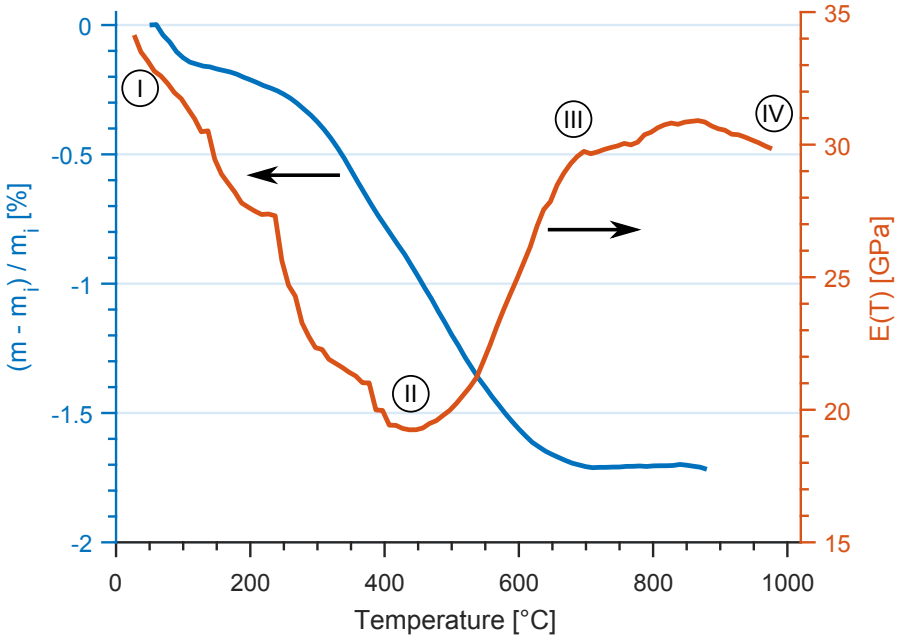

Figure 4.3: Normalized mass (left y-axis) and Young's modulus (right y-axis) variation of a cured carbon-bonded alumina sample as a function of temperature.

network are reduced, along with the ratio of closed to apparent porosity.

It is evident that the measurements of the HT1× showed the highest scattering. As previously explained (Section 4.1.2), the volatiles release continues up to 700 °C. As 500 °C is an intermediate temperature between the cure and the end of the volatiles release, and that the volatiles release is a dynamic process, the ceramic system experiences a properties transition temperature depending on samples' geometry, density, particles size and phase distribution.

4.1.4 Scanning Electron Microscopy (SEM)

Scanning electron microscopy (SEM) was used in order to evaluate the microstructure of carbon bonded alumina. Fig. 4.5 shows the SEM micrographs of the three analyzed samples. It can be observed that the matrix changes with the extent of the thermal treatment. The just cured (JC) sample (Fig. 4.5-a) presents a relatively homogeneous matrix with significantly smaller and more isolated cracks. Fig. 4.5-b presents a few medium-sized network cracks in the matrix, whereas, in Fig. 4.5-c, it is possible to detect a well-developed crack network. As explained in Fig. A.1 (stages V-VI), those cracks are related to the volatiles release and the high anisotropy of graphite's thermal expansion coefficient.

Fig. 4.6 presents the alumina-matrix interface of the three samples in detail. The JC sample's interface (Fig. 4.6-a) was well-connected, attesting the relatively high initial Young's modulus (Fig. A.1 - stage I). The HT1× and HT2× interfaces (Fig. 4.6-b and 4.6-c respectively) were highly affected by the thermal treatment. The latter was most influenced and a remarkable gap between the coarse alumina particles and the matrix can be observed.

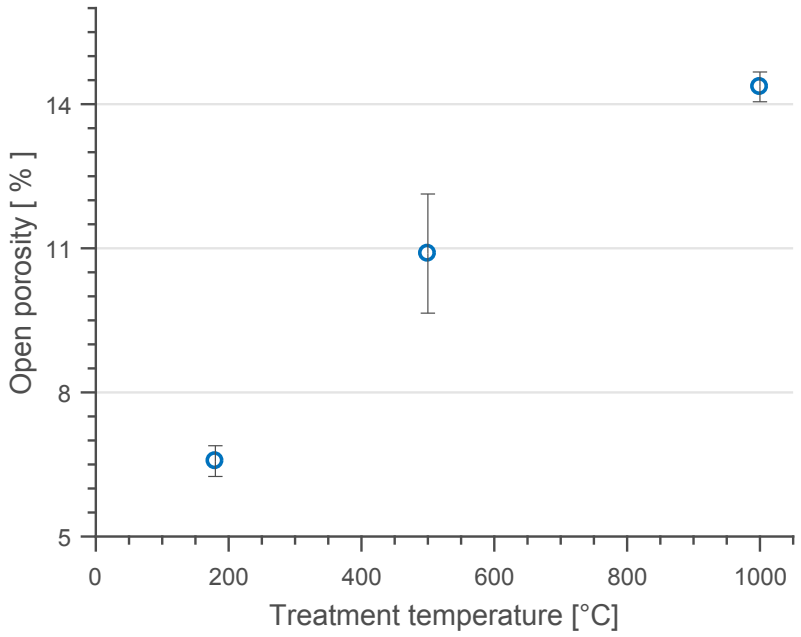

Figure 4.4: Open porosity with confidence intervals as a function of the treatment temperature (JC at 180 °C, HT1× at 500 °C, and HT2× at 1000 °C.)

The typical graphite basal plane cracks are shown in Fig. 4.7. Those cracks are related to the graphite's highly anisotropic thermal expansion coefficient. The graphite basal cracks and the matrix volatiles-release cracks were primarily responsible for the behavior of the Young's modulus between the stages V–VI, cf. Fig. 4.1.

Certainly the stresses generated in the matrix due to the volatiles release and the thermal expansion mismatch between the matrix and the graphite (perpendicular direction) are higher than the ones generated at the alumina-matrix interface. This can be explained by a higher thermal expansion mismatch between the graphite and matrix if compared to the one between alumina and matrix.

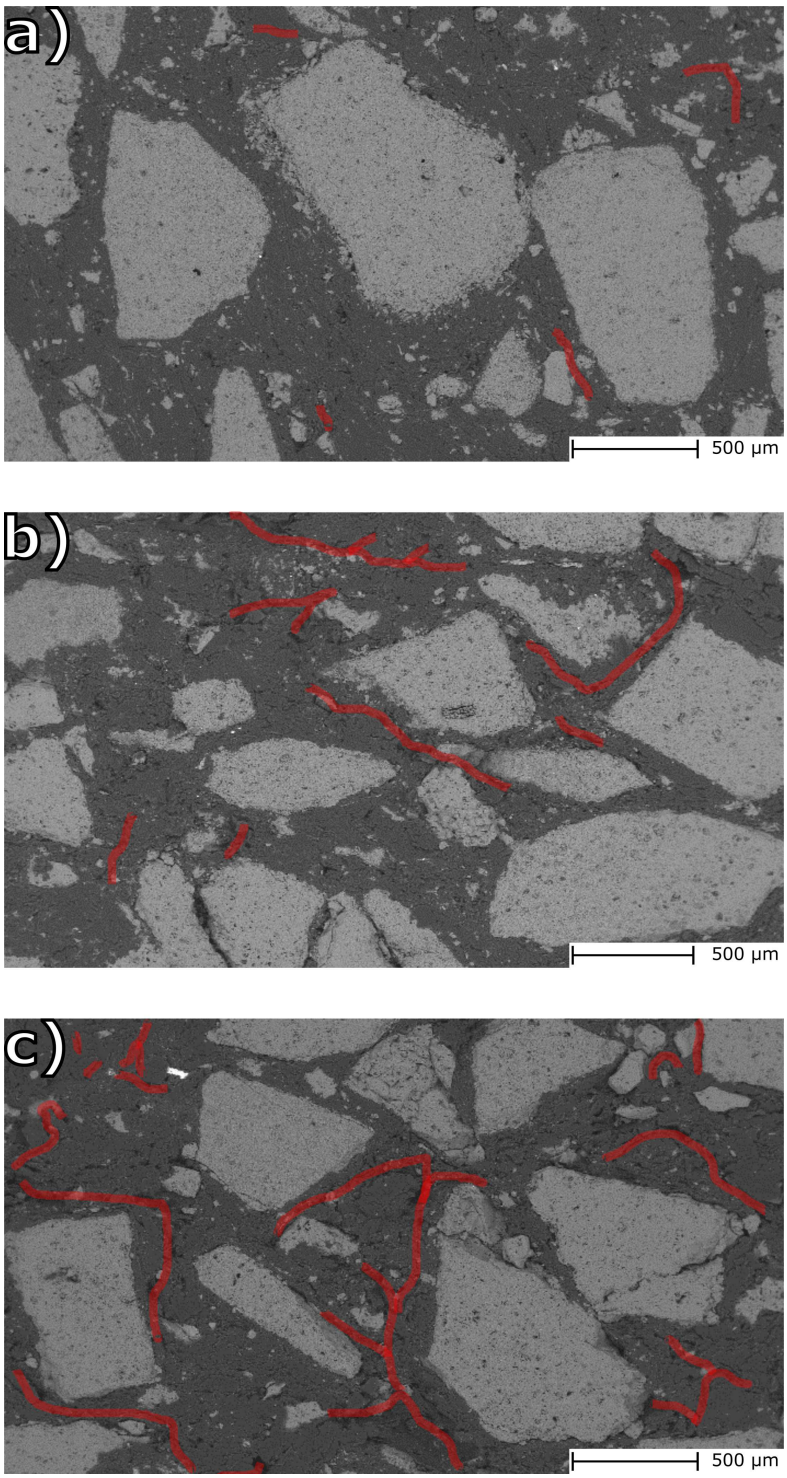

Figure 4.5: SEM micrographs: a) JC at 180 °C; b) HT1× at 500 °C, and HT2× at 1000 °C. In order to better visualize the crack location and its extension, they were highlighted in red.

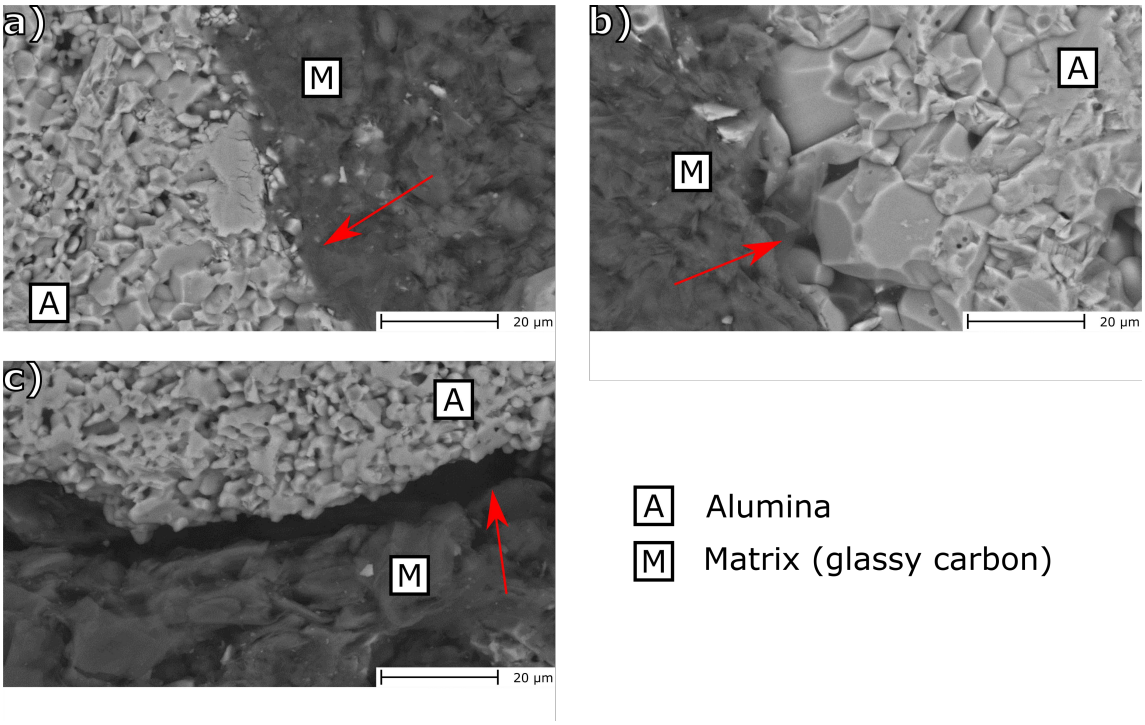

Figure 4.6: Alumina-matrix interface: a) JC at 180 °C; b) HT1× at 500 °C, and HT2× at 1000 °C.

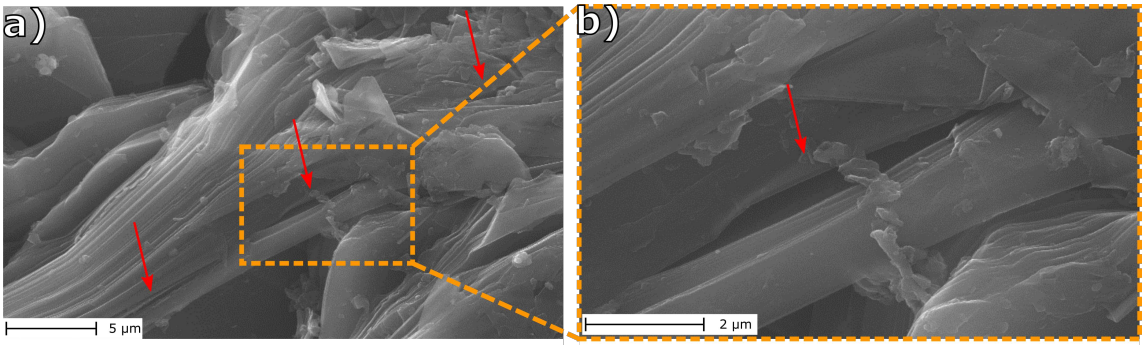

Figure 4.7: Typical graphite crack of a sample heat treated up to 1000 °C after two cycles.

4.1.5 Numerical simulation

The numerical model was developed in order to investigate the microstructure changes behind the non-linear Young's modulus problem (cf. Section 3.1.4) and present a more detailed vision of the proposed theory. Since for the stages VI–VII (Fig. 4.1) the explanation for the Young's modulus increase as a function of temperature was found in the closure of gaps, this thermal treatment was simulated and the results are discussed below.

In Fig. 4.8, the experimentally evaluated and numerically simulated effective Young's modulus have been compared. The Hashin-Shtrikman (HS) [124] model was employed to estimate the Young's modulus of the matrix. The two HS bounds (HS^- and HS^+) and their simple average (HS^*) were considered for the matrix's E, resulting in three different likely composites.

The simulations presented an excellent agreement with the experimental data. The assumption of calculating the matrix Young's modulus with the Hashin-Shtrikman model seems to be valid, as the numerical results were very close to the real ones.

All simulations were able to detect the gaps-closure phenomenon, resulting in a non-linear Young's modulus behavior. Therefore, the closure of the gaps, due to the thermal expansion mismatch between the phases, can be stated to be the main cause for the effective Young's modulus increase, attesting the suggested theory by Franklin and Tucker [103] and Werner *et al.* [104]. Furthermore, it can be concluded that the model materials can be used to analyze the complex behavior of the real heterogeneous ones.

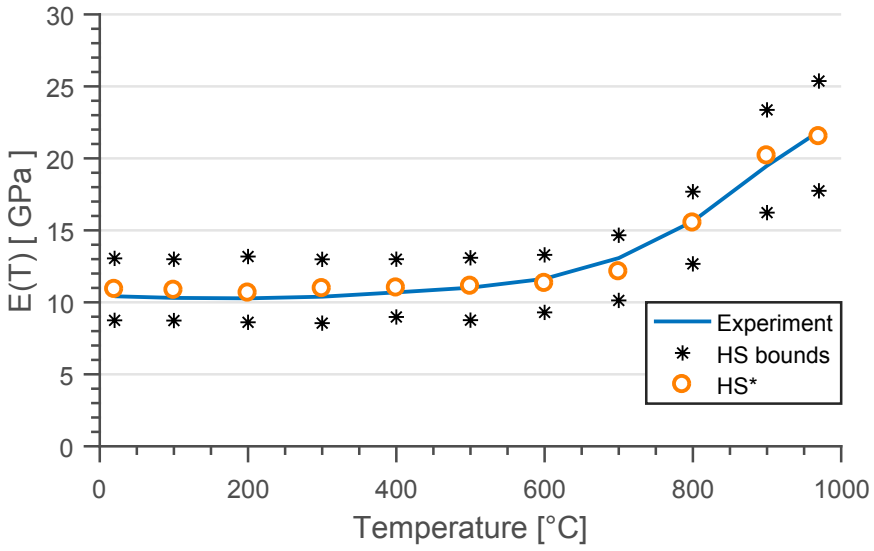

Figure 4.8: Experimental and numerical Young's modulus as a function of temperature. HS bounds were simulated considering the upper and lower matrix Young's modulus calculated by the Hashin-Shtrikman model. HS* was simulated considering the bounds average as the matrix Young's modulus.

Fig. 4.9 presents the stress state (*von Mises* stress) of the virtual sample at three distinct temperatures. It is possible to observe that, as the temperature increases, the gaps are progressively closed and stresses are generated in the microstructure. The white dots on the images

represent the gaps between particles and matrix that are still not closed.

One important result, that could be obtained from the finite element simulation, was the determination of the graphite's key role in the thermal stresses state. As can be noticed in Fig. 4.9, the thermal stresses join into a network shape that is entirely dependent on the graphite's positioning, in correspondence with the real samples' cracks (Fig. 4.5).

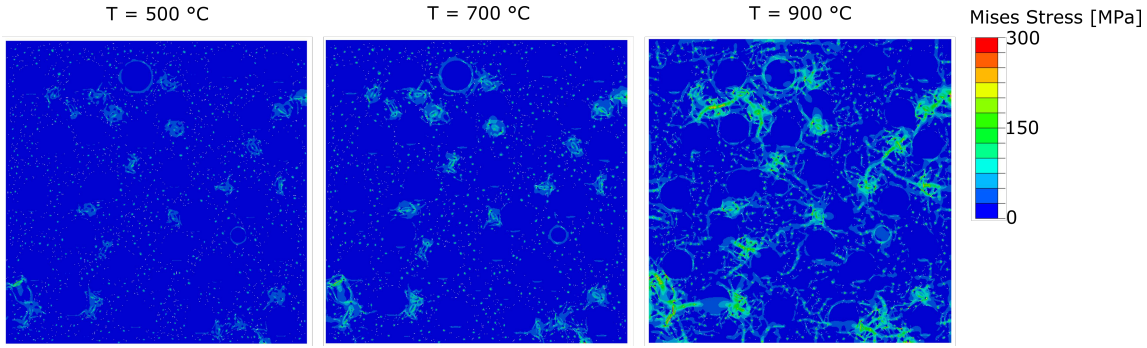

Figure 4.9: Stress state of a virtual Al_2O_3-C sample at three distinct temperatures (finite element simulation).

The dwell time and the cooling step of the second thermal treatment cycle (stages VII–VIII, VIII–IX and IX–X of Figure 4.1) were not considered in the simulations, as they involve viscoplastic phenomena (Section 4.1.1, page 51).

4.1.6 Discussion

Based on the thermo-mechanical experiments (Young's modulus measurements via IET, thermogravimetric analysis, porosity measurement and microstructure assessments) and finite element simulation (model materials), it was possible to characterize and correlate the behavior of carbon-bonded alumina bulk samples at high temperatures with their processing route.

The original Young's modulus characterization as function of temperature was corroborated by the several experiments performed during this study. It was observed that the thermal expansion mismatch between phases are not the sole responsible for the unusual Young's modulus behavior at high temperatures, but complementary, the volatiles release during the resin's thermal treatment plays a major role for the final microstructure and, consequent, thermo-mechanical behavior.

Finite element analysis at the micro-scale level was in a good agreement with the experiments, proving that model materials simulation can be used to assess complex behaviors of refractories.

4.2 Carbon-bonded alumina foam filters: A comparison of processing routes

4.2.1 X-ray computer tomography (µCT)

The analysis of the filters after each preparation step using CT technique provided crucial information on both, *RS* and *CF*, procedures. Figure 4.10 presents the volume rendered images of the 6 regions of interest (*WS*, *LB*, *LT*, *CC*, *RB*, and *RT*) from the sample *RS* after the first coating. As at this stage the sample was not yet thermally treated, the rendered images comprise PU foam and the ceramic coating (viewed as a single material due to the binarisation step). Qualitatively, the regions show no noticeable differences in strut diameter and surface roughness, and no closed cells were detected. In the following paragraphs, quantitative analyses will be introduced.

After the CT post-treatment, it was possible to display the wall thickness distribution of each region of interest (ROI). Figure 4.11 shows the wall thickness distribution of the six ROIs of the sample *CF-T2* after the first thermal treatment. It is clear that the distribution is non-symmetric.

Therefore, using the traditional parameters (average and standard deviation assuming a normal distribution) to characterize each ROI would imply a significant error of misrepresentation (Figure 4.12a). Using the MATLAB^{TM} software, it was possible to identify that the filters wall-thickness values were well fitted by a log-normal function (Figure 4.12b). As it can be seen, there is still a certain error associated with a log-normal distribution, although it is significantly lower than when assuming a normal one.

Therefore, the geometrical mean (μ), standard deviation (σ), the 2σ range (representing 68% of the total wall thicknesses) and the coefficient of determination R^2 (representing the quality of the log-normal approximation to the CT data) were chosen as variables to characterize and compare distinct regions and filters.

Firstly, a CT analysis of a 10 ppi PU foam without any ceramic coating was carried out. This analysis intended to certify that the replica material presented a homogeneous distribution, ensuring that the conclusions drawn from the filter analysis were only dependent on the coating procedure and not on the polymeric foam template.

As it can be seen in Table 4.1, the PU foam presented a quite uniform strut thickness distribution. The maximum difference of the mean wall thickness was 0.02 mm. One can notice

Feature	Region					
	WS	CC	LB	LT	RB	RT
μ [mm]	0.15	0.14	0.16	0.15	0.15	0.16
2σ range [mm]	$0.15^{+0.111}_{-0.064}$	$0.14^{+0.097}_{-0.057}$	$0.16^{+0.117}_{-0.068}$	$0.15^{+0.116}_{-0.065}$	$0.15^{+0.119}_{-0.066}$	$0.16^{+0.128}_{-0.071}$
R^2	0.88	0.84	0.74	0.77	0.73	0.65

The voxel size was $40 \times 40 \times 40\,\mu m^3$.

Table 4.1: Wall thickness distribution of distinct regions of a 10 ppi PU foam without coating (the parameters μ and σ were calculated assuming a log-normal distribution)

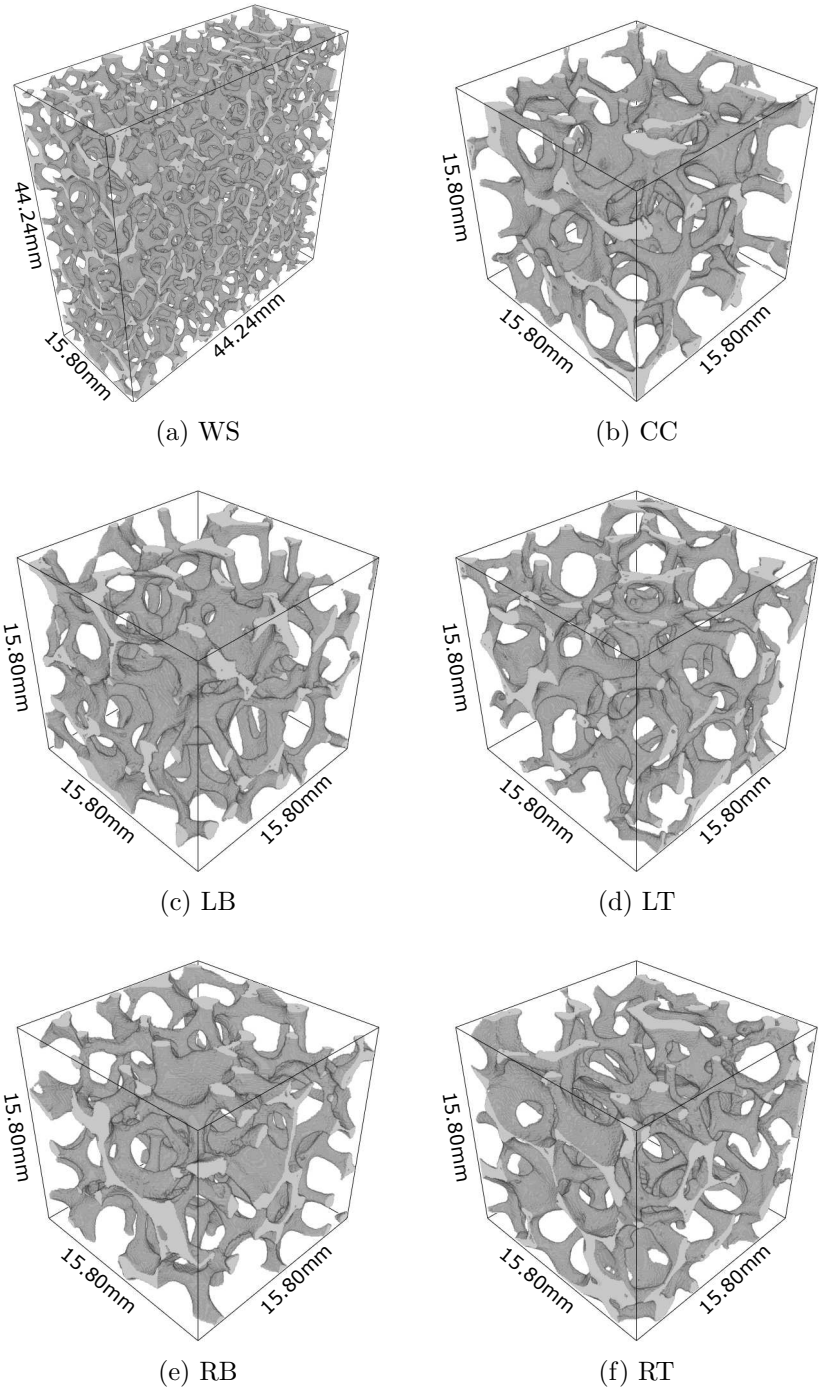

(a) WS (b) CC

(c) LB (d) LT

(e) RB (f) RT

Figure 4.10: Rendered images of the six regions of interest of the rolled and sprayed filter *RS* (still with PU foam) after the first coating. *WS*, *CC*, *LB*, *LT*, *RB* and *RT* stand for whole sample, center, left bottom, left top, right bottom and right top, respectively.

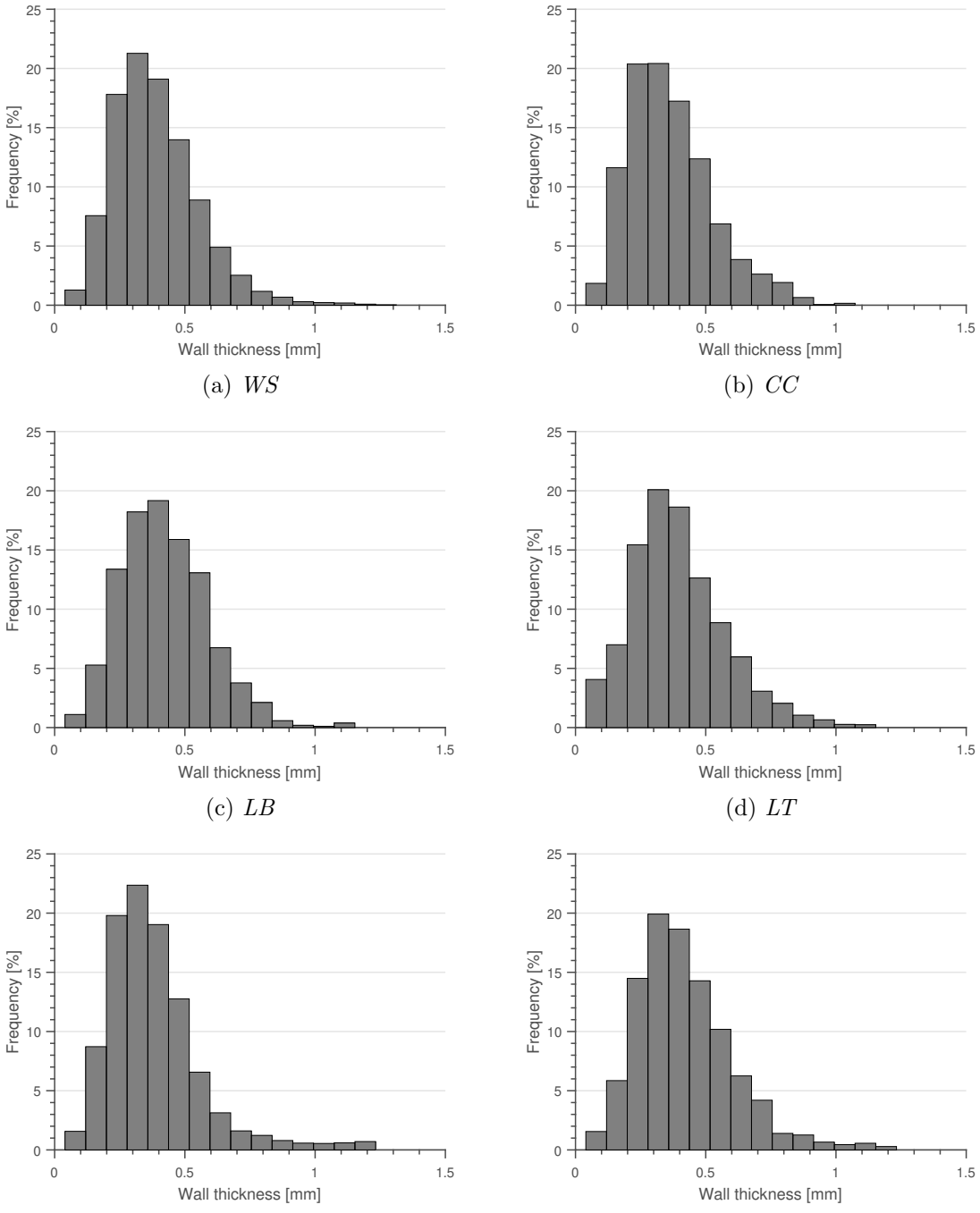

(a) *WS* (b) *CC*

(c) *LB* (d) *LT*

(e) *RT* (f) *RB*

Figure 4.11: Wall thickness distribution of distinct ROIs of the sample *CF-T2*, after first thermal treatment.

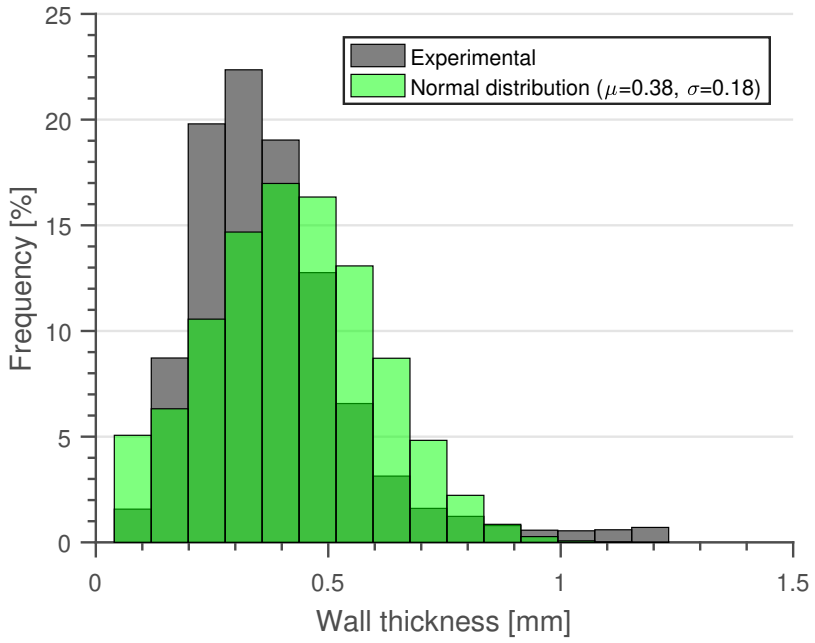

(a) Approximation with a normal distribution

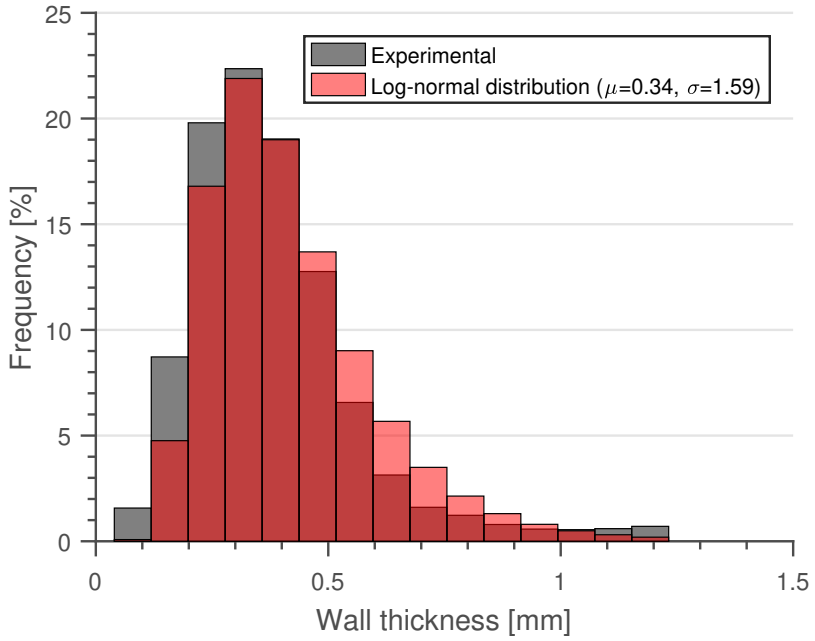

(b) Approximation with a log-normal distribution

Figure 4.12: Wall thickness distribution of the *RT* ROI of the sample *CF-T2*, after first thermal treatment – normal and log-normal approximations.

lower values of R^2 for the PU foam when compared to the coated filters (Tables 4.2, 4.3 and 4.4). This indicates that the log-normal profile is mainly related to the coating processes (spraying and centrifugation) and not to the polymeric foam itself.

Tables 4.2 - 4.4 present the data for the filters *RS*, *CF-T1* and *CF-T2*, respectively. It must be mentioned that only the ROIs *WS* and *CC* can be directly compared at distinct processing stages, due to the randomic positioning of the samples inside the tomograph. As the samples were randomly positioned, the other ROIs are statistically distributed in different positions at distinct stages.

Based on the Tables 4.2 - 4.4, it can be stated that the log-normal distribution satisfactorily fits the CT data, validating the regions characterization (the minimal R^2 value after firing is 0.93). For all samples, the porosity values achieved at the 2nd coating and after firing were in the same range. This indicates a low global shrinkage.

The volume shrinkage was calculated using the CT data. Firstly, the filters global dimensions were measured using the MAVI software. To do so, the filters were assumed as presenting a rectangular parallelepiped geometry and the six planes containing their external surfaces were identified. By calculating the distance of the opposite planes, it was possible to estimate the filter global dimensions and consequently its volume. These measurements were made before (V_{BF}) and after (V_{AF}) the firing step. Comparing the filters volume at both steps allowed the calculation of the volume shrinkage after the firing process (Equation 4.1). As the definition of the external planes was not automatically chosen, it is reasonable to assume an operator error of $\pm$ 1 voxel.

$$\text{Volume Shrinkage} = \frac{V_{BF} - V_{AF}}{V_{BF}} \tag{4.1}$$

The volume shrinkage for the filter *RS* (7.7 %) is in the same range as the value calculated by Emmel and Aneziris [36] for carbon-bonded alumina filters (8.2 %) after complete heat treatment. The filter *CF-T1* presented the highest volume shrinkage, whereas the *CF-T2* presented the lowest one. The former is due to the lower solid content and consequent higher amount of water in the 2nd coating centrifugation slurry (solid content of 65 wt.% - Table 3.2) if compared to the spraying slurry (solid content of 70 wt.% - Table 3.2). For the *CF-T2* procedure, as the sample already experienced contraction during the first thermal treatment, the shrinkage measured after the second one is smaller.

The local shrinkage of the wall thickness (in the struts radial direction) after firing was another feature analyzed from the CT data. To estimate this variable, the mean (μ) wall thickness of the whole sample (*WS*) at the 2nd coating was compared to the μ after firing. In the case of the filters heat-treated just once (*RS* and *CF-T1*), the mean wall thickness of the PU foam (Table 4.1) was subtracted from the 2nd coating mean wall thickness (Table 4.2), as at the binarisation step, the PU foam and the ceramic coating were considered as one entity. Differently from the global volume shrinkage, where 6 planes were subjectively defined, the struts mean radial shrinkage used the mean wall thickness assuming the log-normal distribution, thus the shrinkage error is a function of the distribution quality. Therefore, Table 4.5 presents only the mean values of this variable.

The same trend presented for the global volume shrinkage was also observed for the radial one, see Table 4.5. The *CF-T1* filter showed the highest shrinkage, whereas the *CF-T2* presented the lowest. This is again associated to the lower solid content of the 2nd coating centrifugation

Stage	Feature	Region					
		WS	CC	LB	LT	RB	RT
1st	Porosity [%]	88	89	88	89	87	87
coating*	μ [mm]	0.44	0.41	0.45	0.43	0.48	0.46
	2σ range [mm]	$0.44^{+0.233}_{-0.152}$	$0.41^{+0.213}_{-0.140}$	$0.45^{+0.225}_{-0.150}$	$0.43^{+0.219}_{-0.145}$	$0.48^{+0.259}_{-0.168}$	$0.46^{+0.253}_{-0.163}$
	R^2	0.96	0.94	0.96	0.95	0.94	0.92
2nd	Porosity [%]	75	75	72	76	72	79
coating*	μ [mm]	0.75	0.75	0.86	0.69	0.83	0.65
	2σ range [mm]	$0.75^{+0.420}_{-0.269}$	$0.75^{+0.398}_{-0.260}$	$0.86^{+0.430}_{-0.287}$	$0.69^{+0.359}_{-0.236}$	$0.83^{+0.473}_{-0.301}$	$0.65^{+0.351}_{-0.228}$
	R^2	0.95	0.91	0.87	0.92	0.95	0.97
After	Porosity [%]	76	77	80	73	77	73
firing	μ [mm]	0.54	0.51	0.47	0.61	0.50	0.60
	2σ range [mm]	$0.54^{+0.329}_{-0.205}$	$0.51^{+0.296}_{-0.187}$	$0.47^{+0.287}_{-0.178}$	$0.61^{+0.366}_{-0.229}$	$0.50^{+0.290}_{-0.184}$	$0.60^{+0.360}_{-0.225}$
	R^2	0.96	0.95	0.96	0.96	0.96	0.93

*Binarisation step considered the PU foam and the ceramic coating as a single material.

Table 4.2: Total porosity and wall thickness distribution of distinct regions of the filter *R+S* (the parameters μ and σ were calculated assuming a log-normal distribution).

Stage	Feature	Region					
		WS	CC	LB	LT	RB	RT
1st coating*	Porosity [%]	88	87	89	90	87	88
	μ [mm]	0.48	0.46	0.47	0.46	0.52	0.48
	2σ range [mm]	$0.48^{+0.242}_{-0.161}$	$0.46^{+0.229}_{-0.152}$	$0.47^{+0.224}_{-0.152}$	$0.46^{+0.236}_{-0.156}$	$0.52^{+0.257}_{-0.172}$	$0.48^{+0.244}_{-0.162}$
	R^2	0.98	0.96	0.97	0.97	0.96	0.95
2nd coating*	Porosity [%]	74	71	75	77	72	74
	μ [mm]	0.73	0.79	0.70	0.71	0.78	0.74
	2σ range [mm]	$0.73^{+0.372}_{-0.247}$	$0.79^{+0.387}_{-0.260}$	$0.70^{+0.350}_{-0.233}$	$0.71^{+0.376}_{-0.246}$	$0.78^{+0.406}_{-0.267}$	$0.74^{+0.392}_{-0.256}$
	R^2	0.98	0.95	0.97	0.97	0.95	0.97
After firing	Porosity [%]	74	73	73	75	75	78
	μ [mm]	0.50	0.49	0.52	0.49	0.49	0.49
	2σ range [mm]	$0.50^{+0.225}_{-0.155}$	$0.49^{+0.211}_{-0.147}$	$0.52^{+0.229}_{-0.159}$	$0.49^{+0.221}_{-0.152}$	$0.49^{+0.221}_{-0.152}$	$0.49^{+0.235}_{-0.159}$
	R^2	0.98	0.98	0.98	0.98	0.98	0.98

*Binarisation step considered the PU foam and the ceramic coating as a single material.

Table 4.3: Total porosity and wall thickness distributions of distinct regions of the filter *CF-T1* (the parameters μ and σ were calculated assuming a log-normal distribution).

Stage	Feature	Region					
		WS	CC	LB	LT	RB	RT
1st	Porosity [%]	87	87	86	87	85	88
coating	μ [mm]	0.35	0.33	0.39	0.35	0.38	0.34
	2σ range [mm]	$0.35^{+0.193}_{-0.124}$	$0.33^{+0.198}_{-0.124}$	$0.39^{+0.211}_{-0.137}$	$0.35^{+0.235}_{-0.140}$	$0.38^{+0.224}_{-0.141}$	$0.34^{+0.201}_{-0.126}$
	R^2	0.96	0.93	0.96	0.96	0.97	0.95
2nd	Porosity [%]	77	75	79	79	76	78
coating	μ [mm]	0.49	0.49	0.49	0.45	0.51	0.49
	2σ range [mm]	$0.49^{+0.211}_{-0.147}$	$0.49^{+0.198}_{-0.124}$	$0.49^{+0.196}_{-0.140}$	$0.45^{+0.198}_{-0.138}$	$0.51^{+0.230}_{-0.158}$	$0.49^{+0.225}_{-0.154}$
	R^2	0.98	0.98	0.98	0.97	0.97	0.97
After	Porosity [%]	78	76	77	79	79	79
firing	μ [mm]	0.46	0.47	0.46	0.46	0.45	0.44
	2σ range [mm]	$0.46^{+0.207}_{-0.143}$	$0.47^{+0.212}_{-0.146}$	$0.46^{+0.207}_{-0.143}$	$0.46^{+0.212}_{-0.145}$	$0.45^{+0.203}_{-0.140}$	$0.44^{+0.194}_{-0.134}$
	R^2	0.98	0.97	0.98	0.97	0.98	0.97

Table 4.4: Total porosity and wall thickness distributions of distinct regions of the filter *CF-T2* (the parameters μ and σ were calculated assuming a log-normal distribution).

Filter	Global shrinkage [%]	Struts radial mean shrinkage [%]
RS	7.7 ± 0.8	10.0
CF-T1	9.1 ± 0.8	13.8
CF-T2	1.4 ± 0.8	6.1

Table 4.5: Filter shrinkage after firing

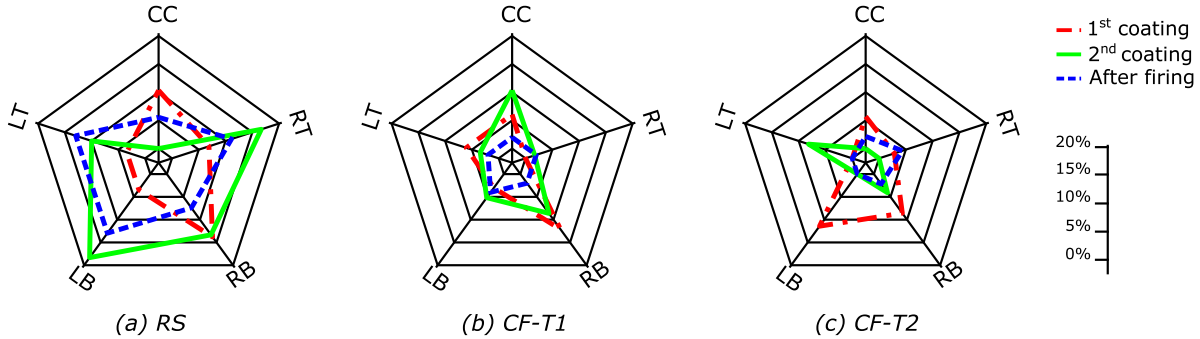

Figure 4.13: Normalized difference between the local and the global wall thickness means.

slurry compared to the spraying one and the additional thermal treatment for the samples *CF-T2*.

For all filters, the radial shrinkage was noticed to be significantly higher than the volume one, due to the measurement procedure. For the volume shrinkage, the filter was assumed as presenting a rectangular parallelepiped geometry and its volume was compared before and after firing. Therefore, the values calculated for the volume shrinkage were only dependent on the filter's global dimensions and can be considered as an effective value. Conversely, the strut's radial shrinkage was only associated to the Al_2O_3-C composition, hence it was considerably higher.

Intending to summarize the data from Tables 4.2, 4.3 and 4.4 and to directly compare the filters features, the normalized differences of the regions of interest (*CC*, *LB*, *LT*, *RB*, *RT*) compared to the *WS* region (Figure 4.13), were calculated.

One can notice a higher variability for the results of the *RS* filter when compared to the *CF-T1* and *CF-T2* ones. Whereas *CF-T1* and *CF-T2* filters presented a variation within the range of 0 and 5% after firing, this value was 10% to 15% for the *RS*.

This variation is related to the filter coating process, as the spraying method is mostly manual. The centrifugation method, in turn, is less dependent on the operator, presenting, consequently, a lower variability. Moreover, the centripetal force can be considered as uniformly applied to the whole sample (filter dimensions are too small compared to the centrifugal radius) [174], so this technique is more reliable.

Another important feature analyzed by the CT data was the influence of the firing step on the ceramic material homogeneity. For all filters, the ranges of variability after firing were smaller than for the 2nd coating step. This indicates that during firing, the material diffuses, giving rise to more homogeneous samples.

To better investigate this behavior, a statistical test for homogeneity of variances (Fligner-Killeen) [175] was used. The normalized mean differences of the ROIs of the three processing procedures were compared before and after firing. If the p-value is lower than 0.05, it means that there is a significant difference between the variances and the null hypothesis cannot be stated. In the case of null hypothesis, it can be assumed that the variances in each sample are the same.

The tests resulted in p values of 0.5002, 0.0609 and 0.6861 for the *RS*, *CF-T1* and *CF-T2* filters, respectively. In all cases the p-values were greater than 0.05, hence it is not possible to statistically attest that the variances before and after firing are significantly different. Nevertheless, as the p-value of the sample *CF-T1* is lower than 0.1, it can be stated that there is a trend towards the material homogenization. It must be highlighted that only those 5 ROIs from each filter were analyzed.

The material uniformisation within the filter could be reinforced by the mesophase transformation of the Carbores® P between 400 and 550 °C. In this temperature range, Carbores® P is in a viscous state [36]. Therefore, during firing the filter would decrease its free energy associated with the external surface, smoothing it.

It must be mentioned that likely sources of errors during the CT analysis could be the limited spatial resolution of the CT images, imprecise positioning of the sample inside the CT equipment and a too coarse binarisation.

4.2.2 Microscopic analysis

CT measurements made possible to analyze the homogeneity of the filters wall thickness. However, little information could be assessed about the filters surface due to the limited resolution of the CT scans. Intending to further differentiate the *RS* and *CF* procedures, the filters surfaces were analyzed by digital optical microscopy. At least three samples from each processing procedure (*RS*, *CF-T1* and *CF-T2*) were evaluated.

Figures 4.14a to 4.14c present the optical microphraphs of *RS* filters. A very smooth surface can be observed, due to the high shear rate associated to the spraying process [36]. At higher shear rates, the slurry presents a lower viscosity being, consequently, better distributed on the template. In Figure 4.14a, a material concentration in the form of droplets can be observed, which is also related to the spraying process. Macrocracks due to the PU burnout can be also detected.

Figures 4.14d to 4.14f show the surfaces of filters produced by centrifugation and after one thermal treatment. Figure 4.14d shows the typical hollow strut cross-section, which was also found in *RS* samples. The *CF-T1* surfaces exhibited a coarser roughness when compared to the *RS* ones. This was most likely a result of to the higher water content in the 2nd coating centrifugation slurry. Some macro-cracks, also associated with the PU burnout, were found in the *CF-T1* filters.

Figures 4.14g to 4.14i show the optical microphraphs of the filters produced by centrifugation and thermally treated twice. The *CF-T2* filters presented the roughest surfaces. Firstly, the presence of pores at the surface can be associated with the higher water content in the 2nd coating centrifugation slurry. On the one hand, almost no macrocracks could be found in the filters structures. On the other hand, a high number of superficial microcracks were detected (Figure 4.14g).

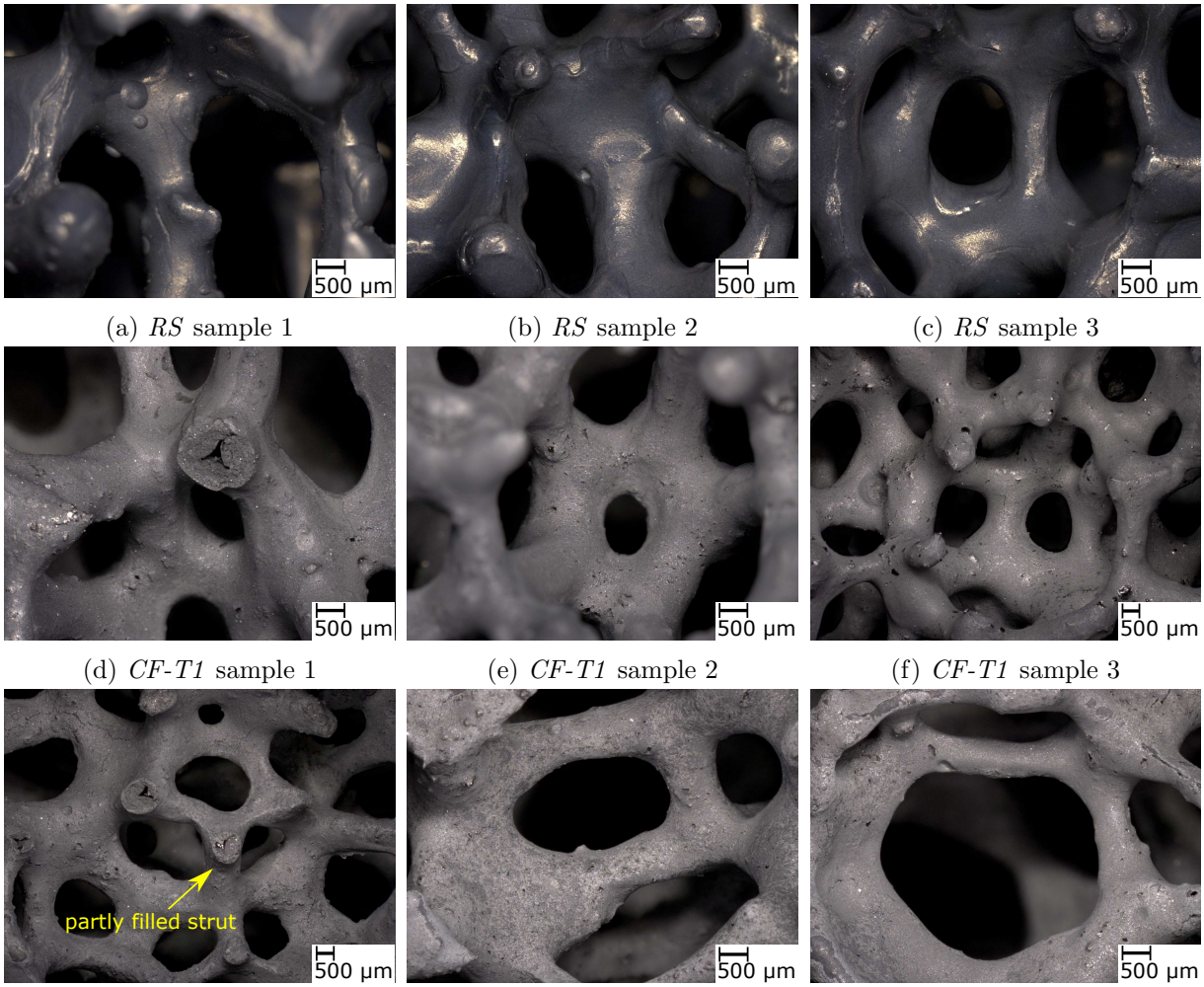

(a) *RS* sample 1 (b) *RS* sample 2 (c) *RS* sample 3

(d) *CF-T1* sample 1 (e) *CF-T1* sample 2 (f) *CF-T1* sample 3

(g) *CF-T2* sample 1 (h) *CF-T2* sample 2 (i) *CF-T2* sample 3

Figure 4.14: Optical micrographs of the samples *RS* (produced by roller + spraying and one thermal treatment), CF-T1 (produced by centrifugation and one thermal treatment) and CF-T2 (produced by centrifugation and two thermal treatments).

Figure 4.14g presents a partly filled strut, showing that the strategy of partially burning out the PU foam with the 1st thermal treatment was effective. Summing up the microscopy results, the *RS* filters presented the smoothest surfaces whereas the *CF-T2* the roughest ones.

Technologically, it is expected that the filters *CF-T2* would result in the highest filtration efficiency, as their external surface area is larger than those of *RS* and *CF-T1*, due to the large amount of microcracks. However, not only the external surfaces, but also the filter mechanical properties should be compared. The filters will be transported and handled for positioning, thus if they do not possess a minimal mechanical strength and friability resistance, they will break, contaminating the molten metal.

4.2.3 Preliminary tests on cold crushing strength

Figure 4.15 shows the force-displacement curves for one sample of each processing route. While the filters *RS* and *CF-T1* presented maximum forces in similar range, the *CF-T2* filter presented the lowest strength, mostly related to the presence of many micro-cracks on its surface.

It was observed that the existence of a high amount of superficial micro-cracks was much more deleterious to the filter's cold crushing strength than the presence of macro-cracks associated to the PU burnout.

Both *RS* and *CF-T1* presented similar strength levels but with distinct curve progression. The *RS* fracture behavior showed a non-linear increase with sharp drops in the force, indicating the breaking of single or few struts (in general the thinner ones). Afterwards, the force rises again, as consequence of stress redistribution within the remaining structure. On the other hand, the *CF-T1* curve was much smoother than the *RS* one. There are some small drops in force and consequent increase, but considerably less than for *RS*. This curve characteristic can be related to the material distribution within the filter. As the *CF-T1* filter presented a more homogeneous material distribution, it is conceivable that the stress distribution was optimized and the breaking of single or few struts due to local stress concentration during the cold crushing test was limited.

The final displacement (before complete failure) of the sample *CF-T2* was considerably higher than of the samples *RS* and *CF-T1* (Table 4.6). Both samples *RS* and *CF-T1* showed maximum displacements of approximately 2 mm, whereas the *CF-T2* value was approximately 7 mm. This extension is related to the brittleness of the struts due to the superficial microcracks, also called *brittle crushing* by Gibson and Ashby [26].

As the filters presented distinct strut thicknesses, directly comparing the force values from the CCS tests could lead to misevaluation. Therefore, a strength normalization was used. It was assumed that all filters presented the same number of struts (n). The struts were considered as simplified hollow cylinders with fixed wall thickness, as measured by CT (Tables 4.2-4.4). Thus, the compressive strength (CS) of each filter was calculated following the equation 4.2. The normalized value was determined assuming the *RS* result as the reference.

$$CS = \frac{\text{Max. force}}{n \cdot \pi \cdot \left[\left(\mu_{\text{after-firing}} + \frac{\mu_{\text{PU-foam}}}{2} \right)^2 - \left(\frac{\mu_{\text{PU-foam}}}{2} \right)^2 \right]} \tag{4.2}$$

Filter	$\mu_{\text{after-firing}}$ [mm]	Max. force [N]	Max. displ. [mm]	Norm. strength CS [-]
RS	0.54	844	1.97	1.00
CF-T1	0.50	750	2.28	1.02
CF-T2	0.46	130	6.70	0.20

Table 4.6: Maximum force, maximum displacement and normalized compressive strength of filters produced by different processing routes.

As visualized in Table 4.6, the filters *RS* and *CF-T1* presented similar normalized strength with distinct fracture behaviors. The filter *CF-T2* showed the lowest value, indicating that

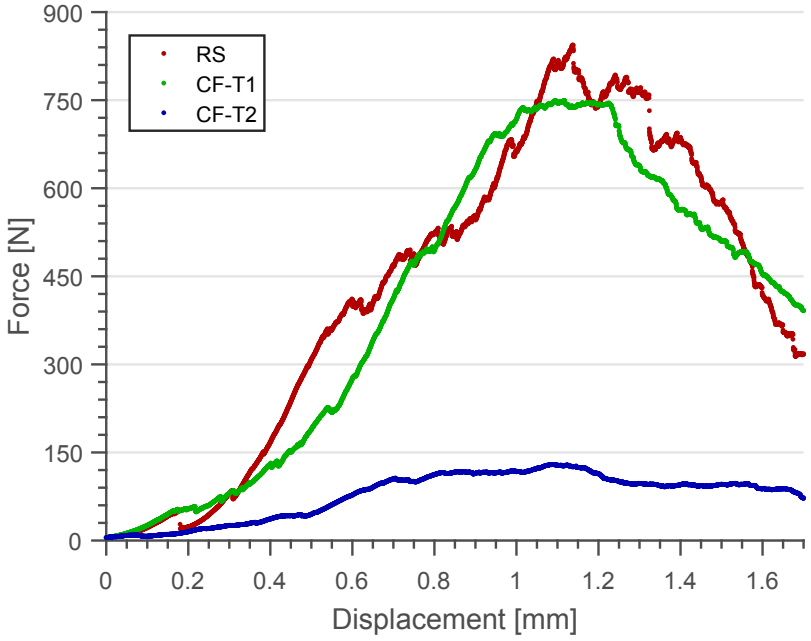

Figure 4.15: Force-displacement curves of the filters *RS*, *CF-T1* and *CF-T2* during cold crushing strength. The testing machine was controlled by displacement with cross-head speed of 1 mm/min.

the surface micro-cracks drastically affected the filter CCS, determining the infeasibility of this processing route. It must be highlighted that only one filter from each processing route was analyzed.

4.2.4 Discussion

A deep evaluation of three distinct processing routes on the ceramic deposition of carbon-bonded alumina filters was analyzed. The strategy of using the computer tomography at several steps of the processing route was proved very useful, since based on the direct comparison of the inter-stage filters with their final geometry allowed a critical assessment of each processing step.

It was observed that the wall thickness values of all filters was well fitted by log-normal distribution functions. Therefore, the geometric mean (μ) and standard deviation (σ) are important parameters to characterize the filters' homogeneity.

The filters' volume and the struts' radial shrinkage were determined based on the CT analysis and the influence of the slurries' water content on those values was highlighted. The surface evaluation via optical microscopy revealed different surface roughness for the distinct processing routes. While the *RS* filters showed a relatively smooth surface with the presence of macrocracks, the *CF-T2* samples displayed a considerably high density of superficial microcracks.

Finally, a preliminary investigation of the cold crushing strength of the filters showed that due to the presence of the superficial micro-cracks, the *CF-T2* filters underperformed mechanically.

It was concluded that those microcracks were much more deleterious to the filters' strength than the macro-cracks related to the PU burnout.

4.3 Carbon-bonded alumina foam filters: The challenge of up-scaling

4.3.1 Mechanical characterization

Figure 4.16 summarizes the results from the cold crushing strength investigation. The brittle behavior of ceramics at room temperature and the highly porous structures are the main reasons for the scattering. Nonetheless, some important trends can be deduced from this Figure. Firstly, a higher mean strength (σ^*) associated to the CF vs. RS filters was observed. This result was valid despite the CF filters presenting lower relative density. The RS-S and RS-L strengths presented similar averages with slightly higher values for large size samples, whereas their scattering ranges were considerably different, being much narrower for the RS-S group. The CF-L filters showed the highest average strength but also the largest scattering in the relative density. The improvement of the mechanical strength due to higher sample size was quite remarkable for centrifuged filters, with the average value increasing from about to 0.2 to 0.4 MPa. During the mechanical testing, catastrophic failure of RS-L filters was always observed starting from the filter's inner core, whereas the thicker struts on the outside remained almost undamaged. The only advantage of impregnation followed by spray coating was a limited scatter of the strength values.

In order to prove the significance of the size and processing factors as well as of their interaction, a balanced two-way ANOVA was carried out with the aid of the software *R*. The statistical analysis pointed out that both factors (manufacturing process and sample size), as well as their interaction, were highly significant ($p < 2e^{-16}$ in all cases). The main reasons behind the distinct mechanical behavior shown by the different manufacturing process – sample dimensions combination will be given in Section 4.3.5.

Simply analyzing the strength as function of relative density does not offer a detailed view over the mechanical behavior. While performing the compression tests, a remarkably different fracture behavior could be noticed between filters produced by impregnation-spraying and those prepared by centrifugation. Figure 4.17 presents a comparison of the force-displacement curves for two samples produced by different routes but with similar mass (S) and crushing strength. Clearly the filter prepared by centrifugation showed a much smoother behavior in compression compared to the one produced by impregnation-spraying. This result corroborates the findings of the preliminary tests described in the previous Section (Figure 4.15).

Furthermore, when considering the results for the 120 samples from Figure 4.16, normalized force-displacement curves were obtained (see Figure 4.18). Each curve was normalized individually with a fixed number of points and extreme values for force and displacement as zero and one.

The mean values and confidence intervals confirmed what was observed for the single filters (see Figure 4.17), i.e. the filters produced by centrifugation showed in general a very smooth behavior in compression, whereas the RS samples were damaged in a more irregular way (larger confidence interval). A sample size effect could also be derived from this investigation. For both

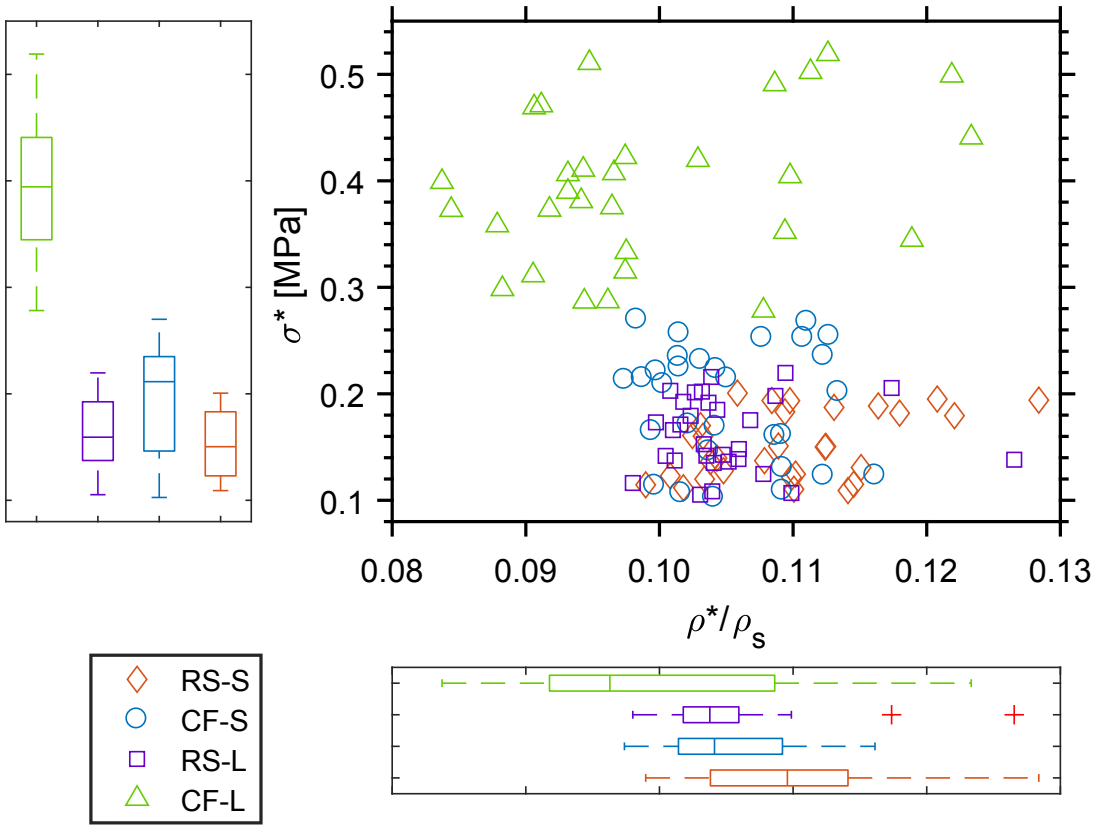

Figure 4.16: Cold crushing strength *versus* relative density of the filter samples produced by different routes and presenting different dimensions: CF = Centrifugation; RS = Spraying; S = Small samples; L = Large samples. Boxplot results are presented next to the respective axes.

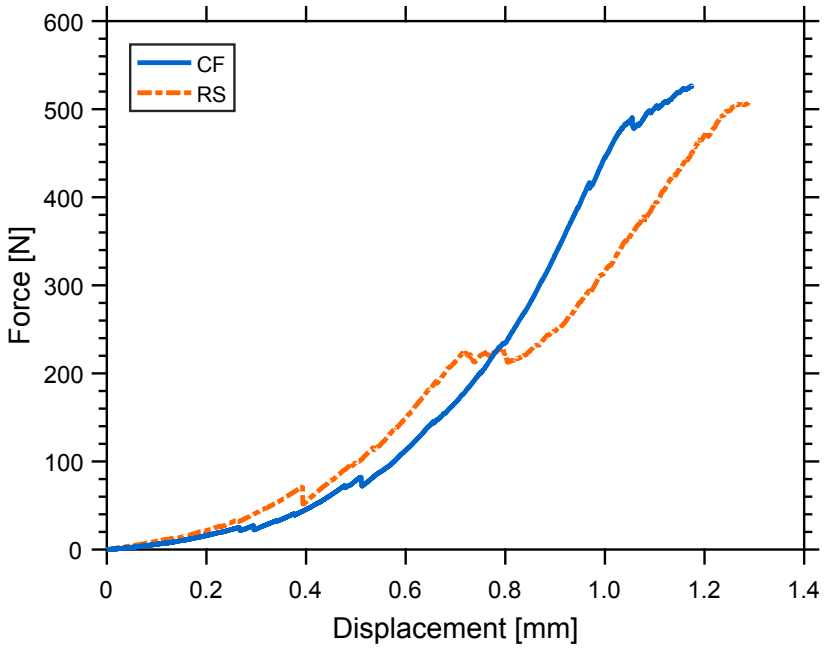

Figure 4.17: Force-displacement curve for S samples with the same theoretical cross-section area and height produced by different routes: CF = Centrifugation; RS = Spraying.

processing routes, the confidence interval of crushing strength for large samples was narrower than for their small counterparts. This behavior can be explained by a better stress redistribution after single struts' failure in the case of large filters. As the S filters presented a significant lower volume than the L ones (1/8), the impact of single strut breakage on the global behavior was much more relevant.

4.3.2 Microscopic analysis

Optical micrographs of two *S* and *L* samples prepared via the different routes are presented in Figure 4.19 and 4.20, respectively. It can be observed that strut tapering was predominant in the samples prepared by impregnation-spraying. As reported by Werzner et al. [160], for artificial computationally-generated geometries with high strut shape factor, the concentration of filter material at the joints of the RS specimens was responsible for closing some small windows between adjacent pores. Cracks were observed on both structures, but particularly on the CF samples, due to the lower strut thickness in general. Nevertheless, the cold crushing strength of such filters was generally higher, as presented in Figure 4.16.

The main reason for the filter material accumulating at the joints of the RS filters may be related to the high shear rate to which the Al_2O_3-C slurry was submitted during the spraying step. As shown by Fischer et al. [176] and Jankovský et al. [177], the shear rate during a spraying process can reach $1000\,s^{-1}$. Based on the rheological study of the Al_2O_3-C suspension by Emmel and Aneziris [36], the applied slurry presents a pronounced shear-thinning behavior resulting in a relative low viscosity at this high shear rate.

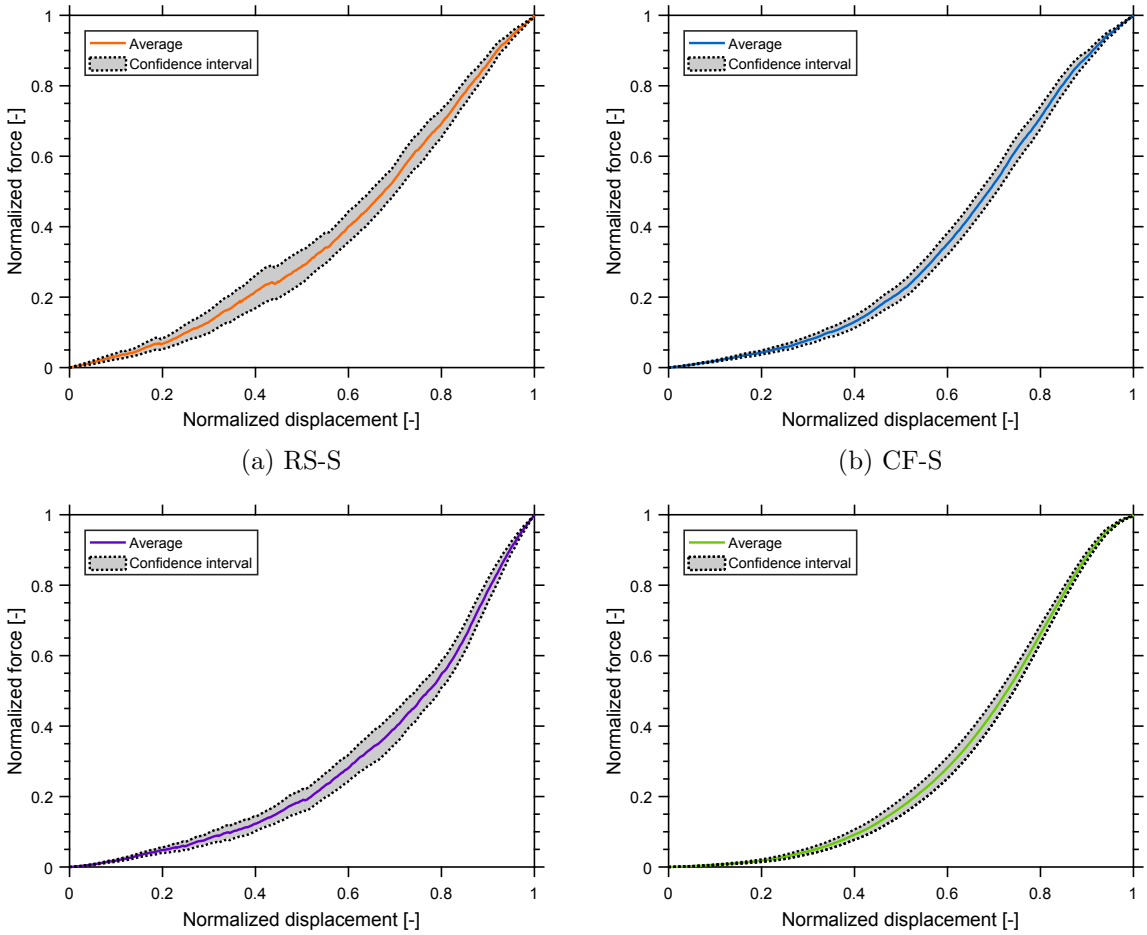

(a) RS-S (b) CF-S

(c) RS-L (d) CF-L

Figure 4.18: Normalized force-displacement curves of the distinct processing routes – sample size combination. The curves and the confidence intervals are the result of 30 samples force-displacement normalization.

It can be assumed that the surface of foam structures is not energetically stable. Therefore, liquid slurry is likely to accumulate at the joints, minimizing the surface energy. However, the higher viscosity associated to the lower shear rate of the centrifugation procedure slows this process down and less tapered struts are obtained from it.

Comparing the micrographs of Figures 4.19 and 4.20 with the ones from Figure 4.14 (Section 4.2.2) makes it possible to conclude that the rough surface of the *CF* filters presented in the previous Section was mainly related to the lower solid content of the centrifugation slurry. As a thicker slurry was used in this Section, comparable roughness between *RS* and *CF* surfaces were achieved.

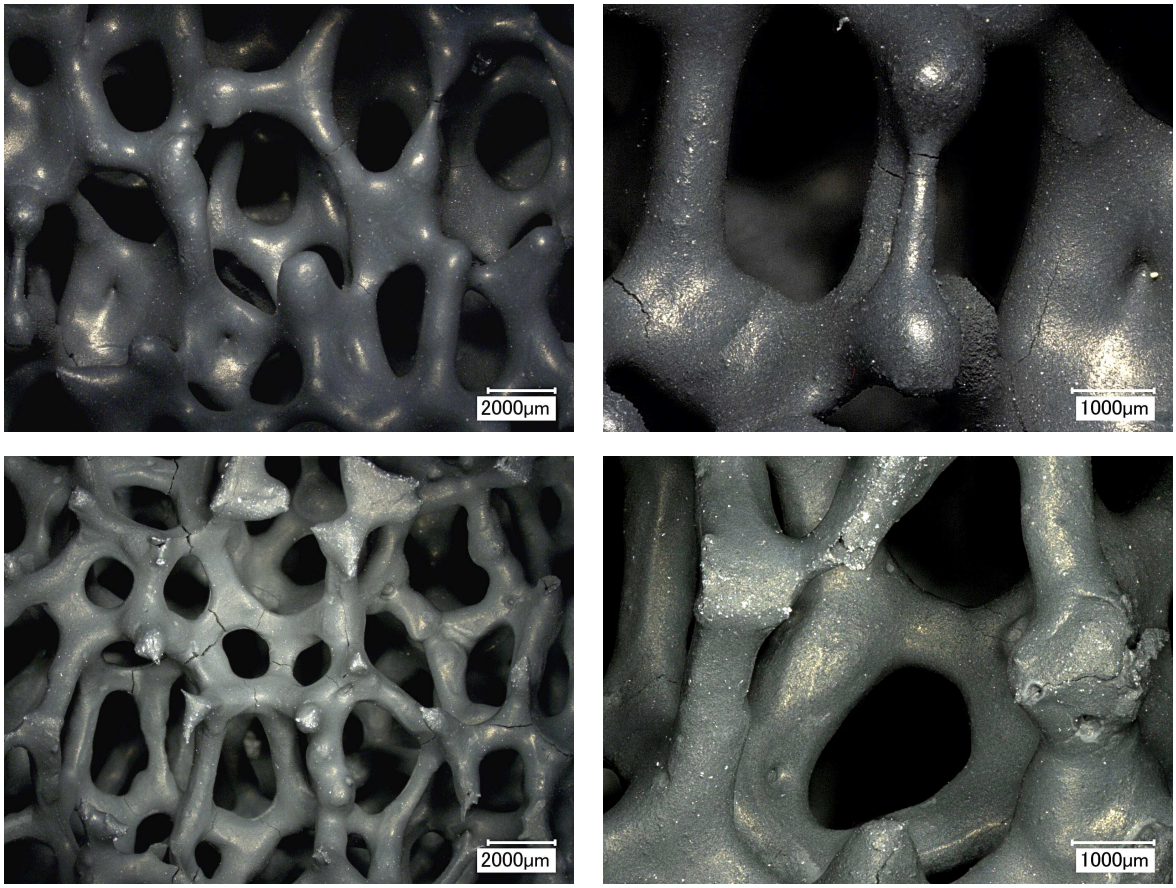

Figure 4.19: Optical micrographs of small filters prepared via different routes. Top: RS-S = impregnation-spraying, small sample; Bottom: CF-S = double centrifugation, small sample.

4.3.3 X-ray computer tomography (µCT) analysis

As explained in Section 3.3.3, the strategy used to assess the geometric features of ceramic filters was based on the results of Section 4.2.1 (Page 61) which showed that the wall thickness distributions of filters prepared by impregnation-spraying or centrifugation can be approximated by log-normal functions. Therefore, each sample was divided into regions of interest (ROIs) and a deeper local investigation on the material distribution was carried out.

Figure 4.21 presents the wall thickness distribution for two ROI's of S samples produced by the distinct routes. The geometric mean value (µ) was almost the same, 0.41 mm for the CF-S sample and 0.43 mm for the RS-S one. However, the geometric standard deviation (σ) was clearly smaller for the filter produced by centrifugation, whose wall thickness did not exceed 1 mm. One can understand σ as a parameter to describe the broadness of the wall thickness distribution. Low σ values indicate that the whole ROI presents similar wall thicknesses. Conversely, high σ would indicate a considerable scattering of wall thickness within the ROI.

Furthermore, linearly interpolating the data of the ROIs provided a global visualization of

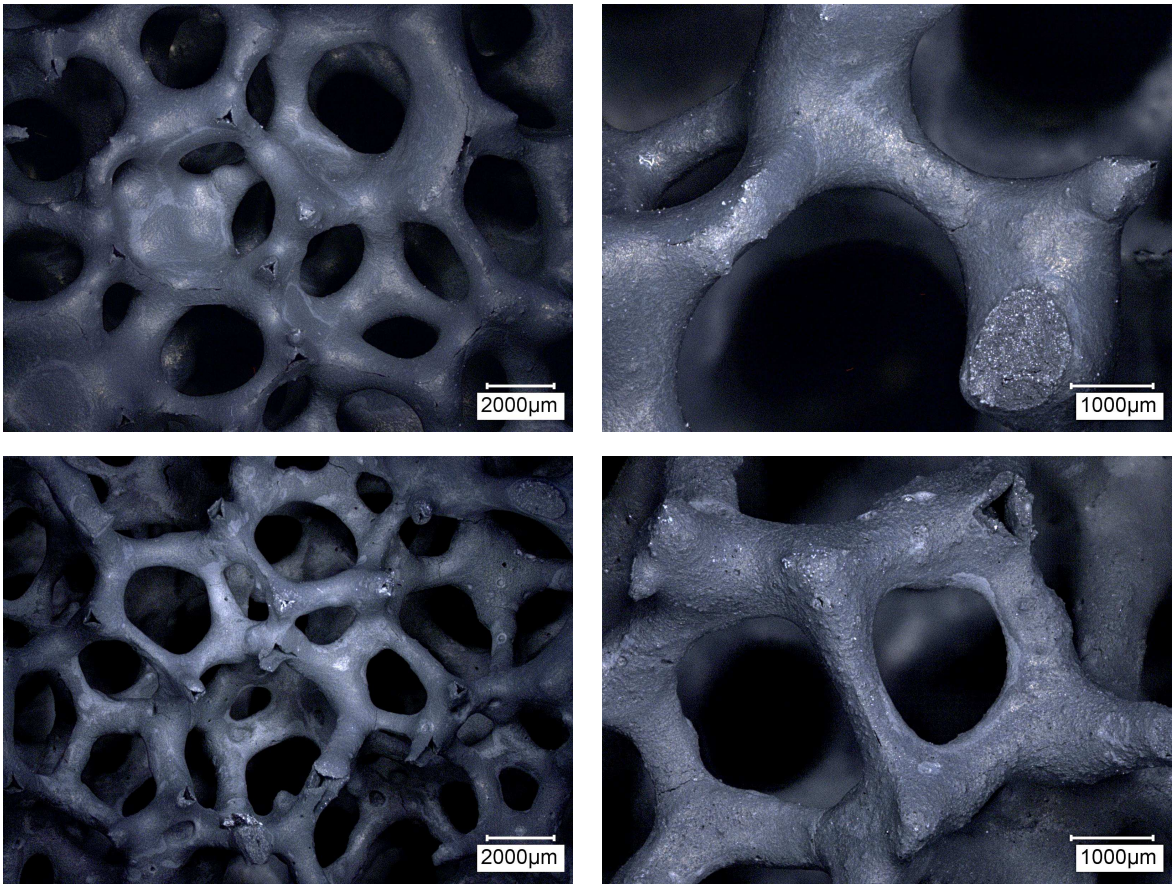

Figure 4.20: Optical micrographs of large filters prepared via different routes. Top: RS-L = impregnation-spraying, large sample; Bottom: CF-L = double centrifugation, large sample.

the results in distinct planes (see Figure 3.12). Figure 4.22 presents the mean wall thickness distributions for a RS-S filter (Figure 4.22a) and a CF-S filter (Figure 4.22b). One can notice that the wall thickness distributions are quite similar and homogeneous. This indicates that, in case of *S* filters, both methods were able to provide material to the whole foam in a homogeneous way.

When analyzing the geometric standard deviation (σ) distribution (Figure 4.23), one can observe higher σ values for the RS-S filter. This result is in agreement with the microscopic analysis (Figure 4.19), that showed a higher material concentration at the joints and more tapered struts for the RS filters.

In the case of large filters (L), some important effects were observed for the mean wall thickness distributions (Figure 4.24). Firstly, the scattering of the wall thickness was generally much higher than for S filters. This explains the strength scattering for the large samples presented in Figure 4.16. It is also clear that the RS procedure could not deliver a sufficient amount of material to the inner core region of L filters. There is an evident gradient from the sample's surfaces towards its center. This clarifies the failure features presented by this type of

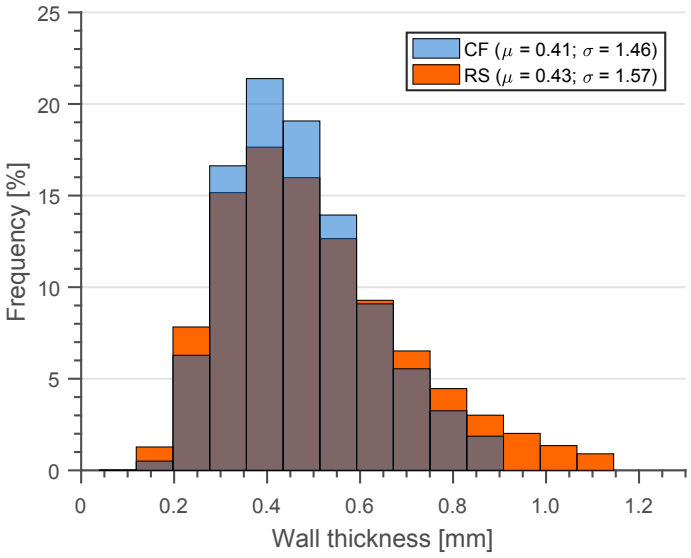

Figure 4.21: Wall thickness distributions for CF-S and RS-S filters: μ = geometric mean value; σ = geometric standard deviation.

filter during the cold crushing strength tests (catastrophic failure always started at the samples' center for RS-L).

The CF-L filters also showed a gradient in the X-Z plane. This can be explained by the variation of centripetal acceleration (function of the distance from the rotational axis) experienced by these filters during centrifugation. This phenomenon was minimized for the S filters, because their height was similar to the distance to the shaft of the centrifugal device. As the L filters presented twice the height of the small ones, this gradient was amplified. When comparing the geometric standard deviation distribution of the RS-L and CF-L filters (Figure 4.25), a correlation with their smaller counterparts can be found. As expected, in general the CF filters showed a lower deviation.

4.3.4 Numerical simulation

To confirm the correlations extracted from the microscopic and CT analyses, the artificially-generated foam geometries were morphologically investigated. As the relative density ρ^*/ρ_s and the k factor were known for each artificial filter, the results of this assessment would confirm that a higher geometric standard deviation is associated to a higher material concentration at the joints and, consequently, tapered struts. Therefore, the 20 geometries obtained by the combination of ρ^*/ρ_s = [0.09; 0.10; 0.11 and 0.12] and k = [0.7; 0.8; 0.9; 1.0 and 1.1] were analyzed. In this case, the region of interest corresponded to the whole virtual sample.

Figure 4.26 presents the geometric standard deviation surface obtained by the linear interpolation of the 20 points investigated. As expected, σ clearly increased with the k parameter for any given relative density. On the other hand, the value of relative density (for the investigated range) had no obvious influence on σ. This results validates the assumption of the standard deviation being directly related to the k factor.

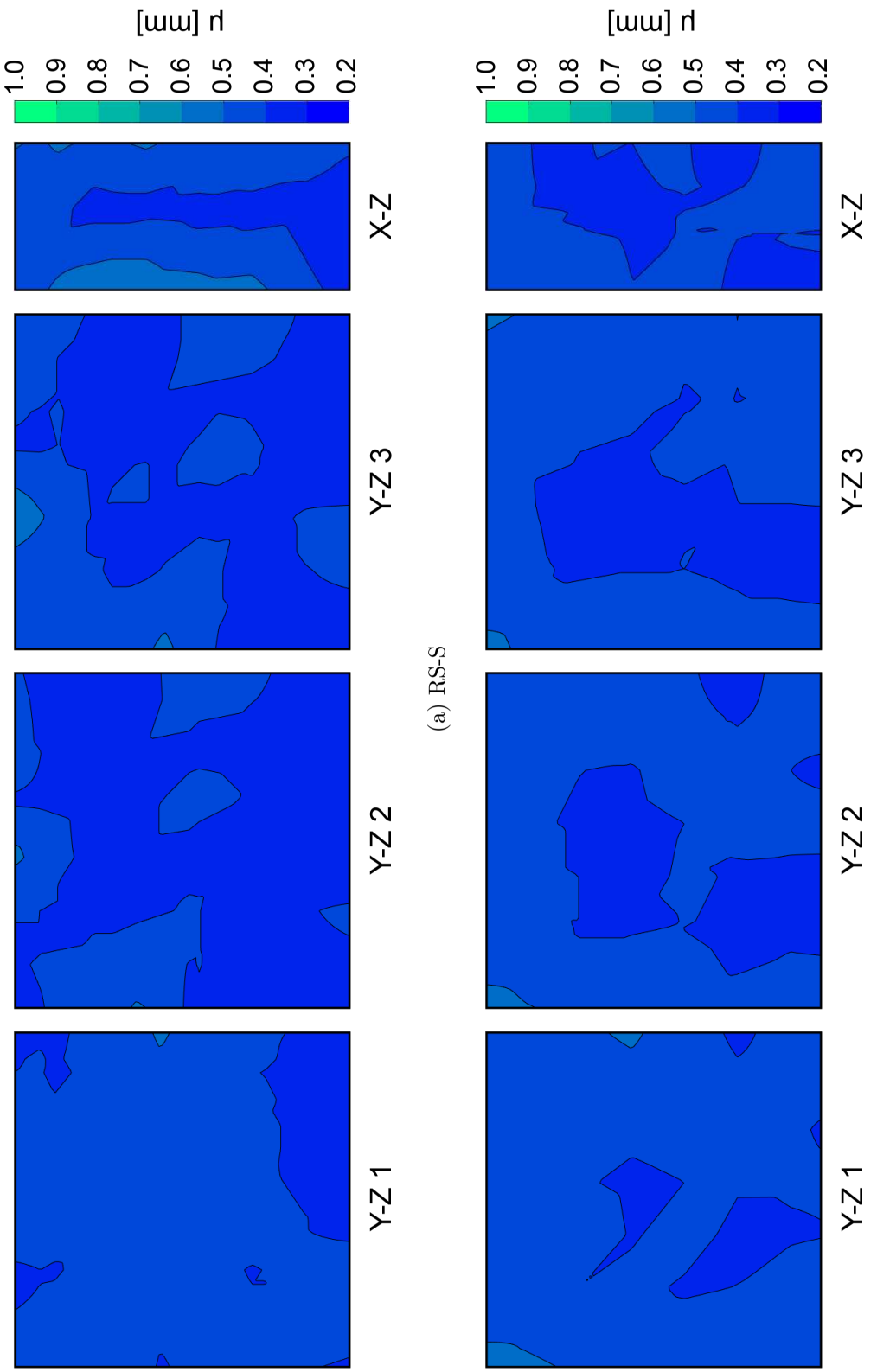

Figure 4.22: Mean wall thickness distributions of the RS-S (a) and CF-S (b) filters at distinct planes.

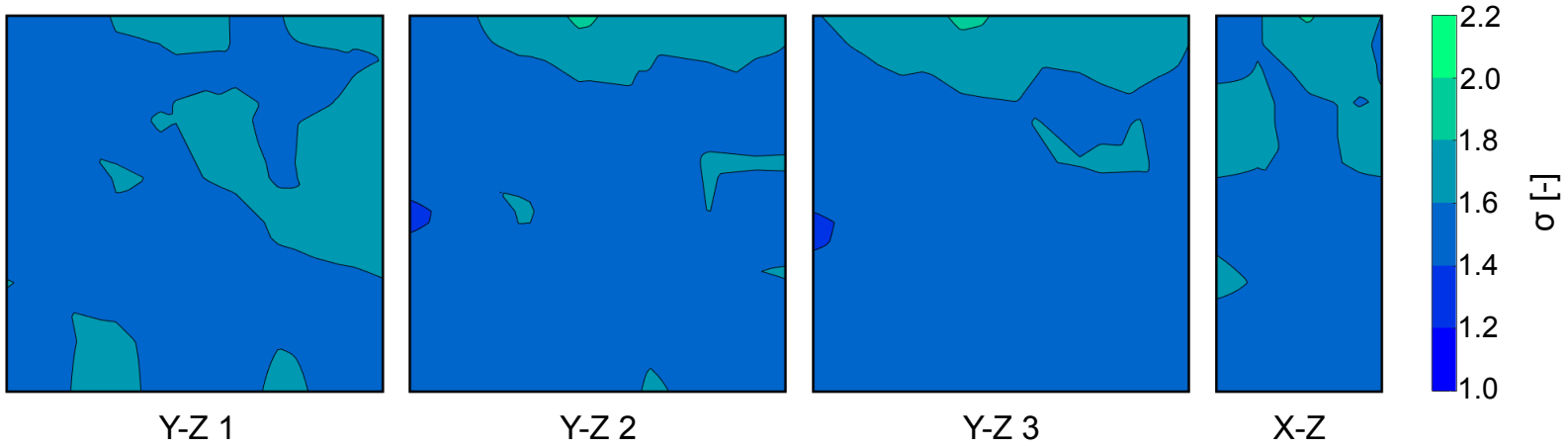

(a) RS-S

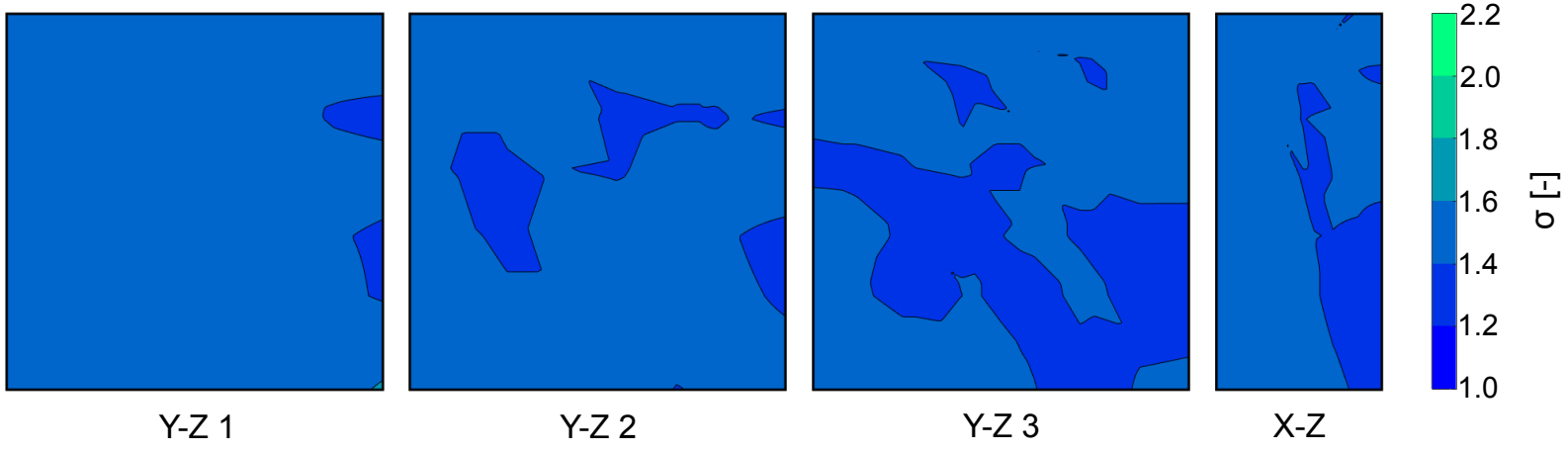

(b) CF-S

Figure 4.23: Geometric wall thickness standard deviation distribution of the RS-S (a) and CF-S (b) filters at distinct planes.

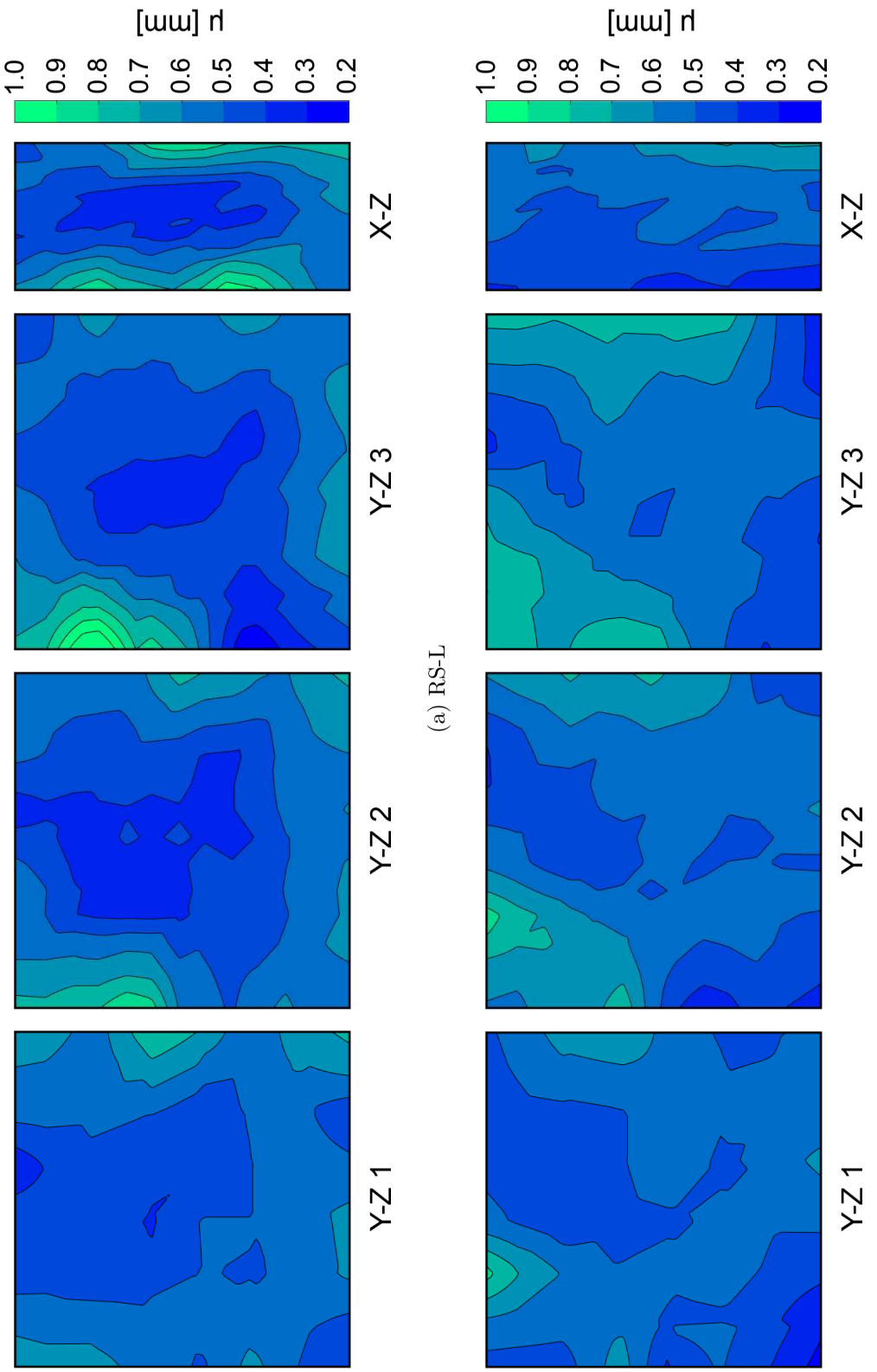

Figure 4.24: Mean wall thickness distributions of the RS-L (a) and CF-L (b) filters at distinct planes.

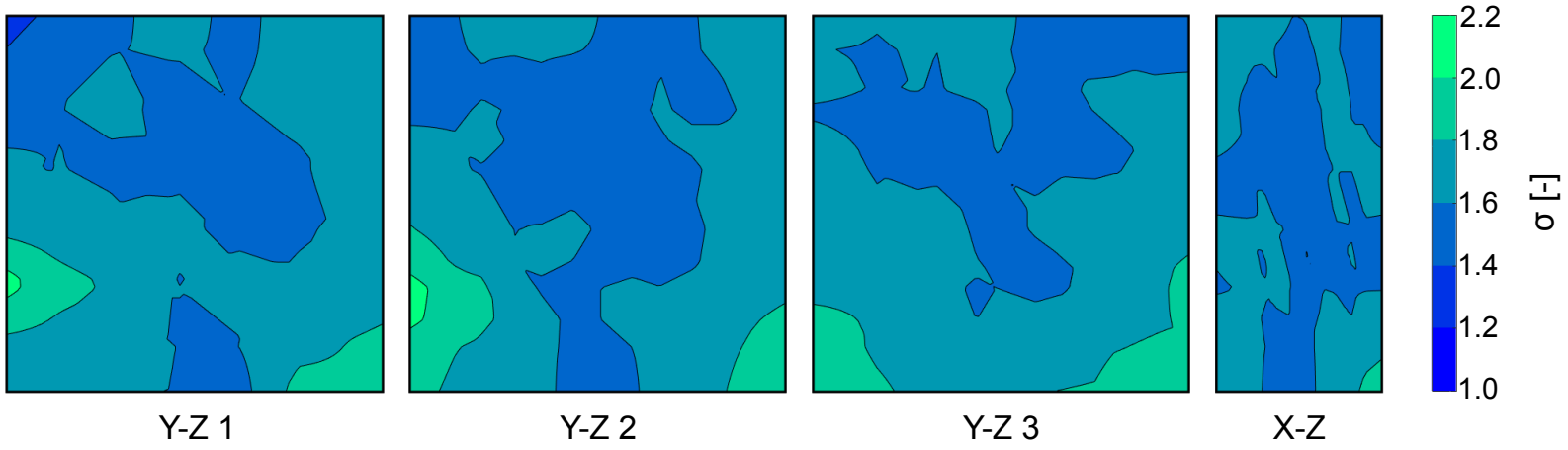

(a) RS-L

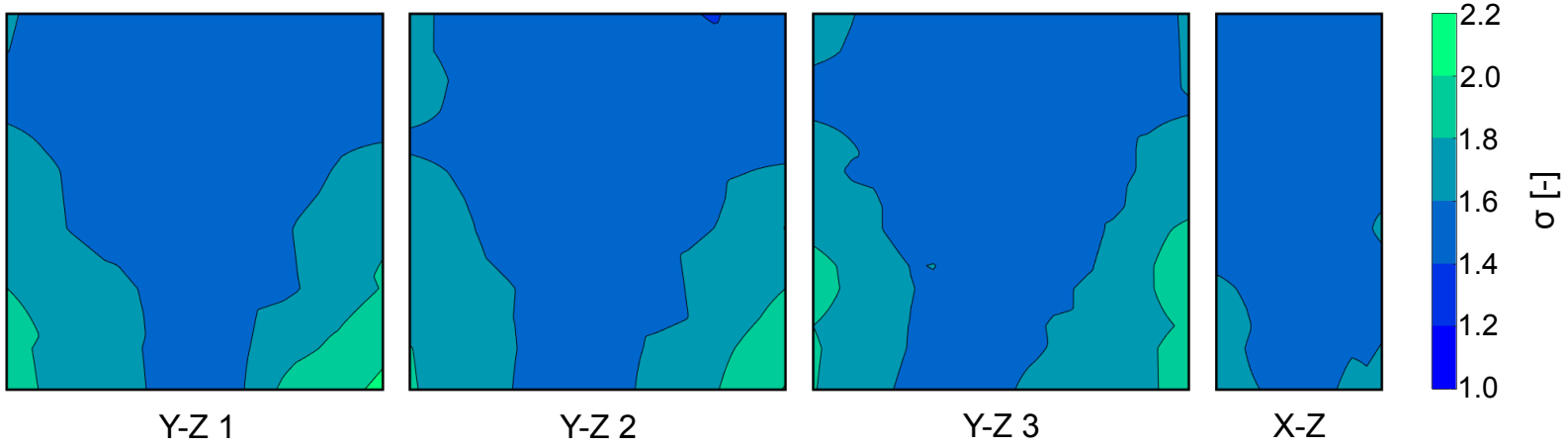

(b) CF-L

Figure 4.25: Geometric wall thickness standard deviation distribution of the RS-L (a) and CF-L (b) filters at distinct planes.

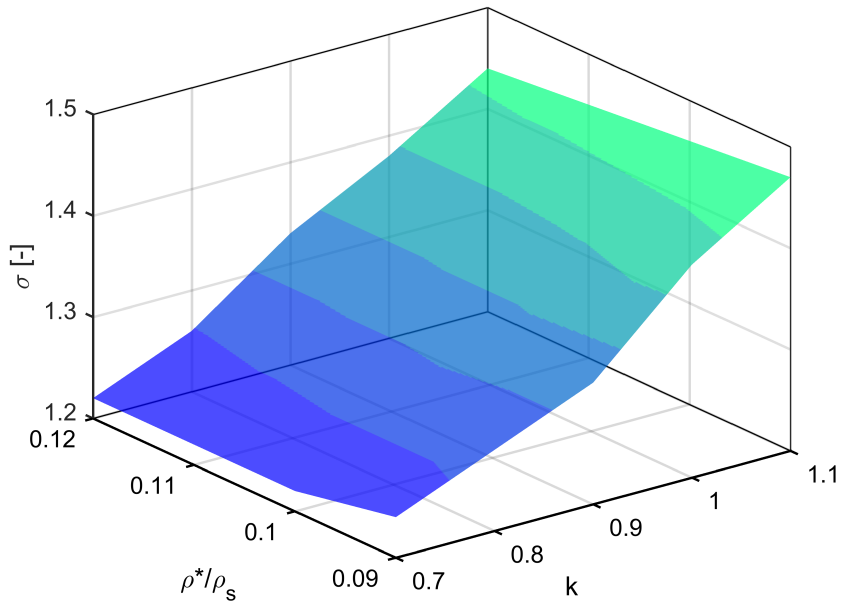

Figure 4.26: Geometric standard deviation surface as function of relative density (ρ^*/ρ_s) and strut tapering factor (k) of the artificially-generated foam geometries.

From the finite element analyses it was possible to compare the distinct filter geometries and a strength parameter was introduced ($\bar{\sigma}_{11}/\sigma_s$). This parameter was extracted by taking into account the maximum global reaction force attained by the structure before the failure, divided by the filter's theoretical cross-sectional area (similar to σ^*/σ_s from the previous sections). Figure 4.27 illustrates the stress distribution within a foam filter structure after the virtual compression test.

By analyzing 16 highly porous structures based on the combination of ρ^*/ρ_s = [0.09; 0.10; 0.11 and 0.12] and k = [0.7; 0.8; 0.9 and 1.0], it was possible to obtain a response surface for the virtual crushing strength as a function of the relative density and strut shape factor (Figure 4.28). As it can be seen, the crushing strength surface presented a tilted concave shape in the range of relative density and k factor analyzed. This highlights that both ρ^*/ρ_s and k factors remarkably affect the crushing strength.

The highest virtual crushing strength was obtained for the filter presenting $\rho^*/\rho_s = 0.12$ and $k = 0.8$. The strength decrease for samples with k lower or higher than 0.8 (regardless of the relative density) indicates that two distinct mechanisms are responsible for the global failure of the filters. To confirm this assumption, the stress distribution of a single strut was analyzed for two filters presenting 11% relative density and k factors of 0.7 and 1.0 (Figure 4.29).

It was observed that the k factor influences the stress distribution in the filter structure. When k is small (lower than 0.8), the most stressed region is located at the joints. It can be assumed that the lower concentration of ceramic material at the joints, associated with the stress concentration due to the hollow struts, are leading the filter's global behavior and inducing the failure during the compression test. On the other hand, for high k values (larger

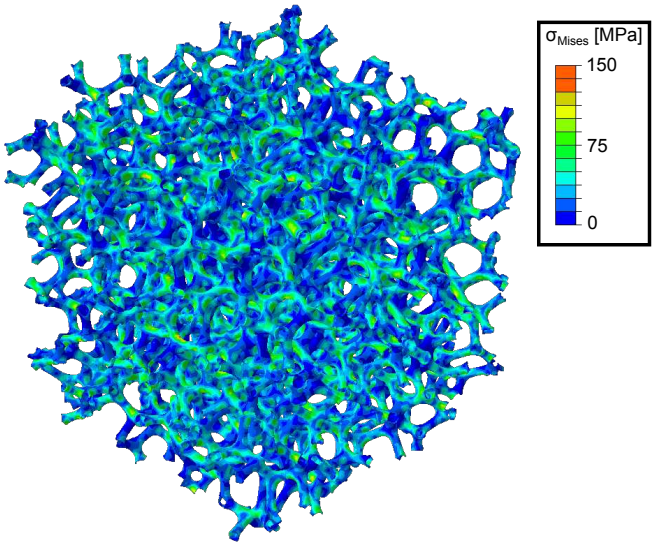

Figure 4.27: Stress state (von Mises) of a sample with k=0.8 and ρ^*/ρ_s=0.1 after the virtual compression test.

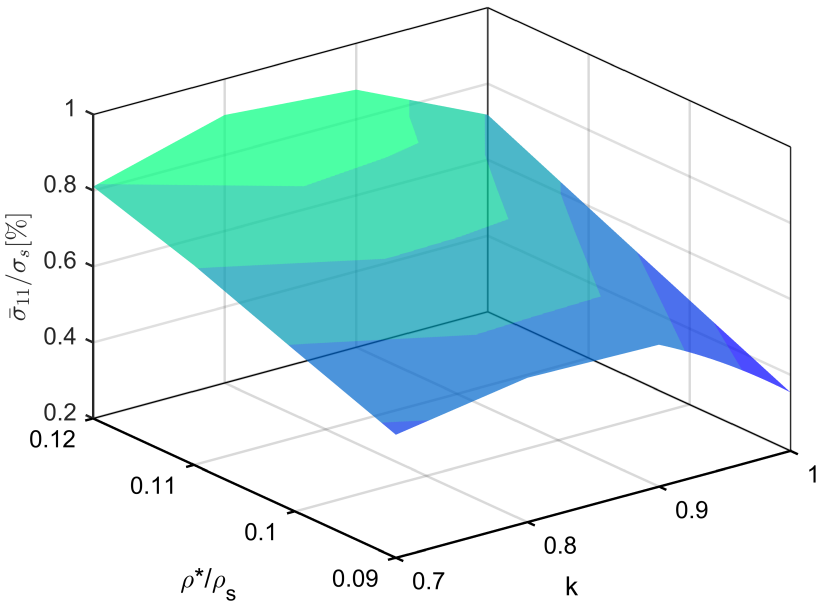

Figure 4.28: Virtual crushing strength surface as function of relative density (ρ^*/ρ_s) and material concentration factor (k).

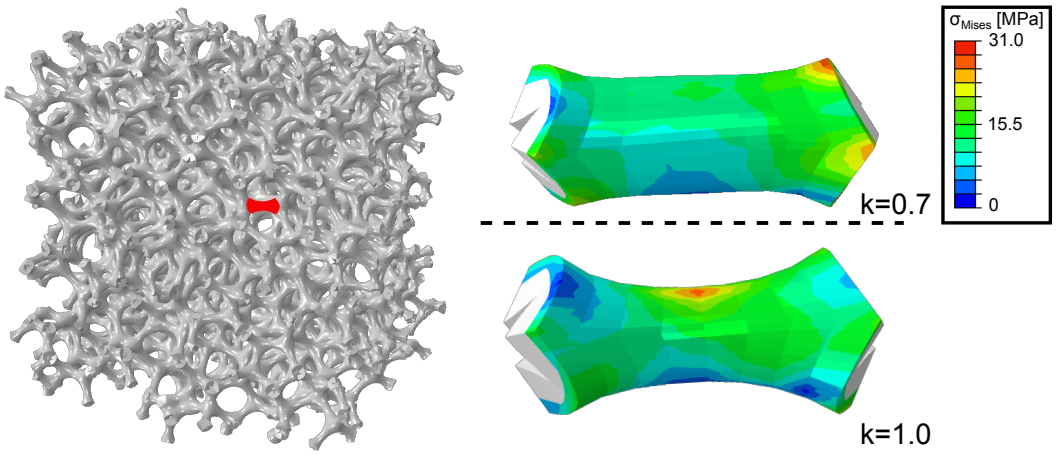

Figure 4.29: Stress distribution in a single strut from two distinct filters presenting 0.11 relative density and $k = 0.7$ and 1.0, respectively.

than 0.8), the tapered geometry of the struts shifts the maximum stress location to the middle part of the struts. Therefore, a different failure mechanism dominates the global behavior.

According to the failure model proposed by Kim and Al-Hassani [45], highly tapered struts subjected to multiaxial stresses are more susceptible to collapse by a combination of bending and normal stresses. As the Gibson and Ashby [26] equations were derived for an ideal cell morphology (see Figure 2.5) not considering tapering, their failure criterion is only taking bending stresses into account (see Equation 2.7). Therefore, most probably the second failure mechanism related to the struts tapering is associated to normal stresses contribution.

To confirm the assumption that this stress shift was related to the contribution of normal stresses in the struts, Figure 4.30 was plotted by combining the results of the finite element simulations, with three distinct fitting curves. As reference, the Gibson-Ashby failure equation for brittle foams was considered ($\bar{\sigma}_{11}/\sigma_s = c \cdot (\rho^*/\rho_s)^{3/2}$). In addition, the Gibson-Ashby equation for stretch-dominated geometries was also analyzed ($\bar{\sigma}_{11}/\sigma_s = d \cdot (\rho^*/\rho_s)$), as for this kind of geometry, struts are subjected only to tensile or compressive stresses. Finally, a fitting model combining both mechanisms (bending-dominated and stretch-dominated equations) was also introduced ($\bar{\sigma}_{11}/\sigma_s = e \cdot (\rho^*/\rho_s) + f \cdot (\rho^*/\rho_s)^{3/2}$) as an alternative to consider the normal stresses contribution into the bending-dominated failure equation from Gibson and Ashby. The fitting curves were calculated with the MATLAB software based on a non-linear regression method. The geometries with $k = 0.7$ and $k = 0.8$ were almost perfectly fitted by the Gibson-Ashby equation. The filters with $k = 0.9$ presented a certain discrepancy, while the filters with $k = 1.0$ were not following the pure bending failure mode proposed by Gibson and Ashby. None of the geometries behaved like stretch-based structures (as expected). On the other hand, the model combining bending and normal stresses could fit the FEM results of all analyzed filters. It must be highlighted that, in general, models with higher order can more easily fit complex curves. Although the proposed model was based on bending-dominated and stretch-dominated equations from Gibson and Ashby [26] as an alternative to include the contribution of normal stresses in highly tapered struts.

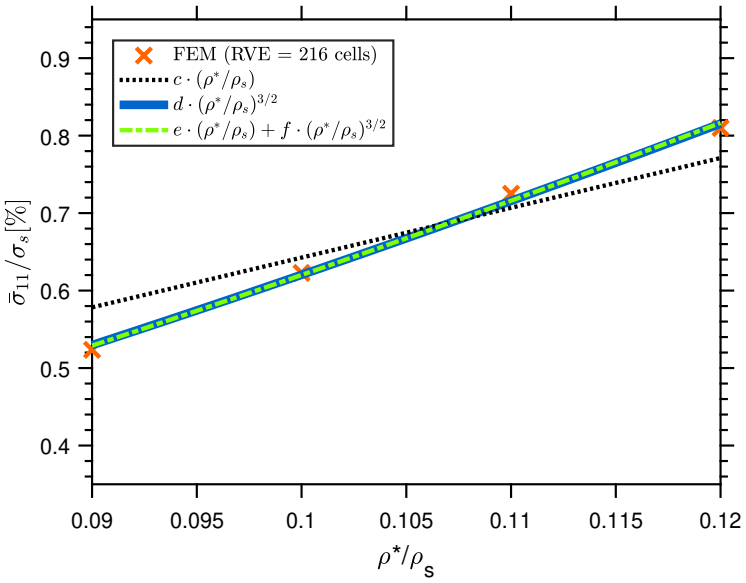

(a) $k = 0.7$

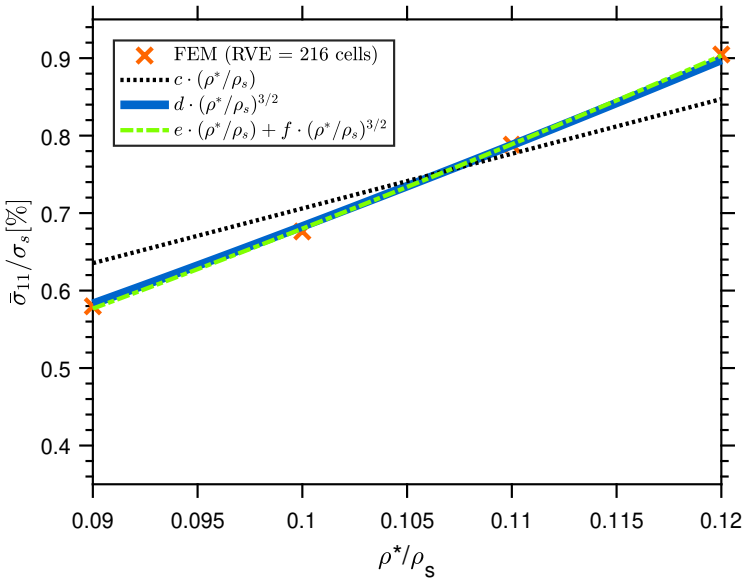

(b) $k = 0.8$

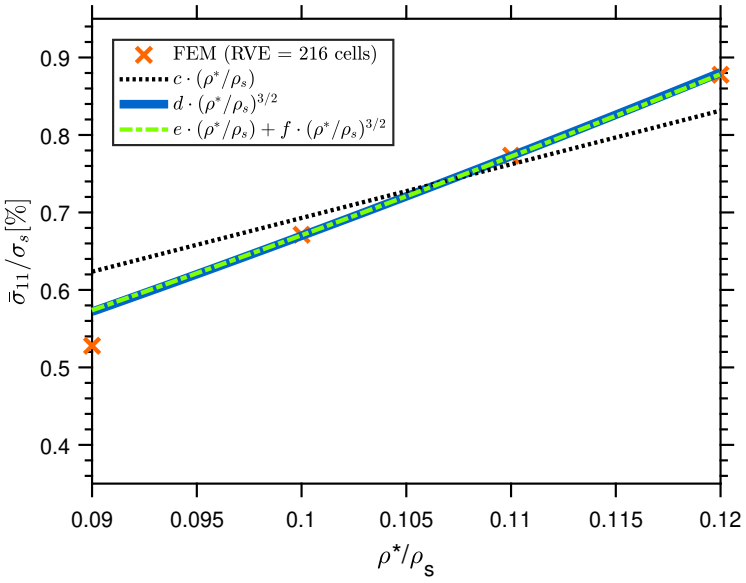

(c) $k = 0.9$

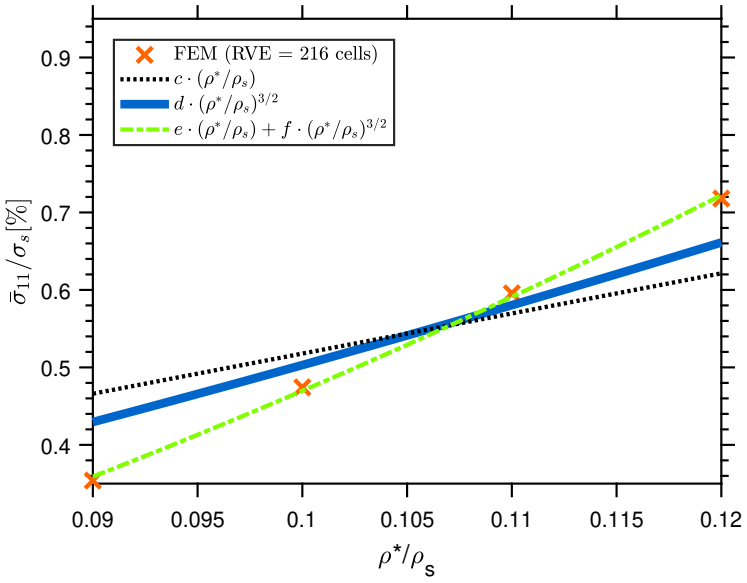

(d) $k = 1.0$

Figure 4.30: Results of virtual compression simulations of artificially-generated geometries.

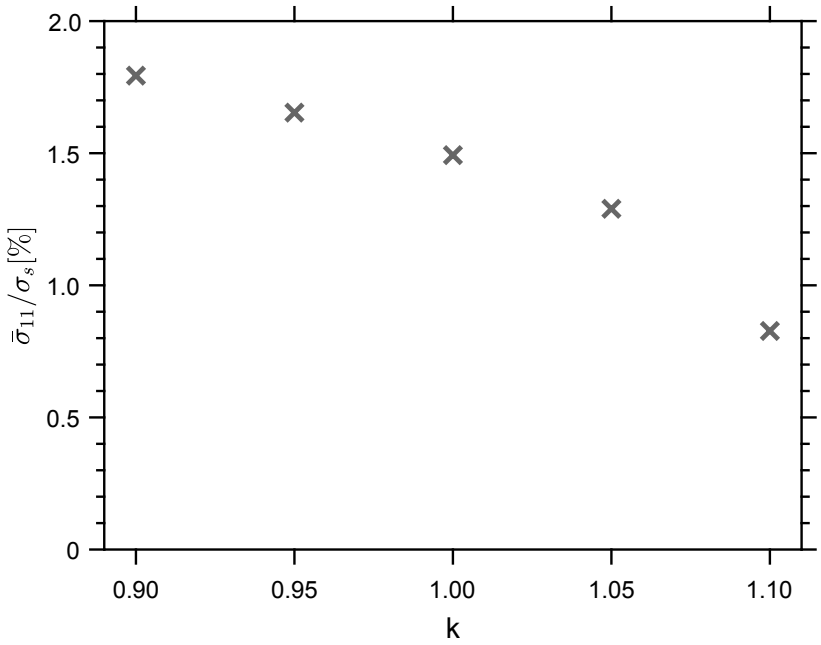

Figure 4.31: Virtual crushing strength as function of tapering factor k (ρ^*/ρ_s was kept constant at 0.2).

This result was not reported by D'Angelo *et al.* [158]. In their finite element analyses, the most stressed region was always located at the strut's nodes. This difference must be related to the simplifying assumptions of the distinct simulation approaches, as well as to a limited tapering range. They considered a foam geometry formed by the stacking of tetrakaidecahedrons and assumed a representative volume element (RVE) containing 16 struts. In the present case, the foam geometry was obtained in a more complex way (see Section 3.3.4), and a RVE containing 216 cells was considered.

In order to expand the relative density range and analyze a broader geometry spectrum, 5 artificially-generated filters with $\rho^*/\rho_s = 0.20$ were simulated. Figure 4.31 shows the non-linear behavior of the virtual crushing strength as a function of the k factor (all filters presented ρ^*/ρ_s = 0.2).

4.3.5 Discussion

Considering all results based on the mechanical tests at room temperature, microscopic and CT analyses, as well as numerical simulations, it was possible to correlate the filters' processing routes with their respective cold crushing strength.

It can be stated that the processing route, which indicated a strength increase for CF samples compared to RS samples, was clearly related to the distinct strut shape factor (k factor) and homogeneity of the filters. Considering the data obtained from the CT analysis, one can assume that the spraying technique was not able to deliver struts with narrow wall thickness distribution within the whole samples. Instead, the struts in the inner core of the RS filters

received less slurry compared to those at the filter's surface (Fig. 4.24). In contrast, the wall thickness during centrifugation was determined by the slurry rheological properties, the angular speed and the distance from the rotational axis. Therefore, a more homogeneous distribution was obtained for S filters, whereas the other samples presented a gradient in the X-Z plane.

The positive effect of increased sample size on the strength should be related to a better redistribution of stresses during the crushing test. As already explained, the sensitivity of single strut failure on the global behavior is much more pronounced for small filters than for the larger ones. As small filters present a significant lower amount of struts, when one of them is broken the stress redistribution can overload the neighbouring struts more likely, leading to a fast catastrophic global failure. It is expected, however, that the up-scaling effect will be counteracted by large defects after reaching a certain filter size. From Weibull theory [178] it is known that higher volumes are associated to a greater likelihood of the sample presenting critical defects. Therefore, a decrease on mechanical strength would be expected.

Furthermore, a significant interaction between the size and the processing route was observed. Thereby, the mechanical strength increase for switching from RS to the CF method was more pronounced for large samples (see Figure 4.16). An explanation for this phenomenon is a different up-scaling sensitivity of the two procedures. For centrifuging, the up-scaling had no remarkable effect on the overall processing conditions, as the setup and the slurry flow parameters remained similar. In the case of spraying, however, the inhomogeneity originating from insufficient coating of the filter center was clearly increased by doubling the filter dimensions, as mentioned above. Consequently, the positive size effect was partially nullified for RS filters in contrast to CF ones.

The high scattering of crushing strength values observed for the CF-L samples highlights that this procedure is still open for improvements. The introduction of a planetary centrifugation device, for instance, would likely reduce the mean wall thickness gradient found in this kind of samples, further improving their material distribution.

Combining numerical simulation with physical and mechanical characterization allowed a deeper comprehension of ceramic foams crushing behavior. It was shown the significant influence of the k factor on the filter's strength. Concluding that for highly tapered struts subjected to compression, the combination of the traditional Gibson-Ashby bending failure criterion with their stretch-dominated equation better represents the foams' behavior.

It is expected that the same behavior measured at room temperature can be extrapolated for carbon-bonded alumina at high temperature applications. Naturally, with different constant values, but following the same tendency. This can be justified by the formulation themselves. As explained in Section 2.2.2, Gibson and Ashby [26] derived the bending-dominated brittle failure criterion based on full section plastic deformation of ductile material beams. Therefore, following the work by Solarek *et al.* [141], that showed evidence of ductile behavior of carbon-bonded alumina foam filters at high temperatures, the Gibson and Ashby bending-dominated equation or even the Gibson and Ashby modified equation proposed in this thesis would be still valid.

5 Summary and Conclusions

This thesis reports the investigation of how the processing routes of carbon-bonded samples (bulk and cellular) interact with their mechanical and thermo-mechanical properties.

In the carbon-bonded bulk study, the effect of the volatiles release on the thermo-mechanical properties of carbon-bonded alumina was analyzed. In order to understand this complex phenomenon, effective Young's modulus, thermogravimetry and porosity measurements were conducted. A finite element model, using the concept of model materials and virtual samples, was developed to validate the assumptions made during the experimental analysis, i.e., the non-linear Young's modulus behavior being directly related to the thermal expansion mismatch between phases.

Results achieved with the computer simulation considering the closure of gaps due to a thermal expansion mismatch among distinct phases during heating were in good agreement with the experiments, which point out that this closure was the primary cause for the increase of the effective Young's modulus during heating. Through the experimental results, it was highlighted that most of the porosity was developed during the volatiles release and the gaps formation due to the thermal expansion mismatch between the particles (alumina and graphite) and the carbon matrix. The particle's expansion rules the global behavior by closing the open porosity formed owing to the volatiles release during firing. Throughout the cooling process, alumina and graphite shrink more than the carbon matrix due to their higher thermal expansion coefficient. Consequently, gaps and cracks are formed. It can be concluded that, in this case, the volatiles release and the thermal expansion mismatch among the phases dominate the composite's non-linear behavior of the Young's modulus at high temperatures.

It can be stated that the gaps between the matrix and particles as well as the crack network give flexibility to the material and act as a damper for the in-situ thermal stress generation. Since the particles (alumina and graphite) have space to deform before stressing the surrounding matrix, the stresses generated are much lower than a completely dense composite (one of the reasons for the high thermal shock resistance).

Inspired by the good results of this investigation, the characterization of carbon-bonded alumina foam filters produced by distinct techniques was carried out. An alternative route for producing carbon-bonded alumina filters was analyzed and compared to the state-of-the-art one. The former is based on dip coating and centrifugation methods (*CF-T1*), whereas the latter on dip coating, rolling and spraying (*RS*). Also a modified centrifugation route was investigated (*CF-T2*), submitting the filters to an extra thermal treatment up to 300 °C in between the two coating steps. This approach was intended to assess the influence of the thermal treatment on the ceramic material surface distribution.

The main aim of this investigation was to compare the filters homogeneities after the different processing routes above mentioned. CT was used at various stages of the filter production, providing a better critical analysis regarding their benefits and drawbacks.

It was found out that the wall thickness values for the filters produced by the three routes

were well fitted by log-normal functions. Besides that, the CT analysis allowed to assess the filter volume and linear shrinkages after firing.

The experiments pointed out that the *RS* volume shrinkage was 7.7 %, whereas the *CF-T1* and the *CF-T2* were 9.1 % and 1.4 %, respectively. The difference between the *RS* and *CF-T1* is related to a lower solid content in the centrifugation slurry, if compared to the spraying one. The *CF-T2* procedure showed the lowest shrinkage because of the additional thermal treatment for this processing route. As the *CF-T2* filters were thermally treated before the final firing, the shrinkage experienced during firing was reduced, increasing the filter dimensional stability.

The local shrinkage calculated is related to the radial direction of the struts. In that case, the values were 10.0 %, 13.8 % and 6.1 % for *RS*, *CF-T1* and *CF-T2*, respectively. The same trend observed for the volume shrinkage was found for the local one. The linear shrinkage was higher than the volume one because while the latter presents an effective measurement, being influenced by the filter geometry and porosity, the linear shrinkage is only related to the struts material (radial direction).

Based on the normalized difference between the local and global wall thicknesses means for each filter, it was possible to compare their homogeneity. It can be concluded that *CF* filters presented a more homogeneous distribution (variability within 0 and 5 %) when compared to the *RS* ones (variability within 10 % and 15 %). This is due to the higher automation level for the *CF* route, being less dependent on the lab operator and after the upscailing study it was also possible to conclude that the shear rate associated to the processing route has a significant influence on the wall thickness homogeneity.

Microscopic analysis highlighted that *RS* filters have a relatively smoother surface and present macro-cracks associated to the PU burnout. *CF-T1* filters presented a rougher surface as well as macrocracks associated to the PU gas release. The surface of *CF-T2* filters was also rough, but almost no macrocracks could be found on the struts. Only, a significant number of micro-cracks were present on the filters surface. This effect is very likely related to the additional thermal treatment of this processing route.

Cold crushing tests showed that *RS* and *CF-T1* filters presented similar strength, but distinct fracture behavior. While the *RS* filter exhibited a locally brittle response (with sharp drops in the force associated to the single or few struts breaking) the *CF-T1* presented a much smoother curve, as a consequence of more homogeneously material distribution. The *CF-T2*, on it's turn, showed the lowest strength, mainly motivated by the high amount of surface microcracks associated to the additional thermal treatment.

Therefore, for the continuation of the study, only the *RS* and *CF-T1* processing routes were chosen for the up-scaling analysis. The influence of the processing route and sample dimensions on the mechanical properties of carbon-bonded alumina foam filters was investigated. The same slurries were used for both processing routes and the filter samples were thermally treated under the same conditions. The following conclusions could be drawn:

(i) Filters prepared by double-step centrifugation showed the highest cold crushing strength and very smooth force-displacement profiles; (ii) Centrifugation delivered foams with higher homogeneity of strut wall thickness (lower geometric standard deviation); (iii) Due to the inherent features of spray coating, a higher inhomogeneity of the material distribution was achieved by upscaling; (iv) Morphological investigations of the artificially-generated foam structures via computer tomography (for relative density in the range 0.09-0.12) pointed out that the strut tapering factor k is correlated to the geometric standard deviation obtained from the wall

thickness distribution analysis; (v) For the same range of relative density, the virtual crushing strength of foams showed a maximum value at $k = 0.8$; (vi) A good correlation between the real and virtual strength was obtained, highlighting that the higher CCS of filters produced by centrifugation is related to lower tapering factors k a comparable relative density; (vii) Two distinct failure mechanisms were detected for filters subject to cold crushing tests. For lower k factors, the joints represent the most likely location for crack initiation, being the most stressed regions. For strut shape factor higher than 0.8, the most stressed region shifts to the struts' middle part, changing the failure behavior. This change is due to the contribution of normal stresses to the failure of highly tapered struts, while non or slightly tapered struts fail mostly by bending; (viii) Double-step centrifugation proved to be a more suitable method to produce ceramic foam filters compared to the impregnation-spraying one, especially for large sizes. The former allows to use less material while keeping good mechanical properties, as the material distribution is more homogeneous.

6 Outlook

The findings of this thesis can be considered a starting point to further improvements on the processing route and consequent thermo-mechanical properties of carbon-bonded refractories. Hereafter, some open topics are listed for future investigations:

- **Young's modulus investigation of carbon-bonded bulk materials at different heating cycles:** As described in the thesis, only two heating cycles were used to characterize the Young's modulus behavior of carbon-bonded alumina. However, for a full characterization of the material behavior during the in-service conditions, distinct heating schedules must be assessed. Therefore, a complete model material also including the creep effects of the carbon matrix at high temperatures should be investigated;

- **Further characterization of open-cell porous ceramics via computed tomography including additive manufacturing technologies:** One of the original findings of this thesis resulted from the use of CT at several steps of the manufacturing process of carbon-bonded alumina filters. As this was a completely new task, some assumptions were made to enable the analyses of such complex structures. Combining modelling with the morphological analysis, it was possible to correlate the geometric standard deviation (σ) from the filter's wall thickness distribution with the strut tapering factor (k) of artificial geometries. For a more complete correlation, it would be appropriate 3D printing the artificially generated foams and then characterizing it via CT. Some works in this direction were already conducted in the CRC 920, see [27], but not focusing on the tapering characterization.

- **Further studies on processing up-scaling:** Finally, the continuation of the up-scaling analysis could be carried out including larger samples and different processing routes. Therefore, a study about the scale factor from different processing routes on the cold crushing strength would be assessed. The possibility of analyzing such large filters at high temperatures would allow the extension of the results to in-service conditions.

Bibliography

[1] V., Roungos: *Development of a self-glazing carbon bonded alumina refractory and its potential as monoblock stopper for steel casting applications.* Ph.D. thesis, Fakultät für Maschinenbau Verfahrens- und Energietechnik der Technischen Universität Bergakademie Freiberg, 2017.

[2] Kreuels, N.: *A view on the European Refractory Industry.* Boletín de la Sociedad Española de Cerámica y Vidrio **48**(2009):245–254.

[3] Roungos, V. and Aneziris, C.G.: *Improved thermal shock performance of $Al_2O_3 - C$ refractories due to nanoscaled additives.* Ceramics International **38**(2012):919–927.

[4] Luchini, B.; Grabenhorst, J.; Fruhstorfer, J.; Pandolfelli, V.C. and Aneziris, C.G.: *On the nonlinear behavior of Young's modulus of carbon-bonded alumina at high temperatures.* Journal of the American Ceramic Society **00**(2018):1–13.

[5] Resende, W.S.; Stoll, R.M.; Justus, S.M.; Andrade, R.M.; Longo, E.; Baldo, J.B.; Leite, E.R.; Paskocimas, C.A.; Soledade, L.E.B. and Gomes, J.E.: *Key features of alumina/-magnesia/graphite refractories for steel ladle lining.* Journal of the European Ceramic Society **20**(2000):1419–1427.

[6] Quintela, M.A.; de Melo, T.M.F.; Lage, I.J.; Pandolfelli, V.C. and Rodrigues, J.A.: *Evaluation of the thermal shock resistance of carbon-containing refractories (in Portuguese).* Cerâmica **47**(2001):174–179.

[7] Aneziris, C.G.; Hubálková, J. and Barabas, R.: *Microstructure evaluation of MgO–C refractories with TiO_2- and Al-additions.* Journal of the European Ceramic Society **27**(2007):73–78.

[8] Vesuvius: *VISO Tundish Stopper.* Marketing Brochure, 1 2015.

[9] Mayerton: *Mayerton Refractories Ltd.* Refractories Worldforum, 3 2012.

[10] Stein, V. and Aneziris, C.G.: *Low-carbon carbon-bonded alumina refractories for functional components in steel technology.* Journal of Ceramic Science and Technology **5**(2014):115–123.

[11] Brachhold, N.; Fruhstorfer, J.; Mertke, A. and Aneziris, C.G.: *Carbon-Bonded Alumina Refractories with Reduced Carbon Content due to the Addition of Semi-Conductive Silicon and/or Nanoparticles.* Journal of Ceramic Science and Technology **7**(2016):209–222.

[12] Pieprzyca, J.; Merder, T.; Warzecha, M. and Skorupa, J.: *The influence of steel preheating level in the tundish on the primary structure of a continuously cast ingot.* Metalurgija **54**(2015):127–130.

[13] Auer, T.; Gruber, D.; Harmuth, H. and Lueftenegger, A.: *Numerical failure analysis for the refractory lining of a tundish.* In *49th International Colloquium on Refractories, Aachen, Germany.* 2006.

[14] Mertke, A. and Aneziris, C.G.: *The influence of nanoparticles and functional metallic additions on the thermal shock resistance of carbon bonded alumina refractories.* Ceramics International **41**(2015):1541–1552.

[15] Zhang, S.W.: *Next generation carbon-containing refractory composites.* Advances in Science and Technology **45**(2006):2246–2253.

[16] Jahn, C.; Gerlach, N.; Weber, A.; Moritz, K. and Aneziris, C.G.: *Investigation on Pressure Slip Casting of Carbon Bonded Alumina.* Interceram-International Ceramic Review **67**(2018):22–29.

[17] Bitencourt, C.S.: *Resin-bonded refractories: fundamentals, critical analysis and the effect of the graphitizing agents and antioxidants (in Portuguese).* Ph.D. thesis, Federal University of Sao Carlos, 2001.

[18] de Oliveira, I.R.; Studart, A.R. and Pandolfelli, V.C.: *Review article: stabilization of graphite-containing aqueous suspensions (in Portuguese).* Cerâmica **46**(2000):186–195.

[19] Ewais, E.M.M.: *Carbon based refractories.* Journal of Ceramic Society of Japan **112**(2004):512–532.

[20] Aneziris, C.G.; Klippel, U.; Schaerfl, W. and Stein, V.: *Functional refractory material design for advanced thermal shock performance due to titania additions.* International Journal of Applied Ceramic Technology **4**(2007):481–489.

[21] Lee, W.E. and Zhang, S.: *Melt corrosion of oxide and oxide–carbon refractories.* International Materials Reviews **44**(1999):77–104.

[22] Rodrigues, J.A. and Pandolfelli, V.C.: *R-curve behavior of MgO-C refractories (in Portuguese).* Ceramica **46**(2001):40 – 47.

[23] Leite, F.C; Luz, A.P. and Pandolfelli, V.C.: *Characteristics and wearing mechanisms of MgO-C refractories for steel ladle slag line.* Ceramica **60**(2014):348–365.

[24] Buffel, B.; Desplentere, F.; Brack, K. and Verpoest, I.: *Modelling open cell-foams based on the Weaire-Phelan unit cell with a minimal surface energy approach.* International Journal of Solid and Structures **51**(2014):3461–3470.

[25] Ashby, M.F.: *The properties of foams and lattices.* Philosophical Transactions of the Royal Society A: Mathematical, Physical and Engineering Sciences **364**(2005):15–30.

[26] Gibson, L.J. and Ashby, M.F.: *Cellular Solids: Structure and Properties*, chapter 5, pages 176–183. Cambridge University Press, 2 edition, 1999.

[27] Herdering, A.; Abendroth, M.; Gehre, P.; Hubálková, J. and Aneziris, C.G.: *Additive manufactured polyamide foams with periodic grid as templates for the production of functional coated carbon-bonded alumina foam filters.* Ceramics International **45**(2019):153–159.

[28] Wetzig, T.; Luchini, B.; Dudczig, S.; Hubálková, J. and Aneziris, C.G.: *Development and testing of carbon-bonded alumina foam filters for continuous casting of steel.* Ceramics International **44**(2018):18143 – 18155.

[29] Wetzig, T.; Baaske, A.; Karrasch, S.; Brachhold, N.; Rudolph, M. and Aneziris, C.G.: *Application of exchangeable carbon-bonded alumina foam filters in an industrial tundish for the continuous casting of steel.* Ceramics International **44**(2018):23024–23034.

[30] Himcinschi, C.; Biermann, C.; Storti, E.; Dietrich, B.; Wolf, G.; Kortus, J. and Aneziris, C.G.: *Innovative carbon-bonded filters based on a new environmental-friendly binder system for steel melt filtration.* Journal of the European Ceramic Society **38**(2018):5580–5589.

[31] Bock, B.; Schmidt, A.; Sniezek, E.; Dudczig, S.; Schmidt, G.; Szczerba, J. and Aneziris, C.G.: *Impact of spinel forming systems (Fe-/Mg-/Mn-Al-O) as functional coating materials for carbon-bonded alumina filters on steel melt filtration.* Ceramics International **45**(2019):4499–4508.

[32] Schramm, A.; Bock, B.; Schmidt, A.; Zienert, T.; Ditze, A.; Scharf, C. and Aneziris, C.G.: *Interface reactions of differently coated carbon-bonded alumina filters with an AZ91 magnesium alloy melt.* Ceramics International **44**(2018):17415–17424.

[33] Gehre, P.; Schmidt, A.; Dudczig, S.; Hubálková, J.; Aneziris, C.G.; Child, N.; Delaney, I.; Rancoule, G. and DeBastiani, D.: *Interaction of slip-and flame-spray coated carbon-bonded alumina filters with steel melts.* Journal of the American Ceramic Society **101**(2018):3222–3233.

[34] Luchini, B.; Hubálková, J.; Wetzig, T.; Grabenhorst, J.; Fruhstorfer, J.; Pandolfelli, V.C and Aneziris, C.G.: *Carbon-bonded alumina foam filters produced by centrifugation: A route towards improved homogeneity.* Ceramics International **44**(2018):13832 – 13840.

[35] Storti, E.; Dudczig, S.; Schmidt, A.; Schmidt, G. and Aneziris, C.G.: *Filter functionalization with carbon nanotubes and alumina nanosheets for advanced steel filtration.* steel research international **88**(2017):1700142.

[36] Emmel, M. and Aneziris, C.G.: *Development of novel carbon bonded filter compositions for steel melt filtration.* Ceramics International **38**(2012):5165–5173.

[37] Emmel, M. and Aneziris, C.G.: *Functionalization of carbon-bonded alumina filters through the application of active oxide coatings for steel melt filtration.* Journal of Materials Research **28**(2013):2234–2242.

[38] Zielke, H.; Schmidt, A.; Abendroth, M.; Kuna, M. and Aneziris, C.G.: *Influence of the Specimen Manufacturing Process on the Strength of Carbon-Bonded Alumina (Al2O3–C).* Advanced Engineering Materials **19**(2017):1700083.

[39] Zielke, H.; Abendroth, M. and Kuna, M.: *Fracture Toughness Characterization of Carbon Bonded Alumina Using Chevron Notched Specimens.* In *Key Engineering Materials*, volume 754, pages 71–74. Trans Tech Publ, 2017.

[40] Zielke, H.; Abendroth, M.; Kuna, M. and Kiefer, B.: *Determining the fracture toughness of ceramic filter materials using the miniaturized chevron-notched beam method at high temperature.* Ceramics International **44**(2018):13986–13993.

[41] Schwartzwalder, K.; Somers, H. and Somers, A.V.: *Method of making porous ceramic articles: U.S Patent, 3090094*, 1963.

[42] Bianchi, G.; Gianella, S.; Ortona, A. and Sa, E.: *Design and additive manufacturing of periodic ceramic architectures.* Journal of Ceramic Science Technology **8**(2017):59–66.

[43] Maxwell, J. C.: *On the calculation of the equilibrium and stiffness of frames.* The London, Edinburgh, and Dublin Philosophical Magazine and Journal of Science **27**(1864):294–299.

[44] Scheffler, M. and Colombo, P.: *Cellular ceramics: structure, manufacturing, properties and applications.* John Wiley & Sons, 2006.

[45] Kim, H.S. and Al-Hassani, S.T.S.: *The effect of doubly tapered strut morphology on the plastic yield surface of cellular materials.* International Journal of Mechanical Sciences **44**(2002):1559–1581.

[46] Triantafillou, T.C.; Zhang, J.; Shercliff, T.L.; Gibson, L.J. and Ashby, M.F.: *Failure surfaces for cellular materials under multiaxial loads—II. Comparison of models with experiment.* International Journal of Mechanical Sciences **31**(1989):665–678.

[47] Settgast, C.; Abendroth, M. and Kuna, M.: *Fracture mechanical analysis of open cell ceramic foams under multi-axial mechanical loading.* Archive of Applied Mechanics **86**(2016):335–349.

[48] Lu, Z.; Huang, J. and Yuan, Z.: *Effects of microstructure on uniaxial strength asymmetry of open-cell foams.* Applied Mathematics and Mechanics **36**(2015):37–46.

[49] Lim, D.; Kim, H.S.; Kim, Y.H.; Kim, Y.H. and Al-Hassani, S.T.S.: *Stress analysis of two-dimensional cellular materials with thick cell struts.* Journal of Mechanical Science and Technology **22**(2008):835.

[50] Storti, E.; Dudczig, S.; Emmel, M.; Colombo, P. and Aneziris, C.G.: *Functional Coatings on Carbon-Bonded Ceramic Foam Filters for Steel Melt Filtration.* Steel Research International **87**(2016):1030–1037.

[51] Xie, L.S. and Chan, K.C.: *The effect of strut geometry on the yielding behaviour of open-cell foams.* International journal of mechanical sciences **48**(2006):249–255.

[52] Settgast, C.; Ranglack-Klemm, Y.; Hubalkova, J.; Abendroth, M.; Kuna, M. and Biermann, H.: *Validation of an experimental-numerical approach for the high temperature behaviour of open-cell ceramic foams.* Journal of the European Ceramic Society **39**(2019):610–617.

[53] Abendroth, M.; Werzner, E.; Settgast, C. and Ray, S.: *An Approach Toward Numerical Investigation of the Mechanical Behavior of Ceramic Foams during Metal Melt Filtration Processes*. Advanced Engineering Materials **19**(2017):1700080.

[54] Jung, A. and Diebels, S.: *Microstructural characterisation and experimental determination of a multiaxial yield surface for open-cell aluminium foams*. Materials & Design **131**(2017):252–264.

[55] Fishler, M.K. and Dale, B.H.: *Carbon Bonded Refractory Bodies: U.S Patent, 4871698*, 1989.

[56] Kernion, M.C. and Renkey, A.L.: *Carbon Bonded Refractories: U.S Patent, 4521357*, 1985.

[57] Michael, D.J.; Kirk, D.A. and Brooks, L.F.: *Magnesite-carbon refractories: U.S Patent, 4912068*, 1988.

[58] Rand, B.; Ahmed, A.S. and Ramos, V.P.S.: *The role of carbon in refractories, Tehran International Conference on Rrefractories*, 2004.

[59] Rand, B. and McEnaney, B.: *Carbon binders from polymeric resins and pitch. I: Pyrolysis behaviour and structure of the carbons*. British ceramic. Transactions and journal **84**(1985):157–165.

[60] McEnaney, B. and Rand, B.: *Carbon binders from polymeric resins and pitch: II, Structure and properties of the carbons*. British Ceramic Transactions and Journal **84**(1985):193–198.

[61] Harris, P.J.F.; Burian, A. and Duber, S.: *High-resolution electron microscopy of a microporous carbon*. Philosophical Magazine Letters **80**(2000):381–386.

[62] Harris, P.J.F.: *New perspectives on the structure of graphitic carbons*. Critical Reviews in Solid State and Materials Sciences **30**(2005):235–253.

[63] Franklin, R.E.: *Crystallite growth in graphitizing and non-graphitizing carbons*. Proc. R. Soc. Lond. A **209**(1951):196–218.

[64] Harris, P.J.F.: *Rosalind Franklin's work on coal, carbon, and graphite*. Interdisciplinary Science Reviews **26**(2001):204–210.

[65] Ban, L.L.; Crawford, D. and Marsh, H.: *Lattice-resolution electron microscopy in structural studies of non-graphitizing carbons from polyvinylidene chloride (PVDC)*. Journal of Applied Crystallography **8**(1975):415–420.

[66] Kroto, H. W.; Heath, J.R.; O'Brien, S.C.; Curl, R.F. and Smalley, R.E.: *C60: Buckminsterfullerene*. Nature **318**(1985):162.

[67] Burian, A. and Dore, J.C: *Does carbon prefer flat or curved surfaces?* Acta Physica Polonica-Series A General Physics **98**(2000):457–468.

[68] Marsh, H. and Rodriguez-Reinoso, F.: *Activated carbon*. Elsevier, 2006.

[69] Appleyard, S.P.; Rand, B. and Ahearn, C.E.: *Processing, Structure and Properties of Pitch-Based Carbon-Carbon Composites*. Preprints of papers - American Chemical Society division fuel chemistry **40**(1995):260–264.

[70] Bitencourt, C.S. and Pandolfelli, V.C.: *Carbon containing refractories: properties, characteristics and variables in their composition*. Cerâmica **59**(2013):84–114.

[71] Yue, C. and Watkinson, A.P.: *Pyrolysis of pitch*. Fuel **77**(1998):695–711.

[72] Marsh, H.; Martinez-Escandell, M. and Rodriguez-Reinoso, F.: *Semicokes from pitch pyrolysis: mechanisms and kinetics*. Carbon **37**(1999):363–390.

[73] Brooks, J.D. and Taylor, G.H.: *The formation of graphitizing carbons from the liquid phase*. Carbon **3**(1965):185–193.

[74] Marsh, H.: *A tribute to Philip L. Walker*. Carbon **29**(1991):703–704.

[75] Mikociak, D.; Magiera, A.; Labojko, G. and Blazewicz, S.: *Effect of nanosilicon carbide on the carbonisation process of coal tar pitch*. Journal of Analytical and Applied Pyrolysis **107**(2014):191–196.

[76] Gubernat, M.; Lis, T.; Tomala, J.; Kawala, J.; Fraczek-Szczypta, A. and Blazewicz, S.: *Study of the carbonization and graphitization of coal tar pitch modified with SiC nanoparticles*. Journal of Nanomaterials **2017**(2017).

[77] Zhang, S. and Lee, W.E.: *Carbon containing castables: current status and future prospects*. British Ceramic Transactions **101**(2002):1–8.

[78] Dolmatov, L.V.; Kutukov, I.E. and Serkovskaya, G.S.: *Petroleum binders and impregnating materials - substitutes for highly toxic coal producs*. Chemistry and Technology of Fuels and Oils **38**(2002):135–137.

[79] Sidorov, O.F.; Deryugin, A.A. and Sidelnikov, A.Y.: *Assessing the carcinogenicity of carbon-bearing binders*. Coke and Chemistry **59**(2017):471–477.

[80] Röder, C.; Weißbach, T.; Himcinschi, C.; Kortus, J.; Dudczig, S. and Aneziris, C.G.: *Raman spectroscopic characterization of novel carbon-bonded filter compositions for steel melt filtration*. Journal of Raman Spectroscopy **45**(2014):128–132.

[81] Fitzer, E.; Mueller, K. and Schaefer, W.: *The chemistry of the pyrolytic conversion of organic compounds to carbon*. Chemistry and physics of carbon **7**(1971):237–383.

[82] Conley, R.T. and Bieron, J.F.: *A study of the oxidative degradation of phenol-formaldehyde polycondensates using infrared spectroscopy*. Journal of Applied Polymer Science **7**(1963):103–117.

[83] Jackson, W.M. and Conley, R.T.: *High temperature oxidative degradation of phenol–formaldehyde polycondensates*. Journal of Applied Polymer Science **8**(1964):2163–2193.

[84] Lenghaus, K.; Qiao, G. GuangHua; Solomon, D.H.; Gomez, C.; Rodriguez-Reinoso, F. and Sepulveda-Escribano, A.: *Controlling carbon microporosity: the structure of carbons obtained from different phenolic resin precursors.* Carbon **40**(2002):743–749.

[85] Kobayashi, K.; Sugawara, S.; Toyoda, S. and Honda, H.: *An X-ray diffraction study of phenol-formaldehyde resin carbons.* Carbon **6**(1968):359–363.

[86] Donald, W. O.: *U.S. Geological Survey, 2015 Minerals Yearbook: Graphite.* USGS, 2015.

[87] Cooper, C.F.: *Graphite-containing refractories.* REFRACT. J. Refract. J. (1980):11.

[88] Chen, X.; Li, Y.; Li, Y.; Sang, S.; Zhao, L.; Li, S.; Jin, S. and Ge, S.: *Effect of carbon aggregates on the properties of carbon refractories for a blast furnace.* Metallurgical and Materials Transactions B **41**(2010):420–429.

[89] Zhao, L. and Sahajwalla, V.: *Interfacial Phenomena during Wetting of Graphite / Alumina.* ISIJ International **43**(2003):1–6.

[90] Warren, B.E.: *X-Ray Diffraction Study of Carbon Black.* The journal of chemical physics **2**(1934):551–555.

[91] Lum, R.; Wilkins, C.W.; Robbins, M.; Lyons, A.M. and Jones, R.P.: *Thermal analysis of graphite and carbon-phenolic composites by pyrolysis-mass spectrometry.* Carbon **21**(1983):111–116.

[92] Bahtli, T.; Bostanci, V. M.; Hopa, D. Y. and Yasti, S. Y.: *The Effect of Carbon Sources on the Thermal Shock Properties of MgO-C Refractories.* Universal Journal of Materials Science **6**(2018):139–147.

[93] Graham, D. and Kay, W.S.: *The morphology of thermally graphitized P-33 carbon black in relation to its adsorbent uniformity.* Journal of Colloid Science **16**(1961):182–185.

[94] Heidenreich, R.D.; Hess, W.M. and Ban, L.L.: *A test object and criteria for high resolution electron microscopy.* Journal of Applied Crystallography **1**(1968):1–19.

[95] Heindl, R.A. and Pendergast, W.L.: *Young's modulus of elasticity at several temperatures for some refractories of varying silica content.* Journal of Research of the National Bureau of Standard **13**(1934):6–851.

[96] Wachtman, J.B. and Lam, D.G.: *Young's modulus of various refractory materials as a function of temperature.* Journal of the American Ceramic Society **42**(1959):254–260.

[97] Joliff, Y.; Absi, J.; Glandus, J.C.; Huger, M. and Tessier-Doyen, N.: *Experimental and numerical study of the thermomechanical behaviour of refractory model materials.* Journal of the European Ceramic Society **27**(2007):1513–1520.

[98] Rossi, R.C.; Cost, J.R. and Janowski, K.R.: *Influence of the shape of dispersed particles on the elastic behavior of composite materials.* Journal of the American Ceramic Society **55**(1972):234–237.

[99] Spriggs, R.M.: *Expression for effect of porosity on elastic modulus of polycrystalline refractory materials, particularly aluminum oxide.* Journal of the American Ceramic Society **44**(1961):628–629.

[100] Phani, K.K. and Niyogi, S.K.: *Porosity dependence of ultrasonic velocity and elastic modulus in sintered uranium dioxide – a discussion.* Journal of Materials Science Letters **5**(1986):427–430.

[101] Munro, R.G.: *Analytical representations of elastic moduli data with simultaneous dependence on temperature and porosity.* Journal of Research of the National Institute of Standards and Technology **109**(2004):497.

[102] Joliff, Y.; Absi, Joseph.; Huger, Marc. and Glandus, J.C.: *Experimental and numerical study of the elastic modulus vs temperature of debonded model materials.* Computational Materials Science **44**(2008):826–831.

[103] Franklin, S.A. and Tucker, B.J.S.: *Hot strength and thermal shock resistance of magnesia-carbon refractories.* Britsh Ceramic Transactions **94**(1995):151–156.

[104] Werner, J.; Aneziris, C.G. and Dudczig, S.: *Young's Modulus of Elasticity of Carbon-Bonded Alumina Materials up to 1450° C.* Journal of the American Ceramic Society **96**(2013):2958–2965.

[105] Fruhstorfer, J.; Möhmel, S.; Thalheim, M.; Schmidt, G. and Aneziris, C.G.: *Microstructure and strength of fused high alumina materials with 2.5 wt% zirconia and 2.5 wt% titania additions for refractory applications.* Ceramics International **41**(2015):10644–53.

[106] Fruhstorfer, J. and Aneziris, C.G.: *The influence of the coarse fraction on the porosity of refractory castables.* Journal of Ceramic Science and Technology **5**(2014):155–165.

[107] Salmang, H.; Scholze, H. and Telle, R.: *Keramik.* Springer, 2007.

[108] Gault, C.; Platon, F. and Le Bras, D.: *Ultrasonic measurements of Young's modulus of Al_2O_3-based refractories at high temperatures.* Materials Science Engineering **74**(1985):105–111.

[109] André, D.; Levraut, B.; Tessier-Doyen, N. and Huger, M.: *A discrete element thermo-mechanical modelling of diffuse damage induced by thermal expansion mismatch of two-phase materials.* Computer Methods in Applied Mechanics and Engineering **318**(2017):898–916.

[110] Luchini, B.; Sciuti, V.F.; Angélico, R.A.; Canto, R.B. and Pandolfelli, V.C.: *Thermal expansion mismatch inter-inclusion cracking in ceramic systems.* Ceramics International **42**(2016):12512–12515.

[111] Luchini, B.; Sciuti, V.F.; Angélico, R.A.; Canto, R.B. and Pandolfelli, V.C.: *Critical inclusion size prediction in refractory ceramics via finite element simulations.* Journal of the European Ceramic Society **37**(2017):315–321.

[112] *Bakelite - Phenolharze: Leitfaden, Produktauswahl, Anwendung.* Bakelite AG, 2000.

[113] Roebben, G.; Bollen, B.; Brebels, A.; van Humbeeck, J. and van der Biest, O.: *Impulse excitation apparatus to measure resonant frequencies, elastic moduli, and internal friction at room and high temperature.* Review of Scientific Instruments **68**(1997):4511–4515.

[114] ASTM, E: *E 1876–1897.* Standard test method for dynamic Young's modulus, shear modulus, and Poisson's ratio by impulse excitation of vibration (1998).

[115] IMCE: *RFDA HTVP1600 catalogue.* `https://www.imce.eu/products/rfda-htvp1600` (accessed December 12, 2018).

[116] Kazuo, I.: *1.4.6 Alumina-Carbon (for Steel Casting).* In *Refractories Handbook*, pages 191–200. The Technical Association of Refractories, Tokyo, Japan, 1998.

[117] Nabertherm: *High-Temperature Furnaces with Scale for Determination of Combustion Loss and Thermogravimetric Analysis (TGA)*, (accessed December 13, 2018). `https://www.nabertherm.com/produkte/details/en/labor_hochtemperaturoefen`.

[118] Auerkari, P.: *Mechanical and physical properties of engineering alumina ceramics.* Julkaisija - Utgivare, 1996.

[119] *Properties and characteristics of graphite.* POCO Graphite, 2015.

[120] *Glassy Carbon Product Informartion.* SPI supplies, 2016.

[121] Tsai, J.-L. and Tu, J.-F.: *Characterizing mechanical properties of graphite using molecular dynamics simulation.* Materials & Design **31**(2010):194–199.

[122] Liu, D.; Gludovatz, B.; Barnard, H.S.; Kuball, M. and Ritchie, R.O.: *Damage tolerance of nuclear graphite at elevated temperatures.* Nature Communications **8**(2017):ncomms15942.

[123] Tsang, D.K.L.; Marsden, B.J.; Fok, S.L. and Hall, G.: *Graphite thermal expansion relationship for different temperature ranges.* Carbon **43**(2005):2902–2906.

[124] Hashin, Z. and Shtrikman, S.: *A variational approach to the theory of the elastic behaviour of multiphase materials.* J Mech Phys Solids **11**(1963):127–140.

[125] Fahmy, A.A. and Ragai, A.N.: *Thermal Expansion Behavior of Two-Phase Solids.* J App Phys **41**(1970):5108–5111.

[126] Zhao, J.X.; Bradt, R.C. and Walker, P.L.: *The fracture toughness of glassy carbons at elevated temperatures.* Carbon **23**(1985):15–18.

[127] MathWorks: *Matlab Documentation*, 2005.

[128] Dassault, S.: *Abaqus 6.10: Documentation and User Manual*, 2010.

[129] Apelian, D.; Mutharasan, R. and Ali, S.: *Removal of inclusions from steel melts by filtration.* Journal of Materials Science **20**(1985):3501–3514.

[130] Almanza, J. M.; Castillejos, A. H.; Acosta, F. and Flores, V. A.: *Microstructure and properties characterization of a new ceramic filter.* Materials & Design **15**(1994):135–140.

[131] Dávila-Maldonado, O.; Adams, A.; Oliveira, L.; Alquist, B. and Morales, R. D.: *Simulation of Fluid and Inclusions Dynamics during Filtration Operations of Ductile Iron Melts Using Foam Filters.* Metallurgical and Materials Transactions B **39**(2008):818–839.

[132] Damoah, L. N. W. and Zhang, L.: *Removal of Inclusions from Aluminum Through Filtration.* Metallurgical and Materials Transactions B **41**(2010):886–907.

[133] Essock, D.M.; Jaunich, H.; Aneziris, C.G. and Hubálková, J.: *Novel foamless ceramic filter for advanced metal casting technologies.* In Smith, J.D. (editor), *Proceedings of the Unified International Technical Conference on Refractories, 9th Biennial Worldwide Conference on Refractories: Nov 8–11, Rosen Centre Hotel, Orlando, Florida, USA*, pages 1–3. 2005.

[134] Zhang, L. and Thomas, B.G.: *Inclusions in continuous casting of steel.* In *XXIV National Steelmaking Symposium, Morelia, Mich, Mexico*, volume 26, page 28. 2003.

[135] Uemura, K.I.; Takahashi, M.; Koyama, S. and Nitta, M.: *Filtration mechanism of non-metallic inclusions in steel by ceramic loop filter.* ISIJ International **32**(1992):150–156.

[136] Spriestersbach, D.; Grad, P. and Kerscher, E.: *Influence of different non-metallic inclusion types on the crack initiation in high-strength steels in the VHCF regime.* International Journal of Fatigue **64**(2014):114–120.

[137] Klinger, C. and Bettge, D.: *Axle fracture of an ICE3 high speed train.* Engineering Failure Analysis **35**(2013):66–81.

[138] Murakami, Y. and Beretta, S.: *Small Defects and Inhomogeneities in Fatigue Strength: Experiments, Models and Statistical Implications.* Extremes **2**(1999):123–147.

[139] Krewerth, D.; Lippmann, T.; Weidner, A. and Biermann, H.: *Influence of non-metallic inclusions on fatigue life in the very high cycle fatigue regime.* International Journal of Fatigue **84**(2016):40–52.

[140] Pierson, H.O.: *Handbook of Carbon, Graphite, Diamond and Fullerenes.* Noyes Publications, Weinheim, New Jersey, 1993. ISBN 0-8155-1339-9.

[141] Solarek, J.; Himcinschi, C.; Klemm, Y.; Aneziris, C.G. and Biermann, H.: *Ductile behavior of fine-grained, carbon-bonded materials at elevated temperatures.* Carbon **122**(2017):141–149.

[142] Dudczig, S.; Aneziris, C. G.; Emmel, M.; Schmidt, G.; Hubálková, J. and Berek, H.: *Characterization of carbon-bonded alumina filters with active or reactive coatings in a steel casting simulator.* Ceramics International **40**(2014):16727–16742.

[143] Schmidt, A.; Salomon, A.; Dudczig, S.; Berek, H.; Rafaja, D. and Aneziris, C.G.: *Functionalized Carbon-Bonded Filters with an Open Porous Alumina Coating: Impact of Time on Interactions and Steel Cleanliness* . Advanced Engineering Materials **19**(2017):1700170–n/a.

[144] Voigt, C.; Jäckel, E.; Aneziris, C.G and Hubálková, J.: *Investigations of reticulated porous alumina foam ceramics based on different coating techniques with the aid of uCT and statistical characteristics.* Ceramics International **39**(2013):2415–2422.

[145] Voigt, C.; Storm, J.; Abendroth, M.; Aneziris, C.G.; Kuna, M. and Hubálková, J.: *The influence of the measurement parameters on the crushing strength of reticulated ceramic foams.* Journal of Materials Research **28**(2013):2288–2299.

[146] Vogt, U.F.; Gorbar, M.; Dimopoulos-Eggenschwiler, P.; Broenstrup, A.; Wagner, G. and Colombo, P.: *Improving the properties of ceramic foams by a vacuum infiltration process.* Journal of the European Ceramic Society **30**(2010):3005–3011.

[147] Jun, I.-K.; Kong, Y.-M.; Lee, S.-H.; Kim, H.-E.; Kim, H.-W. and Goretta, K.C.: *Reinforcement of a reticulated porous ceramic by a novel infiltration technique.* Journal of the American Ceramic Society **89**(2006):2317–2319.

[148] Liang, X.; Li, Y.; Liu, J.; Sang, S.; Chen, Y.; Li, B. and Aneziris, C.G.: *Improvement of the mechanical properties of SiC reticulated porous ceramics with optimized three-layered struts for porous media combustion.* Ceramics International **43**(2017):3741–3747.

[149] Apicella, B.; Tregossi, A.; Stanzione, F.; Ciajolo, A. and Russo, C.: *Analysis of petroleum and coal tar pitches as large PAH.* Chemical Engineering Transactions **57**(2017):775–780.

[150] Fraunhofer, ITWM: *MAVI–Modular algorithms for volume images.* Fraunhofer ITWM – Kaiserslautern, 2014.

[151] Otsu, N.: *A threshold selection method from gray-level histograms.* IEEE transactions on systems, man, and cybernetics **9**(1979):62–66.

[152] Maire, E.; Colombo, P.; Adrien, J.; Babout, L. and Biasetto, L.: *Characterization of the morphology of cellular ceramics by 3D image processing of X-ray tomography.* Journal of the European Ceramic Society **27**(2007):1973–1981.

[153] Elmoutaouakkil, A.; Salvo, L.; Maire, E. and Peix, G.: *2D and 3D Characterization of Metal Foams Using X-ray Tomography.* Advanced Engineering Materials **4**(2002):803–807.

[154] Luchini, B.; Storti, E.; Wetzig, T.; Settgast, C.; Abendroth, M.; Hubálková, J.; Pandolfelli, V.C and Aneziris, C.G.: *Mechanical and physical characterization of Al_2O_3-C foam filters produced by distinct processing routes: the importance of the ceramic strut morphology.* Journal of the European Ceramic Society (2019):1 – 28. Article in press.

[155] Stránský, K.; Bazan, J.; Dobrovská, J.; Balcar, M.; Fila, P. and Martínek, L.: *Application of the theory of physical similarity for the filtration of metallic melts* **42**(2008):175–178.

[156] Kondrat'ev, A.S.; Popov, V.N.; Aksel'rod, L.M.; Baranovskii, M.R.; Suvorov, S.A. and Tebuev, N.B.: *Possibilities of filter-refining of metals and the required characteristics of the filter elements: a review.* Ogneupory **31**(1990):13–19.

[157] Salvini, V.R.; Luchini, B.; Aneziris, C.G. and Pandolfelli, V.C.: *Innovation in ceramic foam filters manufacturing process.* International Journal of Applied Ceramic Technology **16**(2018):378–388.

[158] D'Angelo, C.; Ortona, A. and Colombo, P.: *Finite element analysis of reticulated ceramics under compression.* Acta Materialia **60**(2012):6692–6702.

[159] Werzner, E.; Mendes, M.A.A.; Ray, S. and Trimis, D.: *Numerical investigation on the depth filtration of liquid metals: influence of process conditions and inclusion properties.* Advanced Engineering Materials **15**(2013):1307–1314.

[160] Werzner, E.; Abendroth, M.; Demuth, C.; Settgast, C.; Trimis, D.; Krause, H. and Ray, S.: *Influence of foam morphology on effective properties related to metal melt filtration.* Advanced Engineering Materials **19**(2017):1–10.

[161] Fey, T.; Betke, U.; Rannabauer, S. and Scheffler, M.: *Reticulated replica ceramic foams: Processing, functionalization, and characterization.* Advanced Engineering Materials **19**(2017):1700369.

[162] Boettge, D.; Standke, G.; Fuessel, A. and Adler, J.: *Functionalization of open-celled foams by homogeneous slurry based coatings.* Journal of Materials Research **28**(2013):2220–2233.

[163] Venables, B.; Smith, D.; Gentleman, R. and Ihaka, R.: *Notes on R: a programming environment for data analysis and graphics.* University of Auckland, 1998.

[164] Brakke, K. A.: *The surface evolver.* Experimental mathematics **1**(1992):141–165.

[165] Lee, R.: *Phenolic Resin chemistry and proposed mechanism for thermal decomposition.* NASA Marshall Space Flight Center, Washington (2007):2–40.

[166] Chang, C. and Tackett, J. R.: *Characterization of phenolic resins with thermogravimetry-mass spectrometry.* Thermochimica Acta **192**(1991):181–190.

[167] Cowlard, F.C. and Lewis, J.C.: *Vitreous carbon – A new form of carbon.* Journal of Materials Science **2**(1967):507–12.

[168] Luz, A.P.; Renda, C.G.; Lucas, A.A.; Bertholdo, R.; Aneziris, C.G. and V.C., Pandolfelli: *Graphitization of phenolic resins for carbon-based refractories.* Ceramics International **43**(2017):8171–82.

[169] Marsden, B.J.; Haverty, M.; Bodel, W.; Hall, G.N.; Jones, A.N.; Mummery, P.M. and Treifi, M.: *Dimensional change, irradiation creep and thermal/mechanical property changes in nuclear graphite.* International Materrials Review **61**(2016):155–182.

[170] Wen, K.; Marrow, J. and Marsden, B.: *Microcracks in nuclear graphite and highly oriented pyrolytic graphite (HOPG).* Journal of Nuclear Materials **381**(2008):199–203.

[171] Solarek, J.; Aneziris, C.G. and Biermann, H.: *Mechanical Characterisation of Carbon-Bonded Magnesia at Temperatures up to 1400° C.* Journal of Ceramic Science and Technology **7**(2016):193–202.

[172] Solarek, J.; Bachmann, C.; Klemm, Y.; Aneziris, C.G. and Biermann, H.: *High-Temperature Compression Deformation Behavior of Fine-Grained Carbon-Bonded Alumina.* Journal of the American Ceramic Society **99**(2016):1390–1397.

[173] Whittaker, E.T. and Robinson, G.: *The calculus of observations*, volume 4. Blackie London, 1967.

[174] Pu, X.; Liu, X.; Qiu, F. and Huang, L.: *Novel method to optimize the structure of reticulated porous ceramics.* Journal of the American Ceramic Society **87**(2004):1392–1394.

[175] Conover, W.J.; Johnson, M.E. and Johnson, M.M.: *A comparative study of tests for homogeneity of variances, with applications to the outer continental shelf bidding data.* Technometrics **23**(1981):351–361.

[176] Fischer, U.; Chaves, H.; Aneziris, C.G. and Schmidt, G.: *Investigation of glaze layer formation on green ceramic bodies.* International Journal of Applied Ceramic Technology **12**(2015):81–94.

[177] Jankovský, O.; Storti, E.; Moritz, K.; Luchini, B.; Jiříčková, A. and Aneziris, C.G.: *Nano-functionalization of carbon-bonded alumina using graphene oxide and MWCNTs.* Journal of the European Ceramic Society (2018).

[178] Deng, B. and Jiang, D.: *Determination of the Weibull parameters from the mean value and the coefficient of variation of the measured strength for brittle ceramics.* Journal of Advanced Ceramics **6**(2017):149–156.

A Appendix

A.1 Random sample generator (Matlab code)

Part 1: Sample Generator

```
%%%%%%%%%%%%%%%%%%%%%%%%%%%%%%%%%%%%%%%%%%%%%%%%%%%%%%%%%%%%%%%%%%%%%%%%%%%%%%%%
%%%%%%%%%%%%%%%%%%%%%%%%VIRTUAL SAMPLES GENERATOR%%%%%%%%%%%%%%%%%%%%%%%%%%%%%%%
%%%%%%%%%%%%%%%%%%%%%%%%%%%%%%%%%%%%%%%%%%%%%%%%%%%%%%%%%%%%%%%%%%%%%%%%%%%%%%%%
%--
%This code was wrote to generate virtual samples and analyze the effect of
%the thermal expansion mismatch over the Young's modulus variation as a
%function of temperature.
%%--
%First version: May of 2017
%Author: Bruno Luchini
%Institution: IKGB TU B Freiberg
%%--
%%
clear all
close all
clc
format long
%% Initialization Parameters
vers=9;
Tmax=1000;
SS=50;
Vf=0.15; % Particle volume fraction [%]
NAME=['T30R1' num2str(100*Vf) 'vers' num2str(vers) '.mat'];
r1=3e-3; % Particle radius 1 [m]
r2=1e-3; %Particle radius 2 [m]
vl1=0.47; %Paricle 1 ratio over the total particles
L=20*r1; %Sample size [m]
%% Calculating the number of particles to satisfy the volume fraction condition
syms N1 N2
eq1= (N1*pi*r1^2+N2*pi*r2^2)/L^2==Vf;
eq2= (N1*pi*r1^2)/(N1*pi*r1^2+N2*pi*r2^2) == vl1;
[A, B] = solve(eq1,eq2);
n1=ceil(double(A));
n2=ceil(double(B));
R1=ones(n1,1)*r1;
R2=ones(n2,1)*r2;
r=[R1; R2];
n=n1+n2;
VFF=(n1*pi*r1^2+n2*pi*r2^2)/L^2;
disp(['The Surface Fraction is ' num2str(VFF)])
disp(['The Number of Particles is ' num2str(n1+n2)])
```

```
42 disp(['The Number of Particles R1 is ' num2str(n1)])
43 disp(['The Number of Particles R2 is ' num2str(n2)])
44 %% Generation of the random distributated particles
45 d=[];
46 Dmin=1;
47 count=1;
48 BB=randperm(n);
49 for i=1:n
50     r22(i)=r(BB(i));
51 end
52 r=r22;
53 for i=1:n
54     xc(i)=r(i)+(1*rand(1)*(L-2*r(i)));
55     yc(i)=r(i)+(1*rand(1)*(L-2*r(i)));
56     dx=xc-xc(i);
57     dy=yc-yc(i);
58     d=sqrt(dx.^2+dy.^2);
59     if d(i)==0
60         d(i)=1;
61     end
62     [Dmin, Pmin] =min(d);
63     AA(1)=1;
64     AA(2)=1;
65     while sum(AA)==2
66         if Dmin >(r(i)+r(Pmin)+r2*0.1)
67             AA(1)=0;
68         end
69         if count>100
70             AA(2)=0;
71         end
72         count=count+1;
73         xc(i)=r(i)+(1*rand(1)*(L-2*r(i)));
74         yc(i)=r(i)+(1*rand(1)*(L-2*r(i)));
75         dx=xc-xc(i);
76         dy=yc-yc(i);
77         d=sqrt(dx.^2+dy.^2);
78         if d(i)==0
79             d(i)=1;
80         end
81         [Dmin, Pmin] =min(d);
82     end
83     count2=count;
84     count=1;
85 end
86 %% Plot the first geometry (possibly with overlaps)
87 figure
88 for i=1:n
89     rectangle('Position',[xc(i)-r(i),yc(i)-r(i),2*r(i),2*r(i)], ...
90     'Curvature',[1,1])
91     hold on
92     axis square
93 end
94 %% Moving overlaped particles
95 for i=1:n
96     for j=1:n
```

```
97          RestMatrix(i,j)=r(i)+r(j)+r2*0.2;
98          if i == j
99              RestMatrix(i,j) =0;
100         end
101     end
102 end
103 overlap=1;
104 j=1;
105 K=ones(n,1);
106 while overlap>0
107     for i=1:n
108         dx=xc-xc(i);
109         dy=yc-yc(i);
110         d=sqrt(dx.^2+dy.^2);
111         if d(i)==0
112             d(i)=1;
113         end
114         d2=d-RestMatrix(i,:);
115         [Dmin, Pmin] =min(d2);
116         if Dmin<0
117             AAA=0.1*rand(1);
118             xc(i)=xc(i)+1*AAA*(xc(i)-xc(Pmin));
119             yc(i)=yc(i)+1*AAA*(yc(i)-yc(Pmin));
120             if xc(i) < r(i)+0.2*r2
121                 xc(i)=xc(i)+0.5*rand(1)*r(i);
122             end
123             if xc(i) > L-r(i)-0.2*r2
124                 xc(i)=xc(i)-0.5*rand(1)*r(i);
125             end
126             if yc(i) < r(i)+0.2*r2
127                 yc(i)=yc(i)+0.5*rand(1)*r(i);
128             end
129             if yc(i) > L-r(i)-0.2*r2
130                 yc(i)=yc(i)-0.5*rand(1)*r(i);
131             end
132             K(i)=1;
133         else
134             K(i)=0;
135         end
136     end
137     overlap=sum(K);
138     disp(['The percentage of overlaps is ' num2str(100*overlap/n)])
139     j=j+1;
140 end
141 %% Plot the final geometry
142 figure
143 for i=1:n
144     rectangle('Position',[xc(i)-r(i),yc(i)-r(i),2*r(i),2*r(i)], ...
145     'Curvature',[1,1],'FaceColor',[214 215 239]./255,'EdgeColor',[102 106 ...
            194]./255)
146     hold on
147     txt1 = num2str(i);
148     text(xc(i),yc(i),txt1)
149     axis square
150 end
```

```
151 hold on
152 rectangle('Position',[0,0,L,L])
153
154 %% Calculating the GAPS' size
155 alpha_m=4e-6;
156 alpha_i=8.5e-6;
157
158 r_i=r;
159 xc_h=xc;
160 yc_h=yc;
161 % How many particles have no gaps
162 d0=ceil(0.10*n);
163 for i=1:d0
164     DT(i)=0;
165 end
166 % How many particles have no possible closed gaps
167 d1=ceil(0.00*n);
168 for i=d0+1:d0+d1
169     DT(i)=1.5*Tmax;
170 end
171 % Gaps size distribution (normal)
172 for i=d0+d1+1:n
173     DT(i)=800;
174 %     DT(i)=normrnd(Tmax,SS);
175 %     if DT(i)>Tmax
176 %         DT(i)=2*Tmax-DT(i);
177 %     end
178 end
179 % DT=ones(length(DT))*800;
180 for i=1:n
181     Δ_r=abs(r_i(i)*(alpha_i-alpha_m)*DT(i))
182     r_h(i)=r_i(i)+Δ_r;
183     xc_i(i)=xc_h(i);
184     yc_i(i)=yc_h(i)-Δ_r*cos(pi/12);
185 end
186 %% Save the geometry
187
188 save(NAME,'r_i','r_h','L','xc_i','yc_i','xc_h','yc_h')
```

Part 2: Abaqus conversion:

```
1  %%%%
```

```
%%
clear all
close all
clc
%% Geometry to be loaded
A0='T_ex53vers9';
A00=[A0 '.txt'];
A000=[A0 '.mat'];
load(A000)
%% INPUT Properties
T=[0 20 100 200 300 400 500 600 700 800 900 1000 1100 1200 1400]; ...
    %Temperature [Celsius degrees]
%-------------------------------------------------------------------------
%-----------------MATRIX------------------
%-------------------------------------------------------------------------
E_m=1e9*[28.819 28.799 28.719 28.619 28.519 28.419 28.319 28.219 28.119 ...
    28.019 27.919 27.819 27.719 27.619 27.419]; %Young's Modulus [Pa]
nu_m=0.2; %Poisson coefficient
alpha_m=1e-6*[1.9 1.9 1.9 2 2.9 3.4 3.7 4.0 4.1 4.3 4.3 4.4 4.4 4.5 4.5]; ...
    %Thermal expansion coeficient [1/Celsius degrees]
%-------------------------------------------------------------------------
%-----------------PARTICLE----------------
%-------------------------------------------------------------------------
E_p=1e9*[220 220 218 216 213 210 208 205 200 197 195 193 190 186 ...
    186];%Young's Modulus [Pa]
nu_p=0.22; %Poisson coefficient
alpha_p=1e-6*[2.6 2.6 6.0 6.9 7.6 7.9 8.0 8.0 8.2 8.3 8.5 8.6 8.7 8.8 8.8]; ...
    %Thermal expansion coeficient [1/Celsius degrees]
%-------------------------------------------------------------------------
%-------------------------------------------------------------------------
%% Getting geometry from samples' file
x=xc_h; %Pores' x center position
y=yc_h; %Pores' y center position
r=r_h; %Pores' radius
n=length(x); %Number of pores
x2=xc_i; %Particles' x center position
y2=yc_i; %Particles' y center position
r2=r_i; %Particles' radius
L=20*max(r); %Sample size
%% Name of the final file


fileID = fopen(A00,'w');
%% Initialization
fprintf(fileID,'%0s\n',['L=' num2str(L)]);
fprintf(fileID,'%0s\n','from part import *');
fprintf(fileID,'%0s\n','from material import *');
fprintf(fileID,'%0s\n','from section import *');
fprintf(fileID,'%0s\n','from assembly import *');
fprintf(fileID,'%0s\n','from step import *');
fprintf(fileID,'%0s\n','from interaction import *');
fprintf(fileID,'%0s\n','from load import *');
fprintf(fileID,'%0s\n','from mesh import *');
fprintf(fileID,'%0s\n','from optimization import *');
fprintf(fileID,'%0s\n','from job import *');
```

```
fprintf(fileID,'%0s\n','from sketch import *');
fprintf(fileID,'%0s\n','from visualization import *');
fprintf(fileID,'%0s\n','from connectorBehavior import *');
%% Geometry
%MATRIX GENERATION
fprintf(fileID,'%0s\n','mdb.models[''Model-1'']. ...
ConstrainedSketch(name=''__profile__'', sheetSize=0.05)');
fprintf(fileID,'%0s\n','mdb.models[''Model-1''].sketches ...
[''__profile__''].sketchOptions.setValues(decimalPlaces=6)');
fprintf(fileID,'%0s\n','mdb.models[''Model-1''].sketches ...
[''__profile__''].rectangle(point1=(0, 0),point2=(L, L))');
for i=1:n
    A1=['mdb.models[''Model-1''].sketches ...
    [''__profile__''].CircleByCenterPerimeter(center= ...
    (' num2str(x(i)) ',' num2str(y(i)) '), point1=(' num2str(x(i)) ',' ...
        num2str(y(i)+r(i)) '))'];
    A2=['mdb.models[''Model-1''].sketches ...
    [''__profile__''].ConstructionLine(angle= ...
    255.0,point1=(' num2str(x(i)) ',' num2str(y(i)) '))'];
    A3=['mdb.models[''Model-1''].sketches ...
    [''__profile__''].ConstructionLine(angle= ...
    285.0,point1=(' num2str(x(i)) ',' num2str(y(i)) '))'];
    A4=['mdb.models[''Model-1''].sketches ...
    [''__profile__''].autoTrimCurve(curve1= ...
    mdb.models[''Model-1''].sketches[''__profile__''].geometry[' ...
        num2str(6*i) '], point1=(' num2str(x(i)) ',' num2str(y(i)-r(i)) '))'];
    A5=['mdb.models[''Model-1''].sketches[''__profile__''].Line(point1=(' ...
        num2str(x(i)-r(i)*sin(pi/12)) ',' num2str(y(i)-r(i)*cos(pi/12)) '), ...
        point2=(' num2str(x(i)+r(i)*sin(pi/12)) ',' ...
        num2str(y(i)-r(i)*cos(pi/12)) '))'];
    A6=['mdb.models[''Model-1''].sketches ...
    [''__profile__''].delete(objectList= ...
    (mdb.models[''Model-1''].sketches[''__profile__''].geometry ...
    [' num2str(6*i+1) ...
        '],mdb.models[''Model-1''].sketches[''__profile__''].geometry[' ...
        num2str(6*i+2) ']))'];
    fprintf(fileID,'%0s\n',A1);
    fprintf(fileID,'%0s\n',A2);
    fprintf(fileID,'%0s\n',A3);
    fprintf(fileID,'%0s\n',A4);
    fprintf(fileID,'%0s\n',A5);
    fprintf(fileID,'%0s\n',A6);
end
fprintf(fileID,'%0s\n','mdb.models[''Model-1'']. ...
Part(dimensionality=TWO_D_PLANAR, name=''Part-1'', type=DEFORMABLE_BODY)');
fprintf(fileID,'%0s\n','mdb.models[''Model-1''].parts[''Part-1'']. ...
BaseShell(sketch=mdb.models[''Model-1''].sketches[''__profile__''])');
fprintf(fileID,'%0s\n','del mdb.models[''Model-1''].sketches[''__profile__'']');
%SURFACE CREATION
for i=1:n
    A1=['mdb.models[''Model-1''].parts[''Part-1''].Surface(name=''hh' ...
        num2str(i) ''', side1Edges=mdb.models[''Model-1''].parts ...
    [''Part-1''].edges.findAt((('' num2str(x(i)) ',' ...
        num2str(y(i)-r(i)*cos(pi/12)) ', 0.0), ))')'];
    A2=['mdb.models[''Model-1''].parts[''Part-1''].Surface ...
```

```
110     (name=''hc' num2str(i) ''', side1Edges=mdb.models[''Model-1''].parts ...
111     [''Part-1''].edges.findAt((('' num2str(x(i)-r(i)) ',' num2str(y(i)) ', ...
            0.0), ), ((' num2str(x(i)+r(i)) ',' num2str(y(i)) ', 0.0), ), ))'];
112     fprintf(fileID,'%0s\n',A1);
113     fprintf(fileID,'%0s\n',A2);
114 end
115 %PARTICLES GEOMETRY
116 for i=1:n
117     A1=['mdb.models[''Model-1''].ConstrainedSketch(name=''__profile__'', ...
            sheetSize=0.05)'];
118     A2=['mdb.models[''Model-1''].sketches[''__profile__'']. ...
119     sketchOptions.setValues(decimalPlaces=6)'];
120     A3=['mdb.models[''Model-1''].sketches[''__profile__'']. ...
121     CircleByCenterPerimeter(center=(' num2str(x2(i)) ','  num2str(y2(i)) '), ...
122     point1=(' num2str(x2(i)) ',' num2str(y2(i)+r2(i)) '))'];
123     A4=['mdb.models[''Model-1''].sketches[''__profile__'']. ...
124     ConstructionLine(angle=255.0, point1=(' num2str(x2(i)) ',' ...
            num2str(y2(i)) '))'];
125     A5=['mdb.models[''Model-1''].sketches[''__profile__'']. ...
126     ConstructionLine(angle=285.0, point1=(' num2str(x2(i)) ',' ...
            num2str(y2(i)) '))'];
127     A6=['mdb.models[''Model-1''].sketches[''__profile__'']. ...
128     autoTrimCurve(curve1=mdb.models[''Model-1''].sketches ...
129     [''__profile__''].geometry[2], point1=(' num2str(x2(i)) ',' ...
            num2str(y2(i)-r2(i)) '))'];
130     A7=['mdb.models[''Model-1''].sketches[''__profile__''].Line(point1=(' ...
            num2str(x2(i)-r2(i)*sin(pi/12)) ',' ...
131     num2str(y2(i)-r2(i)*cos(pi/12)) '), point2=(' ...
            num2str(x2(i)+r2(i)*sin(pi/12)) ...
132      ',' num2str(y2(i)-r2(i)*cos(pi/12)) '))'];
133     A8=['mdb.models[''Model-1''].Part(dimensionality=TWO_D_PLANAR, ...
134      name=''Part-' num2str(i+1) ''', type=DEFORMABLE_BODY)'];
135     A9=['mdb.models[''Model-1''].parts[''Part-' num2str(i+1) ...
136     ''']].BaseShell(sketch=mdb.models[''Model-1''].sketches[''__profile__''])'];
137     A10=['del mdb.models[''Model-1''].sketches[''__profile__''']'];
138     fprintf(fileID,'%0s\n',A1);
139     fprintf(fileID,'%0s\n',A2);
140     fprintf(fileID,'%0s\n',A3);
141     fprintf(fileID,'%0s\n',A4);
142     fprintf(fileID,'%0s\n',A5);
143     fprintf(fileID,'%0s\n',A6);
144     fprintf(fileID,'%0s\n',A7);
145     fprintf(fileID,'%0s\n',A8);
146     fprintf(fileID,'%0s\n',A9);
147     fprintf(fileID,'%0s\n',A10);
148 end
149 %Particles surface creation
150 for i=1:n
151     A1=['mdb.models[''Model-1''].parts[''Part-' num2str(i+1) ...
            ''']].Surface(name=''ph' num2str(i) ''', ...
            side1Edges=mdb.models[''Model-1''].parts[''Part-' num2str(i+1) ...
            ''']].edges.findAt((('' num2str(x2(i)) ',' ...
            num2str(y2(i)-r2(i)*cos(pi/12)) ', 0.0), )))'];
152     A2=['mdb.models[''Model-1''].parts[''Part-' num2str(i+1) ...
            ''']].Surface(name=''pc' num2str(i) ''', ...
```

```
            side1Edges=mdb.models[''Model-1''].parts[''Part-' num2str(i+1) ...
            ''']. edges.findAt((('  num2str(x2(i)-r2(i)) ',' num2str(y2(i)) ', ...
            0.0), ), (('  num2str(x2(i)+r2(i)) ',' num2str(y2(i)) ', 0.0), ), ))'];
153     fprintf(fileID,'%0s\n',A1);
154     fprintf(fileID,'%0s\n',A2);
155 end
156 %% Assembly
157 A1=['mdb.models[''Model-1''].rootAssembly.DatumCsysByDefault(CARTESIAN)'];
158 fprintf(fileID,'%0s\n',A1);
159 for i=1:n+1
160     A1=['mdb.models[''Model-1''].rootAssembly.Instance(dependent=ON, ...
            name=''Part-1-' num2str(i) ...
            ''',part=mdb.models[''Model-1''].parts[''Part-' num2str(i) ''']) '];
161     fprintf(fileID,'%0s\n',A1);
162 end
163 %% Contact creation
164 fprintf(fileID,'%0s\n','## CONTACT CREATION');
165 A1=['mdb.models[''Model-1''].ContactProperty(''IntProp-1'')'];
166 A2=['mdb.models[''Model-1''].interactionProperties[''IntProp-1''] ...
167 .TangentialBehavior(dependencies=0, directionality=ISOTROPIC, ...
        elasticSlipStiffness=None, ...
168  formulation=PENALTY, fraction=0.005, maximumElasticSlip=FRACTION, ...
         pressureDependency=OFF, ...
169   shearStressLimit=None, slipRateDependency=OFF, table=((0.35, ), ), ...
          temperatureDependency=OFF)'];
170 A3=['mdb.models[''Model-1''].interactionProperties[''IntProp-1'']. ...
171 NormalBehavior(allowSeparation=OFF, constraintEnforcementMethod=DEFAULT, ...
        pressureOverclosure=HARD)'];
172 fprintf(fileID,'%0s\n',A1);
173 fprintf(fileID,'%0s\n',A2);
174 fprintf(fileID,'%0s\n',A3);
175 A1=['mdb.models[''Model-1''].ContactProperty(''IntProp-2'')'];
176 A2=['mdb.models[''Model-1''].interactionProperties[''IntProp-2'']. ...
177 TangentialBehavior(dependencies=0, directionality=ISOTROPIC, ...
        elasticSlipStiffness=None, formulation=PENALTY, fraction=0.005, ...
        maximumElasticSlip=FRACTION, pressureDependency=OFF, ...
        shearStressLimit=None, slipRateDependency=OFF, table=((0.35, ), ), ...
        temperatureDependency=OFF)'];
178 A3=['mdb.models[''Model-1''].interactionProperties[''IntProp-2'']. ...
179 NormalBehavior(allowSeparation=ON, constraintEnforcementMethod=DEFAULT, ...
        pressureOverclosure=HARD)'];
180 fprintf(fileID,'%0s\n',A1);
181 fprintf(fileID,'%0s\n',A2);
182 fprintf(fileID,'%0s\n',A3);
183 %Contact pairs
184 fprintf(fileID,'%0s\n','## CONTACT PAIRS');
185 for i=1:n
186     A1=['mdb.models[''Model-1''].Tie(adjust=ON, ...
            master=mdb.models[''Model-1''].rootAssembly.instances[''Part-1-1'']. ...
187     surfaces[''hh' num2str(i) ''']], name=''Constraint-' num2str(i) ''', ...
188      positionToleranceMethod=COMPUTED, slave= mdb.models[''Model-1'']. ...
189      rootAssembly.instances[''Part-1-' num2str(i+1) ''']. surfaces[''ph' ...
             num2str(i) ''']], thickness=ON, tieRotations=ON)'];
190     fprintf(fileID,'%0s\n',A1);
191 end
```

```
for i=1:n
    A1=['mdb.models[''Model-1''].SurfaceToSurfaceContactStd ...
    (adjustMethod=NONE,clearanceRegion=None, createStepName=''Initial'', ...
        datumAxis=None, initialClearance=OMIT, ...
        interactionProperty=''IntProp-2'', ...
     master=mdb.models[''Model-1''].rootAssembly.instances[''Part-1-1'']. ...
     surfaces[''hc' num2str(i) '''], name=''Int2-' num2str(i) ''', ...
         slave=mdb.models[''Model-1''].rootAssembly.instances[''Part-1-' ...
         num2str(i+1) '''].surfaces[''pc' num2str(i) '''], sliding=FINITE, ...
         thickness=ON)'];
    fprintf(fileID,'%0s\n',A1);
end
%% Materials Creation
fprintf(fileID,'%0s\n','## Materials Creation');
%Matrix
aa11= num2str(E_m(1));
aa12= num2str(nu_m);
aa13= num2str(T(1));
AA=[ '(' aa11 ',' aa12 ',' aa13 ')' ];
for i=2:length(T)
    aa11= num2str(E_m(i));
    aa12= num2str(nu_m);
    aa13= num2str(T(i));
    aa=[ ',(' aa11 ',' aa12 ',' aa13 ')' ];
    AA=strcat(AA,aa);
end
aa11= num2str(alpha_m(1));
aa12= num2str(T(1));
AA2=[ '(' aa11 ',' aa12 ')' ];
for i=2:length(T)
    aa11= num2str(alpha_m(i));
    aa12= num2str(T(i));
    aa=[ ',(' aa11 ',' aa12 ')' ];
    AA2=strcat(AA2,aa);
end
A1=['mdb.models[''Model-1''].Material(name=''matrix'')'];
A2=['mdb.models[''Model-1''].materials[''matrix''].Elastic(table=(' AA '), ...
    temperatureDependency=ON)'];
A3=['mdb.models[''Model-1''].materials[''matrix''].Expansion(table=(' AA2 ...
    '), temperatureDependency=ON)'];
A4=['mdb.models[''Model-1''].HomogeneousSolidSection(material=''matrix'', ...
    name=''matrix'',thickness=None)'];
A5=['mdb.models[''Model-1''].parts[''Part-1''].Set(faces= ...
    mdb.models[''Model-1''].parts[''Part-1''].faces[0:1], name=''Set-1'')'];
A6=['mdb.models[''Model-1''].parts[''Part-1''].SectionAssignment(offset=0.0, ...
    offsetField='''', offsetType=MIDDLE_SURFACE, region= ...
    mdb.models[''Model-1''].parts[''Part-1''].sets[''Set-1''], ...
    sectionName=''matrix'', thicknessAssignment=FROM_SECTION)'];
fprintf(fileID,'%0s\n',A1);
fprintf(fileID,'%0s\n',A2);
fprintf(fileID,'%0s\n',A3);
fprintf(fileID,'%0s\n',A4);
fprintf(fileID,'%0s\n',A5);
fprintf(fileID,'%0s\n',A6);
%Particle
```

```
235 aa11= num2str(E_p(1));
236 aa12= num2str(nu_p);
237 aa13= num2str(T(1));
238 AA=[ '(' aa11 ',' aa12 ',' aa13 ')' ];
239 for i=2:length(T)
240     aa11= num2str(E_p(i));
241     aa12= num2str(nu_p);
242     aa13= num2str(T(i));
243     aa=[ ',(' aa11 ',' aa12 ',' aa13 ')' ];
244     AA=strcat(AA,aa);
245 end
246 aa11= num2str(alpha_p(1));
247 aa12= num2str(T(1));
248 AA2=[ '(' aa11 ',' aa12 ')' ];
249 for i=2:length(T)
250     aa11= num2str(alpha_p(i));
251     aa12= num2str(T(i));
252     aa=[ ',(' aa11 ',' aa12 ')' ];
253     AA2=strcat(AA2,aa);
254 end
255 A1=['mdb.models[''Model-1''].Material(name=''particle'')'];
256 A2=['mdb.models[''Model-1''].materials[''particle''].Elastic(table=(' AA '), ...
        temperatureDependency=ON)'];
257 A3=['mdb.models[''Model-1''].materials[''particle''].Expansion(table=(' AA2 ...
        '), temperatureDependency=ON)'];
258 A4=['mdb.models[''Model-1''].HomogeneousSolidSection(material=''particle'', ...
        name=''particle'',thickness=None)'];
259 fprintf(fileID,'%0s\n',A1);
260 fprintf(fileID,'%0s\n',A2);
261 fprintf(fileID,'%0s\n',A3);
262 fprintf(fileID,'%0s\n',A4);
263 for i=1:n
264     A5=['mdb.models[''Model-1''].parts[''Part-' num2str(i+1) '''].Set(faces= ...
            mdb.models[''Model-1''].parts[''Part-' num2str(i+1) '''].faces[0:1], ...
            name=''Set-1'')'];
265     A6=['mdb.models[''Model-1''].parts[''Part-' num2str(i+1) ...
            '''].SectionAssignment(offset=0.0, offsetField='''', ...
            offsetType=MIDDLE_SURFACE, region= ...
            mdb.models[''Model-1''].parts[''Part-' num2str(i+1) ...
            '''].sets[''Set-1''], sectionName=''particle'', ...
            thicknessAssignment=FROM_SECTION)'];
266     fprintf(fileID,'%0s\n',A5);
267     fprintf(fileID,'%0s\n',A6);
268 end
269 %Mesh
270 fprintf(fileID,'%0s\n','## Mesh Generation');
271 for i=1:n+1
272     A1=['mdb.models[''Model-1''].parts[''Part-' num2str(i) ...
            '''].setMeshControls(elemShape=TRI, ...
            regions=mdb.models[''Model-1''].parts[''Part-' num2str(i) ...
            '''].faces[0:1])'];
273     A2=['mdb.models[''Model-1''].parts[''Part-' num2str(i) ...
            '''].seedPart(deviationFactor=0.1,minSizeFactor=0.1, size=3e-05)'];
274     A3=['mdb.models[''Model-1''].parts[''Part-' num2str(i) ...
            '''].generateMesh()'];
```

```
275     fprintf(fileID,'%0s\n',A1);
276     fprintf(fileID,'%0s\n',A2);
277     fprintf(fileID,'%0s\n',A3);
278 end
279
280 %Reference Points
281
282 A1=['mdb.models[''Model-1''].rootAssembly.regenerate()'];
283 A2=['mdb.models[''Model-1''].rootAssembly.Set(name=''rf1'', ...
        nodes=mdb.models[''Model-1''].rootAssembly.instances[''Part-1-1'']. ...
284 nodes.findAt(((0,' num2str(L) ',0), )))'];
285 A3=['mdb.models[''Model-1''].rootAssembly.Set(name=''rf2'', ...
        nodes=mdb.models[''Model-1''].rootAssembly.instances[''Part-1-1'']. ...
286 nodes.findAt((' num2str(L) ',0 ,0), )))'];
287 A1='-------------------------------------'
288 fprintf(fileID,'%0s\n',A1);
289     fprintf(fileID,'%0s\n',A1);
290     fprintf(fileID,'%0s\n',A1);
291
292 %% Steps
293
294 A1=['mdb.models[''Model-1''].StaticStep(initialInc=0.5, maxNumInc=10000, ...
        minInc=1e-07, name=''H1'', nlgeom=ON, previous=''Initial'')'];
295 A2=['mdb.models[''Model-1''].StaticStep(name=''Y1'', previous=''H1'')'];
296 A3=['mdb.models[''Model-1''].StaticStep(initialInc=0.5, maxNumInc=10000, ...
        minInc=1e-07,name=''H2'', previous=''Y1'')'];
297 A4=['mdb.models[''Model-1''].StaticStep(name=''Y2'', previous=''H2'')'];
298 A5=['mdb.models[''Model-1''].StaticStep(initialInc=0.5, maxNumInc=10000, ...
        minInc=1e-07,name=''H3'', previous=''Y2'')'];
299 A6=['mdb.models[''Model-1''].StaticStep(name=''Y3'', previous=''H3'')'];
300 A7=['mdb.models[''Model-1''].StaticStep(initialInc=0.3, maxNumInc=1000, ...
        minInc=1e-07,name=''H4'', previous=''Y3'')'];
301 A8=['mdb.models[''Model-1''].StaticStep(name=''Y4'', previous=''H4'')'];
302 A9=['mdb.models[''Model-1''].StaticStep(initialInc=0.3, maxNumInc=10000, ...
        minInc=1e-07,name=''H5'', previous=''Y4'')'];
303 A10=['mdb.models[''Model-1''].StaticStep(name=''Y5'', previous=''H5'')'];
304 A11=['mdb.models[''Model-1''].StaticStep(initialInc=0.2, maxNumInc=10000, ...
        minInc=1e-07,name=''H6'', previous=''Y5'')'];
305 A12=['mdb.models[''Model-1''].StaticStep(name=''Y6'', previous=''H6'')'];
306 A13=['mdb.models[''Model-1''].StaticStep(initialInc=0.2, maxNumInc=10000, ...
        minInc=1e-07, name=''H7'', previous=''Y6'')'];
307 A14=['mdb.models[''Model-1''].StaticStep(name=''Y7'', previous=''H7'')'];
308 A15=['mdb.models[''Model-1''].StaticStep(initialInc=0.2, maxNumInc=10000, ...
        minInc=1e-07, name=''H8'', previous=''Y7'')'];
309 A16=['mdb.models[''Model-1''].StaticStep(name=''Y8'', previous=''H8'')'];
310 A17=['mdb.models[''Model-1''].StaticStep(initialInc=0.2, maxNumInc=10000, ...
        minInc=1e-07, name=''H9'', previous=''Y8'')'];
311 A18=['mdb.models[''Model-1''].StaticStep(name=''Y9'', previous=''H9'')'];
312 A19=['mdb.models[''Model-1''].StaticStep(initialInc=0.15, maxNumInc=10000, ...
        minInc=1e-07, name=''H10'', previous=''Y9'')'];
313 A20=['mdb.models[''Model-1''].StaticStep(name=''Y10'', previous=''H10'')'];
314 A21=['mdb.models[''Model-1''].StaticStep(initialInc=0.15, maxNumInc=10000, ...
        minInc=1e-07, name=''H11'', previous=''Y10'')'];
315 A22=['mdb.models[''Model-1''].StaticStep(name=''Y11'', previous=''H11'')'];
316 A23=['mdb.models[''Model-1''].StaticStep(initialInc=0.15, maxNumInc=10000, ...
```

```
       minInc=1e-07, name=''H12'', previous=''Y11'')'];
317 A24=['mdb.models[''Model-1''].StaticStep(name=''Y12'', previous=''H12'')'];
318 A25=['mdb.models[''Model-1''].StaticStep(initialInc=0.1, maxNumInc=10000, ...
       minInc=1e-07, name=''H13'', previous=''Y12'')'];
319 A26=['mdb.models[''Model-1''].StaticStep(name=''Y13'', previous=''H13'')'];
320      fprintf(fileID,'%0s\n',A1);
321      fprintf(fileID,'%0s\n',A2);
322      fprintf(fileID,'%0s\n',A3);
323      fprintf(fileID,'%0s\n',A4);
324      fprintf(fileID,'%0s\n',A5);
325      fprintf(fileID,'%0s\n',A6);
326      fprintf(fileID,'%0s\n',A7);
327      fprintf(fileID,'%0s\n',A8);
328      fprintf(fileID,'%0s\n',A9);
329      fprintf(fileID,'%0s\n',A10);
330      fprintf(fileID,'%0s\n',A11);
331      fprintf(fileID,'%0s\n',A12);
332      fprintf(fileID,'%0s\n',A13);
333      fprintf(fileID,'%0s\n',A14);
334      fprintf(fileID,'%0s\n',A15);
335      fprintf(fileID,'%0s\n',A16);
336      fprintf(fileID,'%0s\n',A17);
337      fprintf(fileID,'%0s\n',A18);
338      fprintf(fileID,'%0s\n',A19);
339      fprintf(fileID,'%0s\n',A20);
340      fprintf(fileID,'%0s\n',A21);
341      fprintf(fileID,'%0s\n',A22);
342      fprintf(fileID,'%0s\n',A23);
343      fprintf(fileID,'%0s\n',A24);
344      fprintf(fileID,'%0s\n',A25);
345      fprintf(fileID,'%0s\n',A26);
346 %% AMPLITUDE
347 A1=['mdb.models[''Model-1''].TabularAmplitude(data=((0.0, 0.0), (1.0, ...
       20.0)), name=''A1'', smooth=SOLVER_DEFAULT, timeSpan=STEP)'];
348 A2=['mdb.models[''Model-1''].TabularAmplitude(data=((0.0, 20.0), (1.0, ...
       100.0)), name=''A2'', smooth=SOLVER_DEFAULT, timeSpan=STEP)'];
349 A3=['mdb.models[''Model-1''].TabularAmplitude(data=((0.0, 100.0), (1.0, ...
       200.0)), name=''A3'', smooth=SOLVER_DEFAULT, timeSpan=STEP)'];
350 A4=['mdb.models[''Model-1''].TabularAmplitude(data=((0.0, 200.0), (1.0, ...
       300.0)), name=''A4'', smooth=SOLVER_DEFAULT, timeSpan=STEP)'];
351 A5=['mdb.models[''Model-1''].TabularAmplitude(data=((0.0, 300.0), (1.0, ...
       400.0)), name=''A5'', smooth=SOLVER_DEFAULT, timeSpan=STEP)'];
352 A6=['mdb.models[''Model-1''].TabularAmplitude(data=((0.0, 400.0), (1.0, ...
       500.0)), name=''A6'', smooth=SOLVER_DEFAULT, timeSpan=STEP)'];
353 A7=['mdb.models[''Model-1''].TabularAmplitude(data=((0.0, 500.0), (1.0, ...
       600.0)), name=''A7'', smooth=SOLVER_DEFAULT, timeSpan=STEP)'];
354 A8=['mdb.models[''Model-1''].TabularAmplitude(data=((0.0, 600.0), (1.0, ...
       700.0)), name=''A8'', smooth=SOLVER_DEFAULT, timeSpan=STEP)'];
355 A9=['mdb.models[''Model-1''].TabularAmplitude(data=((0.0, 700.0), (1.0, ...
       800.0)), name=''A9'', smooth=SOLVER_DEFAULT, timeSpan=STEP)'];
356 A10=['mdb.models[''Model-1''].TabularAmplitude(data=((0.0, 800.0), (1.0, ...
       900.0)), name=''A10'', smooth=SOLVER_DEFAULT, timeSpan=STEP)'];
357 A11=['mdb.models[''Model-1''].TabularAmplitude(data=((0.0, 900.0), (1.0, ...
       970.0)),name=''A11'', smooth=SOLVER_DEFAULT, timeSpan=STEP)'];
358      fprintf(fileID,'%0s\n',A1);
```

```
359      fprintf(fileID,'%0s\n',A2);
360      fprintf(fileID,'%0s\n',A3);
361      fprintf(fileID,'%0s\n',A4);
362      fprintf(fileID,'%0s\n',A5);
363      fprintf(fileID,'%0s\n',A6);
364      fprintf(fileID,'%0s\n',A7);
365      fprintf(fileID,'%0s\n',A8);
366      fprintf(fileID,'%0s\n',A9);
367      fprintf(fileID,'%0s\n',A10);
368      fprintf(fileID,'%0s\n',A11);
369  %% BC
370
371  A1=['mdb.models[''Model-1''].rootAssembly.Set ...
372  (edges=mdb.models[''Model-1''].rootAssembly.instances ...
373  [''Part-1-1''].edges.findAt((('' num2str(L/2) '', 0.0, 0.0), )), ...
         name=''Set-3'')'];
374  A2=['mdb.models[''Model-1''].DisplacementBC ...
375  (amplitude=UNSET, createStepName=''Initial'', distributionType=UNIFORM, ...
376   fieldName='''', localCsys=None, name=''BC-1'', ...
          region=mdb.models[''Model-1'']. ...
377   rootAssembly.sets[''Set-3''], u1=UNSET, u2=SET, ur3=UNSET)'];
378  A3=['mdb.models[''Model-1''].rootAssembly.Set(edges=mdb.models[''Model-1'']. ...
379  rootAssembly.instances[''Part-1-1''].edges.findAt(((0.0,' num2str(L/2) ', ...
         0.0), )), name=''Set-4'')'];
380  A4=['mdb.models[''Model-1''].DisplacementBC(amplitude=UNSET, ...
         createStepName=''Initial'', distributionType=UNIFORM, fieldName='', ...
         localCsys=None, name=''BC-2'', ...
         region=mdb.models[''Model-1''].rootAssembly.sets[''Set-4''], u1=SET, ...
         u2=UNSET, ur3=UNSET)'];
381  A1='------------------------------'
382  fprintf(fileID,'%0s\n',A1);
383      fprintf(fileID,'%0s\n',A1);
384      fprintf(fileID,'%0s\n',A1);
385      fprintf(fileID,'%0s\n',A1);
386
387  for i=1:12
388  A1=['mdb.models[''Model-1''].DisplacementBC(amplitude=UNSET, ...
         createStepName=''Y'' num2str(i) ''', distributionType=UNIFORM, ...
         fieldName='''', fixed=OFF, localCsys=None, name=''Y'' num2str(i) ''', ...
         region=mdb.models[''Model-1''].rootAssembly.sets[''rf1''], u1=UNSET, ...
         u2=0.0, ur3=UNSET)'];
389  A2=['mdb.models[''Model-1''].boundaryConditions[''Y'' num2str(i) ...
         ''']].deactivate(''H'' num2str(i+1) ''')'];
390      fprintf(fileID,'%0s\n',A1);
391      fprintf(fileID,'%0s\n',A2);
392  end
393
394  A1=['mdb.models[''Model-1''].DisplacementBC(amplitude=UNSET, ...
         createStepName=''Y13'', distributionType=UNIFORM, fieldName='''', ...
         fixed=OFF, localCsys=None, name=''Y13'', ...
         region=mdb.models[''Model-1''].rootAssembly.sets[''rf1''], u1=UNSET, ...
         u2=0.0, ur3=UNSET)'];
395  fprintf(fileID,'%0s\n',A1);
396
397  %%
```

```
398 A1=['mdb.models[''Model-1''].fieldOutputRequests[''F-Output-1''] ...
399 .setValues(variables=(''S'', ''LE'', ''U'', ''CF'', ''CSTRESS'', ''CDISP'', ...
        ''CSTATUS'', ''NT''))'];
400 A2=['mdb.models[''Model-1''].historyOutputRequests[''H-Output-1'']. ...
401 setValues(rebar=EXCLUDE, ...
        region=mdb.models[''Model-1''].rootAssembly.sets[''rf1''], ...
        sectionPoints=DEFAULT, variables=(''U2'', ''RF2'', ''NT''))'];
402     fprintf(fileID,'%0s\n',A1);
403     fprintf(fileID,'%0s\n',A2);
404
405 fclose(fileID);
406 %% Plot geometry
407 figure
408 for i=1:n
409     rectangle('Position',[x(i)-r(i),y(i)-r(i),2*r(i),2*r(i)], ...
410     'Curvature',[1,1],'FaceColor',[0 51 102]./255,'EdgeColor',[0 0 0]./255)
411     hold on
412 %     txt1 = num2str(i);
413 %     text(x(i),y(i),txt1,'FontSize',6)
414     axis square
415 %     xlim([0 L])
416 %     ylim([0 L])
417 end
418 hold on
419 rectangle('Position',[0,0,L,L])
420 print('geo2.pdf','-dpdf')
```

A.2 Particles' positioning FEM model

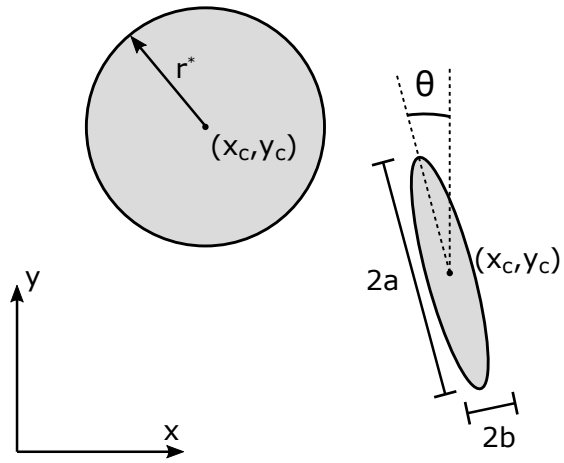

Figure A.1: Particles dimensions.

Table A.2.1: Particles dimensions and positioning

Particle	r^*[mm]	a[mm]	b[mm]	θ[°]	x_c[mm]	y_c[mm]
1	0.5	-	-	-	8.1119	4.6534
2	0.5	-	-	-	2.7446	8.8679
3	0.5	-	-	-	4.5211	6.9402
4	0.5	-	-	-	3.8786	2.6124
5	0.5	-	-	-	1.554	6.7512
6	0.5	-	-	-	0.94926	2.5746
7	0.5	-	-	-	6.4555	0.81372
8	0.5	-	-	-	9.0568	9.1135
9	0.5	-	-	-	7.3371	9.2836
10	0.5	-	-	-	9.208	6.5206
11	0.5	-	-	-	6.2787	4.181
12	0.5	-	-	-	5.5606	7.8473
13	0.5	-	-	-	3.0659	5.2015
14	0.5	-	-	-	0.87366	4.8613
15	0.5	-	-	-	2.1966	1.4028
16	0.5	-	-	-	2.8202	7.0536
17	0.5	-	-	-	8.3009	7.5638
18	0.5	-	-	-	9.1324	0.72247

19	0.5	-	-	-	5.674	3.2171
20	0.5	-	-	-	9.0568	3.1982
21	0.5	-	-	-	4.3321	8.8301
22	0.5	-	-	-	5.5984	5.6551
23	0.5	-	-	-	4.3085	1.0107
24	0.5	-	-	-	2.4801	3.6518
25	0.5	-	-	-	0.83586	8.7167
26	0.5	-	-	-	7.0063	2.5179
27	0.25	-	-	-	6.222	9.1135
28	0.25	-	-	-	6.7701	6.0141
29	0.25	-	-	-	7.715	3.5762
30	0.25	-	-	-	5.0503	1.9698
31	0.25	-	-	-	5.9763	1.6863
32	0.25	-	-	-	7.5544	1.9556
33	0.25	-	-	-	7.3938	7.0725
34	0.25	-	-	-	4.351	5.1259
35	0.25	-	-	-	2.0643	6.0519
36	0.25	-	-	-	2.1777	4.6534
37	0.25	-	-	-	1.176	3.9353
38	0.25	-	-	-	2.9903	1.9509
39	0.25	-	-	-	2.0454	2.5557
40	0.25	-	-	-	0.57128	1.6107
41	0.25	-	-	-	2.669	0.45789
42	-	0.25	0.05	0	9.8474	9.2433
43	-	0.25	0.05	0	9.6604	9.2299
44	-	0.25	0.05	0	6.649	8.9838
45	-	0.25	0.05	0	4.9297	8.9626
46	-	0.25	0.05	0	4.1012	9.6709
47	-	0.25	0.05	0	2.0565	9.711
48	-	0.25	0.05	0	1.816	9.6843
49	-	0.25	0.05	0	2.404	6.0093
50	-	0.25	0.05	0	9.2461	5.1407
51	-	0.25	0.05	0	9.8875	6.2899
52	-	0.25	0.05	0	9.8742	7.1987
53	-	0.25	0.05	0	9.7539	7.7733
54	-	0.25	0.05	0	6.1458	7.947

55	-	0.25	0.05	0	6.3997	8.3746
56	-	0.25	0.05	0	6.2794	6.7443
57	-	0.25	0.05	0	6.1992	5.448
58	-	0.25	0.05	0	3.1924	4.2453
59	-	0.25	0.05	0	0.85383	4.0716
60	-	0.25	0.05	0	0.30593	4.0716
61	-	0.25	0.05	0	0.59992	3.3099
62	-	0.25	0.05	0	0.43956	3.2297
63	-	0.25	0.05	0	1.375	7.8267
64	-	0.25	0.05	0	0.14556	5.7955
65	-	0.25	0.05	0	0.11884	4.9937
66	-	0.25	0.05	0	0.10494	4.1384
67	-	0.25	0.05	0	9.3129	4.566
68	-	0.25	0.05	0	9.794	3.791
69	-	0.25	0.05	0	9.9009	4.3656
70	-	0.25	0.05	0	9.8474	5.3946
71	-	0.25	0.05	0	9.1125	5.2342
72	-	0.25	0.05	0	2.0565	8.9092
73	-	0.25	0.05	0	2.2837	6.5839
74	-	0.25	0.05	0	0.26584	5.0204
75	-	0.25	0.05	0	1.4347	5.045
76	-	0.25	0.05	0	1.8294	3.4302
77	-	0.25	0.05	0	3.6707	9.5641
78	-	0.25	0.05	0	3.8975	9.6586
79	-	0.25	0.05	0	8.6222	9.6869
80	-	0.25	0.05	0	7.9324	9.668
81	-	0.25	0.05	0	2.4441	2.8154
82	-	0.25	0.05	0	5.7181	2.3343
83	-	0.25	0.05	0	9.6144	2.666
84	-	0.25	0.05	0	9.8695	0.73832
85	-	0.25	0.05	0	0.83586	1.1068
86	-	0.25	0.05	0	3.4628	6.0016
87	-	0.25	0.05	0	9.7221	0.61678
88	-	0.25	0.05	0	1.3699	1.9398
89	-	0.25	0.05	0	2.439	5.1871
90	-	0.25	0.05	0	1.6674	5.8126

91	-	0.25	0.05	0	0.81696	3.3558
92	-	0.25	0.05	0	0.1933	3.4881
93	-	0.25	0.05	0	9.8128	2.4109
94	-	0.25	0.05	0	7.5544	0.81864
95	-	0.25	0.05	0	7.0347	0.46429
96	-	0.25	0.05	0	5.8666	0.58895
97	-	0.25	0.05	0	5.3527	4.2629
98	-	0.25	0.05	0	5.107	3.8472
99	-	0.25	0.05	0	3.0659	3.9984
100	-	0.25	0.05	0	5.0314	7.3435
101	-	0.25	0.05	0	6.8457	6.9844
102	-	0.25	0.05	0	0.3067	5.6237
103	-	0.25	0.05	0	6.7134	1.636
104	-	0.25	0.05	0	6.4299	1.636
105	-	0.25	0.05	0	5.5417	2.2975
106	-	0.25	0.05	0	4.8595	1.477
107	-	0.25	0.05	0	1.2138	0.78557
108	-	0.25	0.05	0	1.4595	1.258
109	-	0.25	0.05	0	2.4801	2.1463
110	-	0.25	0.05	0	1.5918	3.2424
111	-	0.25	0.05	0	0.2311	6.3607
112	-	0.25	0.05	0	8.093	3.6393
113	-	0.25	0.05	0	7.2993	4.6787
114	-	0.25	0.05	0	6.5433	3.3558
115	-	0.25	0.05	0	4.3888	1.8628
116	-	0.25	0.05	0	2.669	2.7321
117	-	0.25	0.05	0	3.3872	4.2629
118	-	0.25	0.05	0	5.5039	6.6253
119	-	0.25	0.05	0	3.7085	6.1906
120	-	0.25	0.05	0	1.4028	9.5546
121	-	0.25	0.05	0	0.1933	7.5702
122	-	0.25	0.05	30	9.5497	5.1636
123	-	0.25	0.05	30	9.2632	5.7676
124	-	0.25	0.05	30	2.9962	6.1904
125	-	0.25	0.05	30	2.1836	5.3589
126	-	0.25	0.05	30	6.6437	8.2315

127	-	0.25	0.05	30	4.7916	8.3827
128	-	0.25	0.05	30	5.0751	8.2315
129	-	0.25	0.05	30	1.8942	8.4267
130	-	0.25	0.05	30	3.0884	3.1457
131	-	0.25	0.05	30	2.9548	3.2258
132	-	0.25	0.05	30	6.015	4.776
133	-	0.25	0.05	30	5.2132	9.6136
134	-	0.25	0.05	30	5.0128	9.6403
135	-	0.25	0.05	30	4.8123	9.6403
136	-	0.25	0.05	30	1.8055	0.59324
137	-	0.25	0.05	30	2.5004	0.83378
138	-	0.25	0.05	30	3.0907	1.0877
139	-	0.25	0.05	30	5.179	1.135
140	-	0.25	0.05	30	4.3475	2.2784
141	-	0.25	0.05	30	0.18855	8.6915
142	-	0.25	0.05	30	0.20191	8.1971
143	-	0.25	0.05	30	0.45582	8.01
144	-	0.25	0.05	30	0.20191	6.8073
145	-	0.25	0.05	30	0.18855	7.1146
146	-	0.25	0.05	30	0.49591	6.7271
147	-	0.25	0.05	30	3.4215	9.2331
148	-	0.25	0.05	30	3.3175	9.356
149	-	0.25	0.05	30	8.8549	7.1731
150	-	0.25	0.05	30	1.3512	3.2793
151	-	0.25	0.05	30	4.211	4.629
152	-	0.25	0.05	30	5.9348	4.9364
153	-	0.25	0.05	30	5.7611	4.9765
154	-	0.25	0.05	30	6.4026	2.7849
155	-	0.25	0.05	30	6.2957	2.8383
156	-	0.25	0.05	30	6.1754	2.9051
157	-	0.25	0.05	30	7.2863	0.44517
158	-	0.25	0.05	30	7.6359	1.4941
159	-	0.25	0.05	30	7.995	1.1539
160	-	0.25	0.05	30	8.4863	1.7114
161	-	0.25	0.05	30	3.6199	1.1255
162	-	0.25	0.05	30	7.8816	5.7463

163	-	0.25	0.05	30	8.3635	5.425
164	-	0.25	0.05	30	4.6688	4.9147
165	-	0.25	0.05	30	2.6904	5.8212
166	-	0.25	0.05	30	5.1885	6.8519
167	-	0.25	0.05	30	2.2214	0.61526
168	-	0.25	0.05	30	3.4317	3.0505
169	-	0.25	0.05	30	0.70624	5.9657
170	-	0.25	0.05	30	1.352	5.7557
171	-	0.25	0.05	30	0.37402	2.7744
172	-	0.25	0.05	30	1.5742	8.2149
173	-	0.25	0.05	30	1.541	9.1008
174	-	0.25	0.05	30	1.2575	8.1937
175	-	0.25	0.05	30	1.0119	7.1165
176	-	0.25	0.05	30	5.0184	8.4016
177	-	0.25	0.05	30	0.93066	7.7567
178	-	0.25	0.05	30	3.3175	7.9291
179	-	0.25	0.05	30	3.1852	6.077
180	-	0.25	0.05	30	4.8861	5.4156
181	-	0.25	0.05	30	6.965	3.6013
182	-	0.25	0.05	30	4.3758	5.9258
183	-	0.25	0.05	30	4.168	5.9069
184	-	0.25	0.05	30	9.0817	4.4139
185	-	0.25	0.05	30	8.9683	5.4723
186	-	0.25	0.05	30	6.9272	4.0548
187	-	0.25	0.05	30	7.5461	3.0627
188	-	0.25	0.05	30	7.7965	2.9398
189	-	0.25	0.05	30	5.3397	0.7192
190	-	0.25	0.05	30	7.3619	0.84205
191	-	0.25	0.05	30	5.2688	0.99324
192	-	0.25	0.05	30	3.2608	3.091
193	-	0.25	0.05	30	3.8089	4.2249
194	-	0.25	0.05	30	3.4687	1.1822
195	-	0.25	0.05	30	2.8828	1.1444
196	-	0.25	0.05	30	1.6355	0.63416
197	-	0.25	0.05	30	0.65278	0.76645
198	-	0.25	0.05	30	1.0875	1.6547

199	-	0.25	0.05	30	0.59608	3.9792
200	-	0.25	0.05	30	0.67168	6.4928
201	-	0.25	0.05	30	0.61498	7.192
202	-	0.25	0.05	60	1.6828	4.8136
203	-	0.25	0.05	60	7.7257	6.8074
204	-	0.25	0.05	60	7.8013	8.1681
205	-	0.25	0.05	60	8.1887	8.2153
206	-	0.25	0.05	60	1.1029	3.3413
207	-	0.25	0.05	60	0.32832	2.105
208	-	0.25	0.05	60	4.0566	4.0701
209	-	0.25	0.05	60	4.9787	4.2438
210	-	0.25	0.05	60	7.6647	5.0723
211	-	0.25	0.05	60	6.8362	7.6381
212	-	0.25	0.05	60	0.29479	9.7763
213	-	0.25	0.05	60	1.0766	9.7362
214	-	0.25	0.05	60	3.8829	5.941
215	-	0.25	0.05	60	0.27475	1.0098
216	-	0.25	0.05	60	0.99637	1.9319
217	-	0.25	0.05	60	5.132	1.3567
218	-	0.25	0.05	60	6.4186	0.16459
219	-	0.25	0.05	60	1.5174	0.155
220	-	0.25	0.05	60	3.1746	3.5756
221	-	0.25	0.05	60	0.51529	7.5847
222	-	0.25	0.05	60	1.2009	0.19753
223	-	0.25	0.05	60	3.3884	9.6422
224	-	0.25	0.05	60	1.7848	1.8517
225	-	0.25	0.05	60	8.8029	1.8559
226	-	0.25	0.05	60	9.1809	1.922
227	-	0.25	0.05	60	9.2754	2.4701
228	-	0.25	0.05	60	9.3037	2.6402
229	-	0.25	0.05	60	9.729	0.20225
230	-	0.25	0.05	60	8.8029	1.2417
231	-	0.25	0.05	60	5.0621	0.2253
232	-	0.25	0.05	60	3.4018	0.40848
233	-	0.25	0.05	60	3.1345	0.44857
234	-	0.25	0.05	60	0.941	0.77866

235	-	0.25	0.05	60	0.48743	0.92985
236	-	0.25	0.05	60	0.22714	2.2385
237	-	0.25	0.05	60	0.39847	1.9828
238	-	0.25	0.05	60	6.45	6.2121
239	-	0.25	0.05	60	7.2532	5.9853
240	-	0.25	0.05	60	1.697	4.0671
241	-	0.25	0.05	60	4.7586	3.3111
242	-	0.25	0.05	60	5.2688	2.5174
243	-	0.25	0.05	60	0.61972	3.6702
244	-	0.25	0.05	60	9.729	8.6784
245	-	0.25	0.05	60	8.2926	9.6611
246	-	0.25	0.05	60	8.51	8.565
247	-	0.25	0.05	60	9.4455	7.2421
248	-	0.25	0.05	60	9.6345	5.8435
249	-	0.25	0.05	60	7.2343	6.5617
250	-	0.25	0.05	60	7.2532	6.2215
251	-	0.25	0.05	60	7.7068	5.8813
252	-	0.25	0.05	60	7.1587	5.3333
253	-	0.25	0.05	60	4.4184	4.0104
254	-	0.25	0.05	60	4.1727	4.3127
255	-	0.25	0.05	60	3.9081	4.634
256	-	0.25	0.05	60	3.6435	4.7852
257	-	0.25	0.05	60	1.6238	8.5119
258	-	0.25	0.05	60	1.7057	8.7364
259	-	0.25	0.05	60	1.7537	8.9429
260	-	0.25	0.05	60	3.5868	7.5822
261	-	0.25	0.05	60	7.4743	0.34872
262	-	0.25	0.05	60	5.4389	9.2453
263	-	0.25	0.05	60	4.5318	9.6611
264	-	0.25	0.05	60	3.6435	9.1508
265	-	0.25	0.05	60	3.379	9.7934
266	-	0.25	0.05	60	2.434	9.6233
267	-	0.25	0.05	60	0.35514	9.2264
268	-	0.25	0.05	60	0.60083	9.6611
269	-	0.25	0.05	60	0.86541	7.998
270	-	0.25	0.05	60	4.7775	6.1837

271	-	0.25	0.05	60	7.3666	4.1804
272	-	0.25	0.05	60	6.7429	8.5461
273	-	0.25	0.05	60	7.8391	6.6562
274	-	0.25	0.05	60	8.4816	2.026
275	-	0.25	0.05	60	7.7635	1.2511
276	-	0.25	0.05	60	8.1226	5.5601
277	-	0.25	0.05	60	6.4028	5.1632
278	-	0.25	0.05	60	4.6452	3.9348
279	-	0.25	0.05	60	2.7175	6.2593
280	-	0.25	0.05	60	3.8892	3.7647
281	-	0.25	0.05	60	4.6263	4.5584
282	-	0.25	0.05	90	2.8647	9.6241
283	-	0.25	0.05	90	2.1431	9.3434
284	-	0.25	0.05	90	3.5062	8.849
285	-	0.25	0.05	90	4.1877	8.2343
286	-	0.25	0.05	90	7.1277	8.4614
287	-	0.25	0.05	90	6.4862	7.2053
288	-	0.25	0.05	90	8.0631	7.0182
289	-	0.25	0.05	90	2.691	4.4123
290	-	0.25	0.05	90	3.9472	2.0336
291	-	0.25	0.05	90	5.5107	3.8243
292	-	0.25	0.05	90	4.7356	3.6372
293	-	0.25	0.05	90	7.0876	3.3299
294	-	0.25	0.05	90	6.9005	3.1428
295	-	0.25	0.05	90	7.2346	5.1339
296	-	0.25	0.05	90	9.1188	7.4592
297	-	0.25	0.05	90	3.3191	8.3946
298	-	0.25	0.05	90	3.0385	8.2075
299	-	0.25	0.05	90	2.5574	8.3011
300	-	0.25	0.05	90	0.28559	9.437
301	-	0.25	0.05	90	0.96713	9.4904
302	-	0.25	0.05	90	1.0206	9.3033
303	-	0.25	0.05	90	4.8227	9.3104
304	-	0.25	0.05	90	5.2526	9.9246
305	-	0.25	0.05	90	5.5739	9.5608
306	-	0.25	0.05	90	5.7062	8.7009

307	-	0.25	0.05	90	5.9424	6.8299
308	-	0.25	0.05	90	6.9818	7.4441
309	-	0.25	0.05	90	7.1992	8.2001
310	-	0.25	0.05	90	7.615	8.7292
311	-	0.25	0.05	90	9.7127	8.1245
312	-	0.25	0.05	90	9.2875	8.3607
313	-	0.25	0.05	90	4.7891	5.7086
314	-	0.25	0.05	90	5.1232	6.4302
315	-	0.25	0.05	90	4.8693	5.9625
316	-	0.25	0.05	90	5.2301	5.0938
317	-	0.25	0.05	90	7.4543	0.12083
318	-	0.25	0.05	90	3.7501	6.5464
319	-	0.25	0.05	90	4.2604	6.3007
320	-	0.25	0.05	90	5.8101	6.2629
321	-	0.25	0.05	90	1.8036	2.1241
322	-	0.25	0.05	90	1.9926	3.0124
323	-	0.25	0.05	90	1.2744	3.5793
324	-	0.25	0.05	90	1.6713	3.7872
325	-	0.25	0.05	90	0.68854	5.4881
326	-	0.25	0.05	90	2.7485	9.4379
327	-	0.25	0.05	90	3.7501	7.2835
328	-	0.25	0.05	90	3.5801	6.8488
329	-	0.25	0.05	90	1.7894	5.0487
330	-	0.25	0.05	90	1.761	5.3086
331	-	0.25	0.05	90	1.6146	4.581
332	-	0.25	0.05	90	1.4823	4.2786
333	-	0.25	0.05	90	2.3138	4.2786
334	-	0.25	0.05	90	1.7469	2.8423
335	-	0.25	0.05	90	3.1076	0.13973
336	-	0.25	0.05	90	4.903	0.40432
337	-	0.25	0.05	90	4.5817	0.17753
338	-	0.25	0.05	90	5.9623	0.24435
339	-	0.25	0.05	90	6.8307	9.7781
340	-	0.25	0.05	90	9.5143	9.7592
341	-	0.25	0.05	90	9.1109	8.1629
342	-	0.25	0.05	90	3.7505	0.085885

343	-	0.25	0.05	90	3.41	0.78229
344	-	0.25	0.05	90	2.0871	0.29092
345	-	0.25	0.05	90	1.109	0.45629
346	-	0.25	0.05	90	3.7313	1.576
347	-	0.25	0.05	90	8.2429	5.7643
348	-	0.25	0.05	90	2.2004	5.6393
349	-	0.25	0.05	90	8.3416	1.163
350	-	0.25	0.05	90	8.456	1.3493
351	-	0.25	0.05	90	6.2731	9.8915
352	-	0.25	0.05	90	7.5299	9.8821
353	-	0.25	0.05	90	6.6417	9.6458
354	-	0.25	0.05	90	9.3064	2.2186
355	-	0.25	0.05	90	2.0304	8.0772
356	-	0.25	0.05	90	1.1043	7.5103
357	-	0.25	0.05	90	1.4256	6.1685
358	-	0.25	0.05	90	1.0476	5.9039
359	-	0.25	0.05	90	1.4823	5.4503
360	-	0.25	0.05	90	3.0698	4.6188
361	-	0.25	0.05	90	3.4856	3.8061
362	-	0.25	0.05	90	4.8274	4.3731
363	-	0.25	0.05	90	4.2793	3.3525
364	-	0.25	0.05	90	9.5899	4.8455
365	-	0.25	0.05	120	2.5645	6.5281
366	-	0.25	0.05	120	1.6691	7.3834
367	-	0.25	0.05	120	3.7806	3.4946
368	-	0.25	0.05	120	2.8728	0.736
369	-	0.25	0.05	120	2.7216	2.3518
370	-	0.25	0.05	120	3.0145	2.8243
371	-	0.25	0.05	120	7.2952	5.7129
372	-	0.25	0.05	120	6.7339	5.5125
373	-	0.25	0.05	120	7.0012	4.4969
374	-	0.25	0.05	120	1.8562	0.91545
375	-	0.25	0.05	120	7.0778	1.0573
376	-	0.25	0.05	120	9.733	1.388
377	-	0.25	0.05	120	8.7598	0.20683
378	-	0.25	0.05	120	6.8982	0.17849

379	-	0.25	0.05	120	5.6325	1.0252
380	-	0.25	0.05	120	5.7454	1.1518
381	-	0.25	0.05	120	5.5564	0.19739
382	-	0.25	0.05	120	3.9409	0.46109
383	-	0.25	0.05	120	0.44428	0.37692
384	-	0.25	0.05	120	7.1912	1.1518
385	-	0.25	0.05	120	2.8822	1.5675
386	-	0.25	0.05	120	3.2224	1.5109
387	-	0.25	0.05	120	4.0681	1.7707
388	-	0.25	0.05	120	4.2618	3.5897
389	-	0.25	0.05	120	6.2651	5.9804
390	-	0.25	0.05	120	4.2902	5.5174
391	-	0.25	0.05	120	3.865	5.3284
392	-	0.25	0.05	120	8.1361	8.9003
393	-	0.25	0.05	120	9.1755	7.6908
394	-	0.25	0.05	120	8.722	5.9899
395	-	0.25	0.05	120	3.6949	7.086
396	-	0.25	0.05	120	6.2084	3.5708
397	-	0.25	0.05	120	3.2791	6.4623
398	-	0.25	0.05	120	7.0967	1.3975
399	-	0.25	0.05	120	8.0605	1.7187
400	-	0.25	0.05	120	8.4479	6.7364
401	-	0.25	0.05	120	8.8402	4.7972
402	-	0.25	0.05	120	8.7868	5.1313
403	-	0.25	0.05	120	3.7488	3.3138
404	-	0.25	0.05	120	4.9381	2.806
405	-	0.25	0.05	120	8.1482	0.6001
406	-	0.25	0.05	120	8.9605	1.5766
407	-	0.25	0.05	120	6.1007	2.0309
408	-	0.25	0.05	120	5.8335	1.3093
409	-	0.25	0.05	120	6.956	1.8572
410	-	0.25	0.05	120	7.6242	5.3985
411	-	0.25	0.05	120	0.34107	0.20015
412	-	0.25	0.05	120	0.28762	1.3093
413	-	0.25	0.05	120	0.36868	4.3835
414	-	0.25	0.05	120	3.6571	8.5034

415	-	0.25	0.05	120	6.5297	9.4484
416	-	0.25	0.05	120	5.9438	9.6751
417	-	0.25	0.05	120	5.4336	8.9381
418	-	0.25	0.05	120	7.4935	7.9931
419	-	0.25	0.05	120	3.0712	2.5881
420	-	0.25	0.05	120	3.4492	2.0211
421	-	0.25	0.05	120	6.0383	2.4369
422	-	0.25	0.05	120	6.3218	7.4829
423	-	0.25	0.05	120	5.6226	7.1049
424	-	0.25	0.05	120	6.0383	6.5001
425	-	0.25	0.05	120	9.5403	5.542
426	-	0.25	0.05	120	9.4968	3.9866
427	-	0.25	0.05	120	8.8731	4.0055
428	-	0.25	0.05	120	8.1361	2.4747
429	-	0.25	0.05	120	8.2684	2.8149
430	-	0.25	0.05	120	7.7912	2.3896
431	-	0.25	0.05	120	2.7877	7.9742
432	-	0.25	0.05	120	1.7483	7.5963
433	-	0.25	0.05	120	5.4147	4.7803
434	-	0.25	0.05	120	4.9422	3.0984
435	-	0.25	0.05	120	9.4401	1.6809
436	-	0.25	0.05	120	6.9266	5.6119
437	-	0.25	0.05	120	6.5108	4.7614
438	-	0.25	0.05	120	4.791	2.4936
439	-	0.25	0.05	120	3.7516	5.593
440	-	0.25	0.05	120	7.8337	8.4467
441	-	0.25	0.05	120	6.0572	7.1994
442	-	0.25	0.05	120	6.8132	7.9364
443	-	0.25	0.05	120	5.3769	8.5979
444	-	0.25	0.05	120	4.6965	7.9742
445	-	0.25	0.05	120	3.9973	7.9553
446	-	0.25	0.05	150	0.15245	2.5582
447	-	0.25	0.05	150	0.19359	1.642
448	-	0.25	0.05	150	9.8131	2.9649
449	-	0.25	0.05	150	5.0482	0.76338
450	-	0.25	0.05	150	5.5827	0.48275

451	-	0.25	0.05	150	5.6629	0.69656
452	-	0.25	0.05	150	8.1285	1.9594
453	-	0.25	0.05	150	7.7543	0.73665
454	-	0.25	0.05	150	7.8879	0.2422
455	-	0.25	0.05	150	8.0791	0.22935
456	-	0.25	0.05	150	8.2917	0.24352
457	-	0.25	0.05	150	8.4692	0.22884
458	-	0.25	0.05	150	8.2287	0.80347
459	-	0.25	0.05	150	8.5227	0.64311
460	-	0.25	0.05	150	8.4425	3.0352
461	-	0.25	0.05	150	9.2042	3.9305
462	-	0.25	0.05	150	8.7766	4.3181
463	-	0.25	0.05	150	8.5093	6.4161
464	-	0.25	0.05	150	8.7231	8.0866
465	-	0.25	0.05	150	5.9435	8.3672
466	-	0.25	0.05	150	5.7698	9.0086
467	-	0.25	0.05	150	5.8233	9.2358
468	-	0.25	0.05	150	1.587	9.7035
469	-	0.25	0.05	150	3.8588	5.0931
470	-	0.25	0.05	150	0.43778	6.2558
471	-	0.25	0.05	150	0.42442	5.8615
472	-	0.25	0.05	150	0.90551	6.229
473	-	0.25	0.05	150	0.91887	6.6433
474	-	0.25	0.05	150	1.6138	2.4739
475	-	0.25	0.05	150	2.91	2.4605
476	-	0.25	0.05	150	8.2955	6.0553
477	-	0.25	0.05	150	8.0149	6.3493
478	-	0.25	0.05	150	7.8812	6.229
479	-	0.25	0.05	150	7.6273	6.336
480	-	0.25	0.05	150	6.7988	6.5631
481	-	0.25	0.05	150	3.2441	7.4986
482	-	0.25	0.05	150	2.0414	7.7525
483	-	0.25	0.05	150	2.1884	7.7525
484	-	0.25	0.05	150	2.3889	7.8059
485	-	0.25	0.05	150	2.5225	7.846
486	-	0.25	0.05	150	7.7209	7.4184

487	-	0.25	0.05	150	7.4536	7.6857
488	-	0.25	0.05	150	1.1861	1.2177
489	-	0.25	0.05	150	8.496	2.4605
490	-	0.25	0.05	150	8.3222	3.4494
491	-	0.25	0.05	150	4.6473	2.3269
492	-	0.25	0.05	150	5.4625	1.5919
493	-	0.25	0.05	150	5.5025	1.8057
494	-	0.25	0.05	150	4.615	1.7644
495	-	0.25	0.05	150	4.5136	2.9817
496	-	0.25	0.05	150	9.5957	1.179
497	-	0.25	0.05	150	4.6915	7.6519
498	-	0.25	0.05	150	4.0678	7.6141
499	-	0.25	0.05	150	7.2428	3.6642
500	-	0.25	0.05	150	7.7531	4.0233
501	-	0.25	0.05	150	8.5658	3.8721
502	-	0.25	0.05	150	8.3012	3.8154
503	-	0.25	0.05	150	9.7942	1.9633
504	-	0.25	0.05	150	3.5765	8.0487
505	-	0.25	0.05	150	8.3201	9.2961
506	-	0.25	0.05	150	8.0744	8.5968
507	-	0.25	0.05	150	6.4491	7.7085
508	-	0.25	0.05	150	7.2617	7.6897
509	-	0.25	0.05	150	9.5485	7.8219
510	-	0.25	0.05	150	9.7186	6.8203
511	-	0.25	0.05	150	8.6414	5.7053
512	-	0.25	0.05	150	8.2445	6.499
513	-	0.25	0.05	150	9.6052	4.3824
514	-	0.25	0.05	150	9.7564	3.3996
515	-	0.25	0.05	150	0.79835	0.33801
516	-	0.25	0.05	150	2.1402	7.1794
517	-	0.25	0.05	150	6.1278	8.3889
518	-	0.25	0.05	150	6.5247	6.7258
519	-	0.25	0.05	150	4.3891	7.8219
520	-	0.25	0.05	150	5.5986	4.1556
521	-	0.25	0.05	150	4.5214	5.573
522	-	0.25	0.05	150	5.0884	4.7981

523	-	0.25	0.05	150	6.4113	5.6297
524	-	0.25	0.05	150	6.7704	4.8926
525	-	0.25	0.05	150	8.8492	2.398

A.3 Particles' size distribution

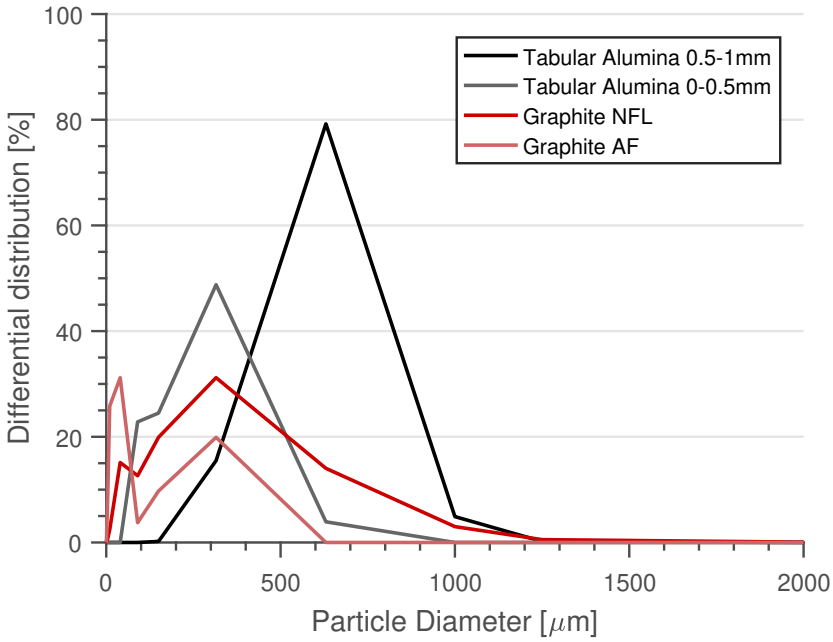

Figure A.2: Particle size distribution of the raw material used in Section 3.1.4 (Page 29).

A.4 µCT Parameters

Device	CT-ALPHA
Manufacturer	ProCon X-ray GmqH Garbsen
Year	2008
X-Ray tube	160kV Fa. Feinfocus Garbsen 2008
Mode	High Power
Tension	150 kV
Current	40 μA
Target power	5.7 W
Detector	Dexela
Type	1512
Manufacturer	Perkin Elmer
Year	2015
Active pixels	1944×1526
Image averaging	4
Skip	1
Exposure time	0.6 s
Reconstruction:	1 averaged image per 0.9 degrees

Table A.2: Parameters used for the CT analysis

A.5 Erosion - Dilation morphological procedure

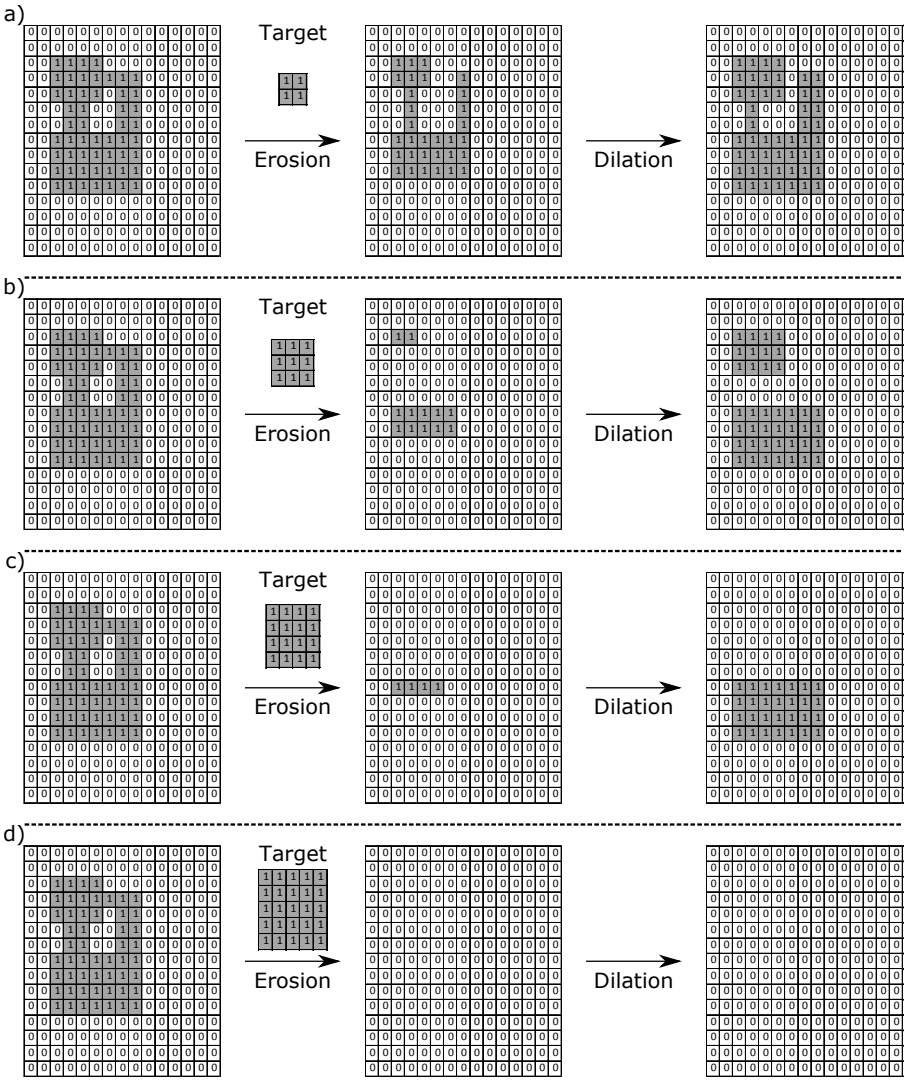

Figure A.3: Example of the morphological procedure (erosion and dilation) used to investigate the wall thickness distribution of ceramic foam filters. (The example is in 2D, while the real filters' evaluation was in 3D).

List of Figures

List of Tables